

# Quantum transport in semiconductor nanowires

*Voor mijn ouders,  
Chris, Bas  
en Annemieke.*

# **Quantum transport in semiconductor nanowires**

## **Proefschrift**

ter verkrijging van de graad van doctor  
aan de Technische Universiteit Delft,  
op gezag van de Rector Magnificus prof. dr. ir. J.T. Fokkema,  
voorzitter van het College voor Promoties,  
in het openbaar te verdedigen op dinsdag 13 juni 2006 om 15.00 uur

door

**Jorden Adriaan VAN DAM**

natuurkundig ingenieur  
geboren te Emmen.

Dit proefschrift is goedgekeurd door de promotor:

Prof. dr. ir. L. P. Kouwenhoven

Samenstelling van de promotiecommissie:

Rector Magnificus	voorzitter
Prof. dr. ir. L. P. Kouwenhoven	Technische Universiteit Delft, promotor
Prof. dr. D. Loss	Universiteit Basel, Zwitserland
Prof. dr. L. Samuelson	Universiteit Lund, Zweden
Prof. dr. Yu. V. Nazarov	Technische Universiteit Delft
Prof. dr. ir. T. M. Klapwijk	Technische Universiteit Delft
Prof. dr. H. W. M. Salemink	Technische Universiteit Delft
Dr. E. P. A. M. Bakkers	Philips Research Laboratories



*Published by:* Jorden van Dam  
*Cover designed by:* Ernst Damen / Tremani  
*Printed by:* Febodruk – [www.febodruk.nl](http://www.febodruk.nl)

Keywords: semiconductor nanowires, quantum dots, superconductivity

Casimir PhD Series, Delft-Leiden, 2006-06

ISBN: 90-8593-013-8

Copyright © 2006 by Jorden van Dam

# Preface

When I visited Delft in the beginning of 2002 on my search for a PhD position, I was happy to encounter several excellent groups and an abundance of interesting research projects. Subjects ranged from complex biological systems to single electrons in semiconductors. One project was of particular interest to me: ‘semiconductor nanowires’. That chemists could grow such amazingly versatile semiconductor nano-structures was quite a miracle for a physicist like me. Furthermore, the challenge to start a new project was very appealing. Therefore, I decided to join the Quantum Transport group (QT) of Hans Mooij and Leo Kouwenhoven and started the adventurous nanowire-journey in May 2002.

This thesis describes the experimental results of four years of research on semiconductor nanowires. Crucial for this work has been the synthesis of nanowires which was done at Philips Research Laboratories in Eindhoven. The nanowire devices were fabricated at the ‘Delft Institute of Microelectronics and Submicrontechnology’ (DIMES) and measurements were performed in our laboratory in Delft. This shows that this work is the result of intense collaboration. I am very grateful to everyone at Philips Research Laboratories, DIMES and the Delft University of Technology who has contributed to this work. There are several people I would like to thank individually.

First of all, I thank Leo Kouwenhoven for giving me the opportunity to do my PhD in QT. Your ability to choose new interesting research directions, to find enough money to keep your students (‘big spenders’) happy, and to create a good atmosphere for science is admiring. I am very thankful to Silvano De Franceschi, my supervisor. Your impressive knowledge of physics, enormous drive, and broad interest have been very inspiring. It was very nice working with you! I also thank Leonid Gurevich, especially for teaching me numerous ‘fabrication secrets’. Your enthusiasm made the cleanroom a nicer place, even when a new contact recipe once more resulted in  $G\Omega$  resistances.

I am very grateful to Erik Bakkers from Philips Research. It was a great pleasure working with you and thanks to you the collaboration between Philips and Delft is very fruitful. Without your high-quality nanowires this work would

not have been possible. Many thanks also to Aarnoud Roest. You have shot some really nice InAs nanowires with your ‘laser-gun’. Other people from Philips I thank are Lou-Fé Feiner, Magnus Borgström, Olaf Wunnicke, and Eddy Evens.

I also thank Yong-Joo Doh who was involved in our first paper on superconductivity in nanowires. Thanks to you we’ve managed to get good results and a very nice paper. Of course I am very grateful to numerous other (former) members of the ‘Delft nanowire team’. Floris joined the team about three years ago and since then worked hard on the Harvard-link. Gást, good luck with the silicon wires! Silvia, thanks for all your help with the Niobium. I thank Dirk for organizing the (already legendary) QT sailing trip and Anne for organizing the next one. Juriaan and Marc recently joined the team and will continue the research on transport in semiconductor nanowires. I am confident that you two will get very nice results. One year ago, the nanowire team started with an optics section and since then many new people joined the group. Val, Ethan, Maarten (2x), Freek, Elisabeth, and Umberto, good luck with quantum opto-electronics. I thank my students: Tessa Nolst Trenité, Sandra Foletti, Arend Zwaneveld, Marc Kea, and Fleur Rijkers for the nice time and their hard work. I’ve learned a lot from all of you. Good luck in science, consulting, and oil.

I am very thankful to Yuli Nazarov for the nice collaboration during the last few months of my PhD. I admire your deep insight in condensed matter physics and have learned a lot from our discussions. The numerous anecdotes you have used in your explanations, like ‘the story of the marble stone’, have made a deep impression. I also thank Pablo Jarillo-Herrero for the nice time we have spent studying supercurrents through carbon nanotubes. Your enthusiasm, drive, and unlimited interest in ‘facts and figures’ (like: ‘What is the average income of the top-50 CEOs?’) are impressive. Thanks for everything and good luck at Columbia University.

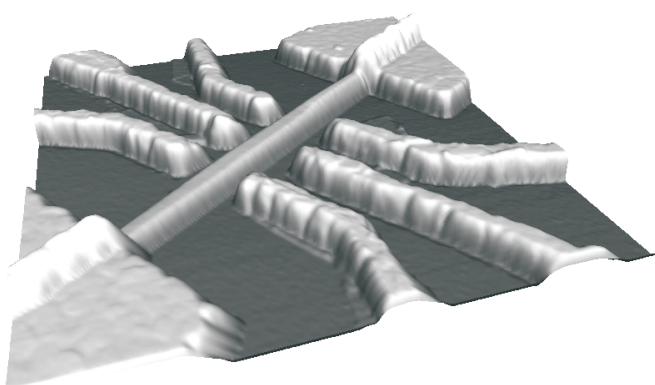
I thank Hans Mooij and Leo Kouwenhoven for making the Quantum Transport group such a great place for research. This group combines a stimulating research environment with very nice people. I would like to thank all (former) group members for their positive contributions to this group. Special thanks to the people who gave valuable technical support: Bram van der Enden, Raymond Schouten, Mascha van Oossanen, Leo Dam, Willem den Braver, Wim Schot, Leo Lander, and Remco Roeleveld. Thanks to Bram, equipment was fixed quickly (even on Friday evening) and the coffee breaks were always enjoyable. Mascha, special thanks for the bonding-lessons. I thank Wim and Willem for producing the  $\sim 10.000$  liters of Helium used for the experiments. Special thanks to Yuki French-Nakagawa and Ria van Heeren-van der Kramer for taking care of flight tickets, bills, and so many other things. I would like to thank all (former) in-

habitants of room A: Hubert Heersche, Jelle Plantenberg, Marta Mas Torrent, Laurens Willems van Beveren, Piotr Beliczynski, and Eduard Driessen. Thanks to you room A was a nice place to work, to play Quake, and to discuss physics (and other important things in life). Hubert, thanks for everything, especially for being vice-president of ‘Comité slechte koffie nee!’. I’m sure we’ve improved QT’s scientific output by getting a Kavli espresso-machine. Jelle, special thanks for the unforgettable ‘escalation-events’. Good luck in the battle against Microsoft and other software manufacturers without an ‘open source’ policy... I also acknowledge Ronald Hanson (senior vice-president of ‘Comité slechte koffie nee!’), Hannes Majer (thanks for the hospitality at Yale), Floor Paauw, Jeroen Elzerman, Alexander ter Haar, Ivo Vink, Frank Koppens (special thanks for valuable logistic support), Pieter de Groot (tunneling now has a completely different meaning), Sami Sapmaz (good luck next week), and Tristan Meunier (trying to understand the Dutch). Also many thanks to Ruth de Boer and Frank van der Heyden from the other side of the physics building. I thank Marc Zuiddam, Anja van Langen-Suurling, and Arnold van Run from DIMES for their valuable help.

I thank people from the PvdA for providing such a nice and interesting place outside the lab. Special thanks to Femke Stolker for the good times and for being my paranymp, to Carla Jonquière for the nice time we’ve had organizing several events, and to Ernst Damen for designing the cover and invitation.

During the last four years, performing measurements and writing a thesis did not always leave enough time for the more important things in life. I am very grateful to my friends, family, and Annemieke for their continuous interest, love, and support.

Jorden van Dam  
Delft, June 2006





# Contents

<b>1</b>	<b>Introduction</b>	<b>1</b>
1.1	Nanotechnology . . . . .	1
1.2	Semiconductor nanowires . . . . .	1
1.3	Outline . . . . .	3
<b>2</b>	<b>Theoretical concepts</b>	<b>5</b>
2.1	Quantum Dots . . . . .	5
2.2	Superconductivity . . . . .	9
<b>3</b>	<b>Device fabrication and measurement techniques</b>	<b>17</b>
3.1	Introduction . . . . .	17
3.2	Semiconductor nanowire growth . . . . .	17
3.3	Device fabrication . . . . .	20
3.4	Measurement techniques . . . . .	22
<b>4</b>	<b>Epitaxial growth of InP nanowires on germanium</b>	<b>25</b>
4.1	Introduction . . . . .	26
4.2	Nanowire growth and characterization . . . . .	26
4.3	Electrical measurements . . . . .	31
<b>5</b>	<b>Single-electron tunneling in InP nanowires</b>	<b>35</b>
5.1	Introduction . . . . .	36
5.2	Device fabrication . . . . .	36
5.3	InP nanowire Quantum Dots . . . . .	38
5.4	Excited state spectroscopy . . . . .	40
<b>6</b>	<b>Tunable supercurrent through semiconductor nanowires</b>	<b>43</b>
6.1	Introduction . . . . .	44
6.2	Device fabrication . . . . .	44
6.3	Gate control of supercurrents through InAs nanowires . . . . .	46
6.4	Mesoscopic properties of InAs nanowire junctions . . . . .	49

---

6.5	Appendix . . . . .	53
<b>7</b>	<b>Quantum supercurrent transistors in carbon nanotubes</b>	<b>57</b>
7.1	Introduction . . . . .	58
7.2	Quantum supercurrent transistor action . . . . .	58
7.3	Correlation between critical current and normal state conductance	62
7.4	Appendix . . . . .	67
<b>8</b>	<b>Supercurrent reversal in quantum dots</b>	<b>71</b>
8.1	Introduction . . . . .	72
8.2	Gate controlled SQUIDs . . . . .	72
8.3	Tunable quantum dots . . . . .	74
8.4	Supercurrent reversal in quantum dots . . . . .	75
8.5	Supercurrents through multi-level quantum dots . . . . .	78
8.6	Appendix . . . . .	79
	<b>Summary</b>	<b>91</b>
	<b>Samenvatting</b>	<b>95</b>
	<b>Curriculum Vitae</b>	<b>99</b>
	<b>List of publications</b>	<b>101</b>

# Chapter 1

## Introduction

### 1.1 Nanotechnology

In nanotechnology, matter is manipulated on the scale of single atoms and molecules. New tools that operate on the nanometer length scale can put atoms together in the desired arrangement or composition. In principle, this ability allows one to synthesize almost any kind of complex molecule or material. In all technology areas based on materials (e.g. physics, electronics, material science, medicine, bio-chemistry) these new techniques will have a big impact. A subfield known as Nano-electronics focuses on the development of electronic devices with nanometer length scales. The objective is not only to miniaturize existing silicon semiconductor technology but also to invent alternative concepts for storage and computation. Whereas in silicon technology bits are controlled by electrical currents and voltages, the small size of nanometer devices allows logic to be defined by individual electrons. On this scale the behavior of single electrons must be described by quantum mechanics. Often unexpected properties arise that are completely different from the behavior of large-scale devices.

### 1.2 Semiconductor nanowires

Much of the recent interest for chemically grown semiconductor nanowires arises from their unique versatility. This versatility results in a wide range of potential applications. In the last few years many proofs of concept have been shown such as field effect transistors, elementary logic circuits, resonant tunneling diodes, light emitting diodes, lasers, and biochemical sensors [1, 2, 3]. These achievements, together with the recent advance in the integration of III-V nanowires with standard silicon technology [4, 5], yield great promise for the development of next-generation (opto-)electronics. Simultaneously, the high degree of free-

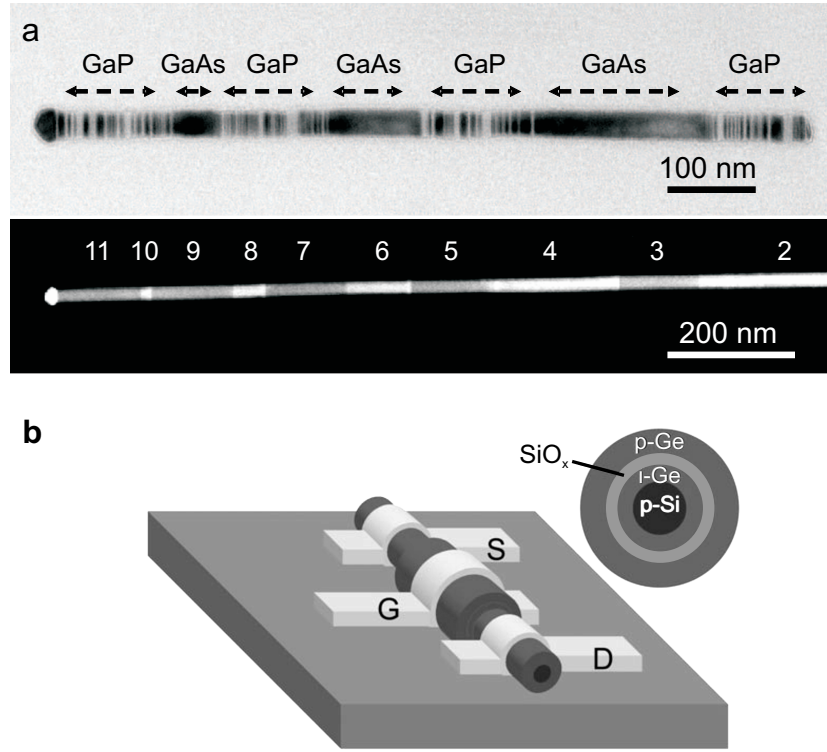


**Figure 1.1:** Two examples illustrating the high degree of freedom in semiconductor nanowire growth. **a**, top: Bright-field transmission electron microscopy (TEM) image of a heterostructured GaP-GaAs nanowire. bottom: HAADF TEM image of a different GaP-GaAs wire visualizing the heterostructures. The contrast difference is due to the different atomic masses [6]. **b**, Epitaxial core-shell silicon/germanium nanowires from the Lieber group operated as a nanowire field effect transistor [7].

dom in nanowire growth and device engineering create new opportunities for the fabrication of controlled one-dimensional systems for fundamental science.

The high degree of freedom in nanowire growth is demonstrated in Fig. 1.1a which shows a nanowire consisting of alternating sections of gallium phosphide (GaP) and gallium arsenide (GaAs) [6]. These heterostructures can be grown by changing the semiconductor material during nanowire growth. Due to the small diameter of the nanowires ( $\sim 1\text{-}100$  nm), the interface between different materials can be almost atomically sharp without dislocations. Figure 1.1b shows the feasibility of growing epitaxial core-shell heterostructures. In this work, by the Lieber group, this technique has been used in order to demonstrate the operation of a silicon/germanium field-effect transistor [7].

In this thesis we study the fascinating world of quantum mechanics using the unprecedented versatility of semiconductor nanowires. For instance, we show that semiconductor nanowires can act as gate-controlled superconducting switches and that the supercurrent through a quantum dot can reverse sign by adding one electron.

## 1.3 Outline

We now give a short description of the chapters of this thesis.

First we discuss basic theory of quantum dots and superconductivity as these are the two main subjects of this thesis. In chapter 3 we describe the growth of semiconductor nanowires, the fabrication of nanowire devices and the measurement techniques.

Chapter 4: The integration of III-V semiconductors with silicon technology is a major challenge in nanotechnology. The superior (opto-)electronic properties of III-V materials combined with the industry standard of silicon technology potentially yield many new (opto-)electronic devices. In this chapter we show that InP nanowires can be epitaxially integrated with germanium substrates using a vapor-liquid-solid growth process. The epitaxial relation between the nanowires and the substrate is investigated by high-resolution X-ray diffraction and high-resolution transmission electron microscopy. In the last part of the chapter we show, by using conductive atomic force microscopy, that a low-resistance electrical contact can be realized between the nanowires and the germanium substrate.

Chapter 5: In this chapter we discuss the fabrication of InP nanowire field-effect transistors and their electrical properties. We first present a contacting scheme that results in contact resistances as low as  $\sim 10\text{k}\Omega$  with minor temperature-dependence. Subsequently, we discuss coulomb-blockade behavior in the InP nanowire devices at low temperatures. Finally, we demonstrate energy quantization due to the confinement of electrons in small sections of the InP nanowires.

Chapter 6: Here we present tunable superconducting devices based on InAs nanowires. We start with describing the technology used to obtain high transparency superconducting contacts, the key ingredient for this work. Then we characterize the Josephson junctions and show that the supercurrent flowing through the nanowires can be controlled by a voltage applied to a nearby gate. At the end of this chapter we discuss the mesoscopic character of the nanowire superconducting junctions.

Chapter 7: In this chapter we investigate supercurrents flowing through the discrete energy levels of a carbon nanotube quantum dot. We show that if a level is on resonance with the Fermi energy of the superconducting contacts a supercurrent can flow through the carbon nanotube. We also find that the product of critical current and normal state resistance is not constant, in contrast to previously explored regimes, but becomes an oscillating function of gate voltage.

Chapter 8: In the final chapter we investigate the flow of a supercurrent through a quantum dot with strong Coulomb interactions. We use local gating to define quantum dots with a tunable coupling to superconducting electrodes. Depending on the properties of the quantum dot the supercurrent can be positive or negative. We determine the sign of the supercurrent by integrating the nanowire junction in a superconducting quantum interference device. Comparison of experimental data with numerical results shows that excited states of the quantum dot are involved in Cooper pair transport. As a result, the supercurrent sign not only depends on the number of electrons in the quantum dot but also on the character of the orbital wavefunctions.

## References

- [1] C. M. Lieber, MRS Bull. **28**, 486 (2003).
- [2] P. Yang, MRS Bull. **30**, 85 (2005).
- [3] L. Samuelson *et al.*, Physica E **25**, 313-318 (2004).
- [4] E. P. A. M. Bakkers *et al.*, Nature Materials **3**, 769 (2004).
- [5] T. Mårtensson *et al.*, Nano Lett. **4**, 1987 (2004).
- [6] M. A. Verheijen *et al.*, J. Am. Chem. Soc., **128**, 1353 (2006).
- [7] L. J. Lauhon *et al.*, Nature **420**, 57 (2002).

# Chapter 2

## Theoretical concepts

### 2.1 Quantum Dots

Quantum dots are small conducting islands with a discrete set of electronic energy levels. This discrete energy spectrum results from the confinement of electrons in a small ‘box’, analogous to the well-know ‘particle in a box’ from quantum mechanics courses. When the size of the island gets smaller, the confinement of electrons increases resulting in a larger energy level separation. This separation has to be larger than the thermal energy which typically means that measurements take place below a few Kelvin and the size of the quantum dot (QD) is below a micron. Many different material systems have been used to study QDs, like metallic nanoparticles, carbon nanotubes, single molecules, semiconductor heterostructures, and semiconductor nanowires. The quantum mechanical properties of QDs are usually studied using optical spectroscopy or electronic transport techniques. In experiments described in this thesis we have used the latter to study quantum dots defined in short segments of semiconductor nanowires. Here we present a general introduction to electronic transport through quantum dots based on ref. [1].

In order to measure electronic transport through a quantum dot, the quantum dot must be attached to source and drain reservoirs, with which particles can be exchanged (see Fig. 2.1). The QD is also capacitively coupled to one or more ‘gate’ electrodes, that can be used to tune the electrostatic potential of the dot with respect to the reservoirs.

A simple, yet very useful model to understand electronic transport through QDs is the constant interaction (CI) model [2]. In this model two important assumptions are made. First, the Coulomb interactions between electrons in the dot are captured by a single constant capacitance,  $C$ . This is the total capacitance to the outside world, i.e.  $C = C_S + C_D + C_g$ , where  $C_S$  is the capacitance to the

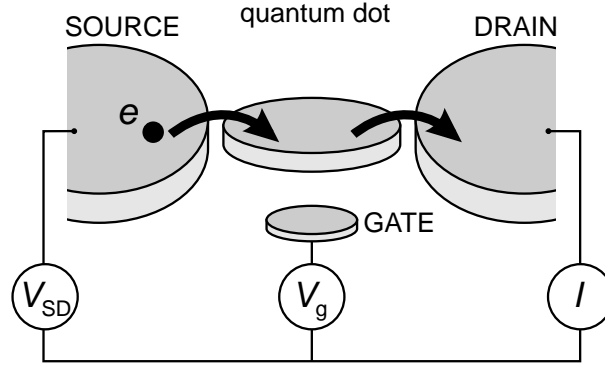


**Figure 2.1:** Schematic picture of a quantum dot. The quantum dot (represented by a disk) is connected to source and drain contacts via tunnel barriers, allowing charge carriers to tunnel to and from the quantum dot. Here, current through the device,  $I$ , is measured in response to a bias voltage,  $V_{SD}$  and a gate voltage,  $V_g$ .

source,  $C_D$  that to the drain, and  $C_g$  to the gate. Second, the discrete energy spectrum is independent of the number of electrons on the dot. Under these assumptions the total energy of an  $N$ -electron dot with the source-drain voltage,  $V_{SD}$ , applied to the source (and the drain grounded), is given by

$$U(N) = \frac{[-|e|(N - N_0) + C_S V_{SD} + C_g V_g]^2}{2C} + \sum_{n=1}^N E_n \quad , \quad (2.1)$$

where  $-|e|$  is the electron charge and  $N_0$  the number of electrons on the dot at zero gate voltage. The terms  $C_S V_{SD}$  and  $C_g V_g$  can change continuously and represent the charge on the dot that is induced by the bias voltage (through the capacitance  $C_S$ ) and the gate voltage  $V_g$  (through the capacitance  $C_g$ ), respectively. The last term of Eq. 2.1 is a sum over the occupied single-particle energy levels  $E_n$ , which are separated by an energy  $\Delta E_n = E_n - E_{n-1}$ . These energy levels depend on the characteristics of the confinement potential.

To describe transport experiments, it is often more convenient to use the electrochemical potential,  $\mu$ . This is defined as the minimum energy required to add an electron to the quantum dot

$$\begin{aligned} \mu(N) &\equiv U(N) - U(N-1) = \\ &= (N - N_0 - \frac{1}{2})E_C - \frac{E_C}{|e|}(C_S V_{SD} + C_g V_g) + E_N \quad , \end{aligned} \quad (2.2)$$

where  $E_C = e^2/C$  is the charging energy. A diagram with electrochemical potentials for different electron numbers,  $N$ , is shown in Fig. 2.2a. The discrete levels



are spaced by the so-called addition energy,  $E_{add}(N)$

$$E_{add}(N) = \mu(N+1) - \mu(N) = E_C + \Delta E \quad . \quad (2.3)$$

The addition energy consists of a purely electrostatic part, the charging energy  $E_C$ , and the energy spacing between two discrete quantum levels,  $\Delta E$ . Note that  $\Delta E$  can be zero, when two consecutive electrons are added to the same spin-degenerate level or if there are additional degeneracies present.

Transport can occur when an electrochemical potential level (or state) lies within the ‘bias window’ between the electrochemical potential of the source ( $\mu_S$ ) and the drain ( $\mu_D$ ), i.e.  $\mu_S \geq \mu \geq \mu_D$  with  $-|e|V_{SD} = \mu_S - \mu_D$ . Only then an electron can tunnel from the source onto the dot, and tunnel off to the drain without losing or gaining energy. The important point to realize is that since the dot is very small, it has a very small capacitance and therefore a large charging energy – for typical dots  $E_C \approx$  a few meV. If the electrochemical potential levels are as shown in Fig. 2.2a, this energy is not available (at low temperatures and small bias voltage). So, the number of electrons on the dot remains fixed and no current flows through the dot. This effect is known as Coulomb blockade. The charging energy becomes important when it exceeds the thermal energy,  $k_B T$ , and when the barriers are sufficiently opaque such that the electrons are located either in the reservoirs or in the dot. The latter condition implies that quantum fluctuations in the number of electrons on the dot must be sufficiently small. A lower bound for the tunnel resistances  $R_t$  of the barriers can be found from the Heisenberg uncertainty principle. The typical time  $\Delta t$  to charge or discharge the dot is given by the  $RC$ -time. This yields  $\Delta E \Delta t = (e^2/C) R_t C > h$ . Hence,  $R_t$  should be much larger than the quantum resistance  $h/e^2$  to sufficiently reduce the uncertainty in the energy.

It turns out that there are several ways to lift Coulomb blockade. First, we can change the voltage applied to the gate electrode. This changes the electrostatic potential of the dot with respect to that of the reservoirs, shifting the whole ‘ladder’ of electrochemical potential levels up or down. When a level falls within the bias window, a current can flow through the device. In Fig. 2.2b  $\mu(N)$  is aligned, so the electron number alternates between  $N-1$  and  $N$ . This means that the  $N^{th}$  electron can tunnel onto the dot from the source, but only after it tunnels off to the drain another electron can tunnel onto the dot from the source. This cycle is known as single-electron tunneling.

By sweeping the gate voltage and measuring the current, we obtain a trace as shown in Fig. 2.3a. At the positions of the peaks, an electrochemical potential level is aligned with the source and drain and a single-electron tunneling current

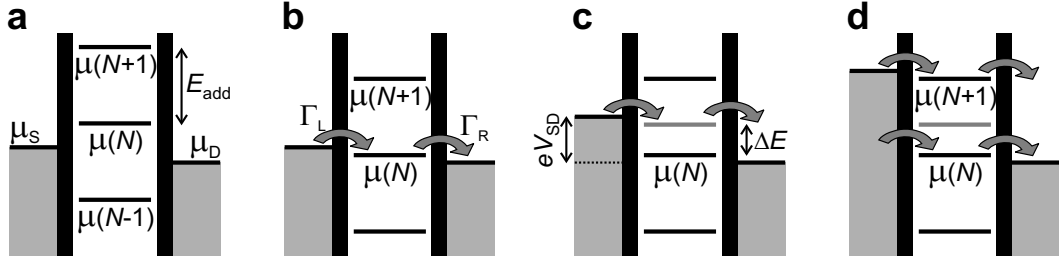


**Figure 2.2:** Schematic diagrams of the electrochemical potential of the quantum dot for different electron numbers. **a**, No level falls within the bias window between  $\mu_S$  and  $\mu_D$ , so the electron number is fixed at  $N - 1$  due to Coulomb blockade. **b**, The  $\mu(N)$  level is aligned, so the number of electrons can alternate between  $N$  and  $N - 1$ , resulting in a single-electron tunneling current. The magnitude of the current depends on the tunnel rate between the dot and the reservoir on the left,  $\Gamma_L$ , and on the right,  $\Gamma_R$ . **c**, Both the ground-state transition between  $N - 1$  and  $N$  electrons (black line), as well as the transition to an  $N$ -electron excited state (gray line) fall within the bias window and can thus be used for transport (though not at the same time, due to Coulomb blockade). This results in a current that is different from the situation in (b). **d**, The number of electrons can alternate between  $N - 1$ ,  $N$ , and  $N + 1$ .

flows. In the valleys between the peaks, the number of electrons on the dot is fixed due to Coulomb blockade. By tuning the gate voltage from one valley to the next one, the number of electrons on the dot can be precisely controlled. The distance between the peaks corresponds to  $E_C + \Delta E$ , and can therefore give

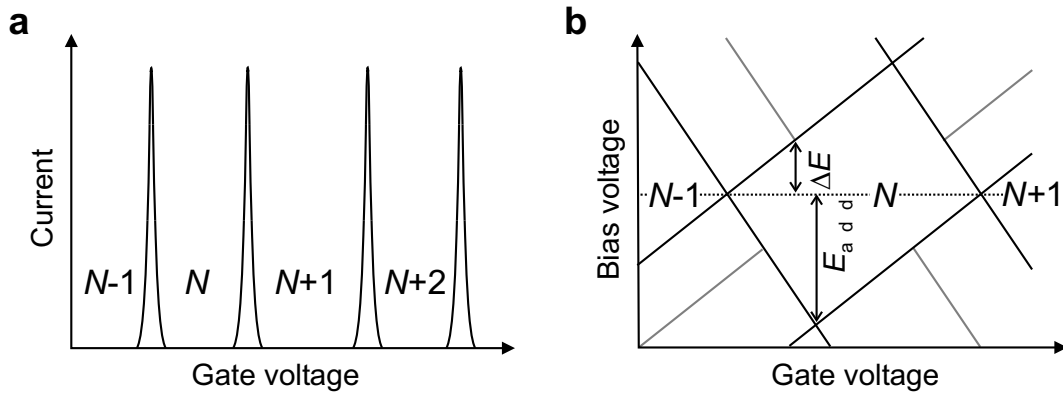


**Figure 2.3:** Electron transport through a quantum dot. **a**, Coulomb peaks in current versus gate voltage in the linear-response regime. **b**, Coulomb diamonds in differential conductance,  $dI/dV_{SD}$ , versus  $V_{SD}$  and  $V_g$ , up to large bias. The edges of the diamond-shaped regions (black) correspond to the onset of current. Diagonal lines emanating from the diamonds (gray) indicate the onset of transport through excited states.

information about the energy spectrum of the dot.

A second way to lift Coulomb blockade is by changing the source-drain voltage,  $V_{SD}$  (see Fig. 2.2c). (Typically, the drain potential is kept fixed, and only the source potential is changed.) This increases the bias window and also ‘drags’ the electrochemical potential of the dot along, due to the capacitive coupling to the source. Again, a current can flow only when an electrochemical potential level falls within the bias window. By increasing  $V_{SD}$  until both the ground state and an excited state transition fall in the bias window, an electron can tunnel not only through the ground state, but also through an excited state of the  $N$ -electron dot. This is visible as a change in the total current. In this way, excited-state spectroscopy can be performed.

Usually, the current or differential conductance is measured while sweeping the bias voltage, for a series of different values of the gate voltage. Such a measurement is shown schematically in Fig. 2.3b. Inside the diamond-shaped region, the number of electrons is fixed due to Coulomb blockade, and no current flows. Outside the diamonds, Coulomb blockade is lifted and single-electron tunneling can take place (or for larger bias voltages even double-electron tunneling is possible, see Fig. 2.2d). Excited states are revealed as changes in the current, i.e. as peaks or dips in the differential conductance. From such a ‘Coulomb diamond’ the energy of excited-states as well as the charging energy can be determined.

The simple model described above explains how quantization of charge and energy result in effects like Coulomb blockade and Coulomb oscillations. Nevertheless, it is over-simplified in many respects. For instance, the model considers only first-order tunneling processes, in which an electron tunnels first from one reservoir onto the dot, and then from the dot to the other reservoir. But when the tunnel rate between the dot and the leads,  $\Gamma$ , is increased, higher-order tunneling via virtual intermediate states becomes important [3]. Such processes, known as ‘co-tunneling’, can result in a finite current in regimes where first-order tunneling is prohibited due to Coulomb blockade. In chapter 8 we show that Cooper pairs of electrons can be transported through a quantum dot by 4<sup>th</sup>-order co-tunneling.

## 2.2 Superconductivity

The *proximity effect* is a phenomenon which can be described as the leakage of Cooper pairs of electrons from a superconductor,  $S$ , into a normal-type conductor,  $N$  [4]. The microscopic process that enables charge transport through a normal metal-superconductor interface at energies within the superconducting gap,  $2\Delta$ , is Andreev reflection [5, 6]. Here we present a general introduction to the proximity

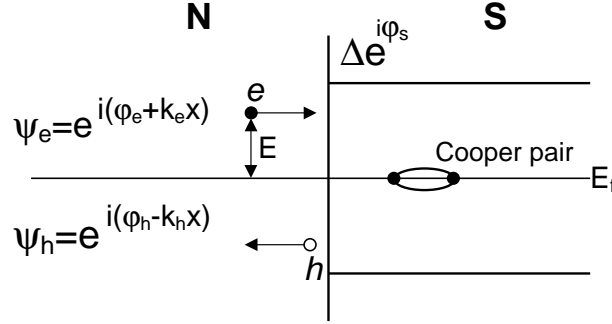


**Figure 2.4:** Schematic representation of Andreev reflection. An electron in the normal electrode (N, left) with energy  $E$  smaller than the superconducting gap  $\Delta$  (filled circle) pairs with another electron with opposite energy and wave vector to form a Cooper pair in the Superconductor (S, right). The result is a hole (open circle) in N with opposite energy and wave vector reflected away from the interface. Note that Andreev reflection is a phase coherent process, i.e.  $\varphi_h$  and  $\varphi_e$  are correlated (see §2.2.1).

effect based on ref. [7].

We consider an electron in a normal conducting metal with an energy  $E < \Delta$  above the Fermi energy approaching a clean normal metal-superconductor interface. Due to the presence of a gap in the excitation spectrum of the superconductor no electron states are available at energies  $E < \Delta$  in the superconductor. As a result the wave function of the electron is exponentially damped over a length scale given by the superconducting coherence length  $\xi_s = \hbar v_F / (\pi \Delta)$  [8]. This implies that the electrons at those energies are reflected. As shown by Andreev in 1964 [5] transport through clean  $N - S$  interfaces [9] at energies  $E < \Delta$  can occur due to a reflection process now referred to as *Andreev reflection*.

The process of Andreev reflection is schematically shown in Fig. 2.4. An electron  $e$  with energy  $E$  and wave vector  $k_e$  impinges on the  $N - S$  interface. For simplicity we assume  $\Psi = \Delta e^{i\varphi_s}$  in the superconductor and  $\Psi = \Delta = 0$  elsewhere. At the interface the electron pairs with another electron with opposite momentum, spin and energy to form a Cooper pair in the superconductor. The result is a hole  $h$  with energy  $-E$  and wave vector  $k_h$ , that moves away from the  $N - S$  interface. Note that also the opposite Andreev reflection process can occur: a hole impinging on the  $N - S$  interface will be reflected as an electron.

### 2.2.1 Properties of Andreev reflection

We now discuss three important properties of *Andreev reflection* in more detail.

### Retro-reflection

The small energy difference  $2E$  between the hole and the electron results in an *almost* identical magnitude of the electron and hole wave vectors. The difference in wavevectors,  $\delta k$ , is given by

$$\delta k = \left( \frac{dE}{dk} \right)_{E=E_f}^{-1} \times 2E = \frac{2E}{\hbar v_F} . \quad (2.4)$$

As a result we can write

$$\begin{aligned} k_e &= k_f + \frac{E}{\hbar v_F} \\ k_h &= k_f - \frac{E}{\hbar v_F} . \end{aligned} \quad (2.5)$$

### Phase coherence

Andreev reflection is a phase coherent process. This means there is a well defined relation between the phase of the electron  $\varphi_e$  and the (Andreev) reflected hole  $\varphi_h$ . These relations are given by

$$\begin{aligned} \varphi_h &= \varphi_e + \varphi_s - \arccos(E/\Delta) \\ \varphi_e &= \varphi_h - \varphi_s - \arccos(E/\Delta) , \end{aligned} \quad (2.6)$$

where  $\varphi_s$  is the phase of the superconducting condensate. This relation is a consequence of the continuity conditions of the electron and hole wave functions and their derivatives.

At the fermi energy ( $E = 0$ ), the last term in eq. 2.6 equals  $\pi/2$ . This is particularly relevant when phase coherent Andreev reflections have to be considered between particles that have undergone 1 and  $2n + 1$  Andreev reflections ( $n$  an integer). In both situations an electron is converted into a hole (or a hole into an electron). However, these particles have a relative phase shift of  $\pi$  with respect to each other and as a result they interfere destructively. An example of a resulting effect is the re-entrant behavior of the resistance of a normal conducting material connected to a single superconductor [10].

If only one superconductor is present in the system,  $\varphi_s$  does not play a role and can be chosen zero by an appropriate gauge transformation. The situation changes if two superconductors are present with phases  $\varphi_{s1}$  and  $\varphi_{s2}$ . In this situation it is to be expected that interference effects occur periodic in  $(\varphi_{s1} - \varphi_{s2})$ .

### Phase conjugation

As stated before, the wave vector of an electron and Andreev reflected hole are almost identical in magnitude. This has important consequences for the dynamical phase,  $\theta$ , which the two particles acquire. Consider the 1-D problem of an electron in a normal metal a distance  $-L$  from the  $S-N$  interface. At the interface the electron has acquired a dynamical phase  $\theta_e$  by travelling from  $x = -L$  to  $x = 0$  given by

$$\theta_e = \int_{-L}^0 k_e dx = k_F L + \frac{E}{\hbar v_F} L \quad . \quad (2.7)$$

At the interface the electron is Andreev reflected and due to the retro-active property of Andreev reflection the hole returns to the position  $x = -L$  which results in a phase

$$\theta_h = \int_0^{-L} k_h dx = -k_F L + \frac{E}{\hbar v_F} L \quad . \quad (2.8)$$

At the Fermi energy  $k_e = k_h$ , so the dynamical phase acquired by the electron upon traveling to the  $S-N$  interface is exactly canceled by the phase shift of the returning hole. This implies that the presence of a superconductor enhances particle interference effects in the normal metal because the dynamical phases of the original electron and reflected hole cancel.

### 2.2.2 Andreev bound states

As discussed before, Andreev reflection is the process that enables charge transport at energies  $E < \Delta$  through an  $S-N$  interface. The same is true for supercurrent transport through an  $S-N-S$  junction. Let us therefore consider what happens if two superconductors are attached to a single piece of normal conducting material. For simplicity we assume a 1-D picture, in which the superconducting order parameter in the superconductors is given by  $\Psi(x) = \Delta e^{i\varphi_s}$  ( $\varphi_s = \varphi_{s1}$  or  $\varphi_{s2}$ ) and  $\Psi = \Delta = 0$  in the normal metal. The semiconductor picture of such a structure is shown in Fig. 2.5. Consider an electron at an energy  $E < \Delta$  above the Fermi energy moving in the positive (+) direction (from left to the right in the picture) starting at the leftmost  $S-N$  interface. After traveling a distance  $L$  it impinges on the  $S-N$  interface of superconductor 2 and will be Andreev reflected as a hole at energy  $-E$ . The hole retraces the path of the original electron, reaches superconductor 1 and will be Andreev reflected again. We now are back at the starting position. The result of this cycle is the transfer of a charge of  $2e$  from S1 to S2. Within a full quantum description this electron-hole motion

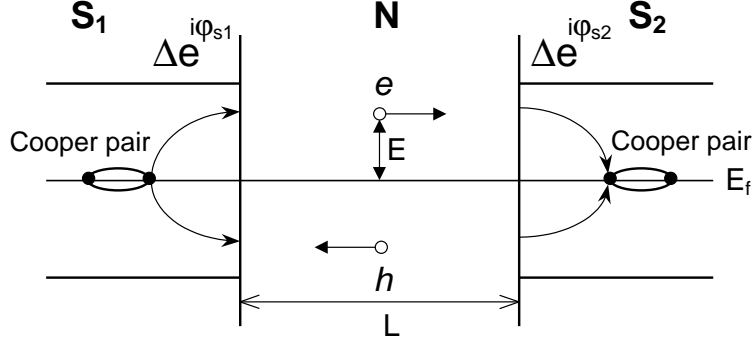


**Figure 2.5:** Schematic representation of an Andreev bound state. Multiple phase coherent Andreev reflections lead to the formation of Andreev bound states. In every cycle a charge of  $2e$  is transported from  $S_1$  to  $S_2$ . Note that also the opposite process is possible, in which the electron travels to the left, resulting in a current in the opposite direction.

forms a bound state if the total phase acquired during one cycle is a multiple of  $2\pi$  [6, 11, 12, 13, 14]. This is called an *Andreev bound state*. The condition for the formation of such a state would therefore be

$$\varphi_{s2} - \varphi_{s1} + (k_e - k_h)L - 2 \arccos(E/\Delta) = 2\pi n \quad . \quad (2.9)$$

However, the situation is a bit more complicated, for the opposite state also exists, where we start with a left moving electron. Using Eq. 2.5 and  $\varphi = \varphi_{s1} - \varphi_{s2}$  we can write for the energy of state  $n$

$$E_n^\pm = \frac{\hbar v_F}{2L} [2(\pi n + \arccos(E/\Delta)) \pm \varphi] \quad , \quad (2.10)$$

where the superscript  $+$  denotes the state with a right moving electron (left moving hole) and  $-$  the state with a left moving electron (right moving hole). If we now consider a long junction, in which the  $(k_e - k_h)L$  term dominates over the  $2 \arccos(E/\Delta)$  term in Eq. 2.9, Eq. 2.10 simplifies to

$$E_n^\pm = \frac{\hbar v_F}{2L} [2\pi(n + 1/2) \pm \varphi] \quad , \quad (2.11)$$

for energies  $E < \Delta$ . Note that every bound state  $n$  is in principle degenerate, for it consists of a  $+$  and a  $-$  state. As can be seen from Eq. 2.10 and Eq. 2.11 this degeneracy is lifted by  $\varphi \neq 2\pi n$ . The dispersion relation is shown in Fig. 2.6 and is an odd function with respect to the Fermi energy. The total supercurrent carried by these bound states at  $T = 0$  can be calculated using the relation

$$I_n^\pm = -(2e/\hbar) \sum_n dE_n^\pm/d\varphi \quad . \quad (2.12)$$

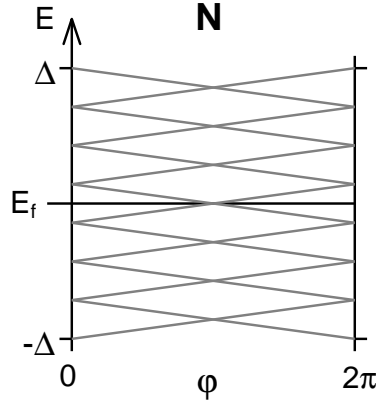


**Figure 2.6:** Schematic representation of the dispersion relation of the Andreev bound states in a long ballistic SNS junction. Note that the slope of each subsequent state is opposite, resulting in charge transport in the opposite direction for each consecutive state.

This indicates that each state carries a supercurrent  $ev_F/L$  and that each subsequent state carries supercurrent in the opposite direction [15]. The lowest state,  $E_0^+$ , carries a supercurrent in the positive direction with respect to the phase difference  $\varphi$ , i.e. from larger values of  $\varphi$  to smaller values of  $\varphi$ . This is perhaps the most intriguing property of Andreev bound states, they are localized states capable of (net) supercurrent transport.

A question that might arise from Eq. 2.12 is the following: why do we have a net supercurrent if Andreev bound states come in pairs carrying supercurrent in opposite directions? In order to understand this we have to look at the occupation probability of the Andreev bound states. When the phase difference between the superconductors is zero, the occupation of Andreev bound states carrying supercurrent in opposite directions is the same resulting in a vanishing supercurrent. However, when the phase difference is nonzero, time reversal symmetry is broken and the occupation probability of bound states carrying supercurrent in opposite directions is different. This results in a finite net supercurrent.

## References

- [1] Ronald Hanson, *Electron spins in Semiconductor Quantum Dots*, PhD thesis (2005).
- [2] Kouwenhoven, L. P., Marcus, C. M., McEuen, P. L., Tarucha, S., Westervelt, R. M. & Wingreen, N.S. Electron transport in quantum dots, in *Mesoscopic Electron Transport*, edited by Sohn, L. L., Kouwenhoven, L. P. & Schön, G.



- (Kluwer, Series E **345**, 1997), p.105-214.
- [3] Averin, D. V. & Nazarov, Yu. V. in *Single Charge Tunneling - Coulomb Blockade Phenomena in Nanostructures*, edited by Grabert, H. & Devoret, M.H. (Plenum Press and NATO Scientific Affairs Division, New York, 1992), p. 217.
- [4] P. G. de Gennes, Rev. Mod. Phys. **36**, 216 (1964).
- [5] A. F. Andreev, Zh. Eksp. Teor. Fiz. **46**, 1823 (1964) [Sov. Phys. JETP **19**, 1228 (1964)].
- [6] B. J. van Wees and H. Takayanagi, in: *Mesoscopic Electron Transport: NATO ASI series* vol. 345, 469-502 L. L. Sohn *et al* (eds.) (Kluwer Academic, Dordrecht, Boston, London, 1997) (1997).
- [7] Jochem Baselmans, *Controllable Josephson Junctions*, PhD thesis (2002).
- [8] See for instance M. Tinkham, *Introduction to Superconductivity*, McGraw-Hill, Singapore, (1996).
- [9] The limit of arbitrary transparent S-N interfaces is discussed in: G. E. Blonder, M. Tinkham and T. M. Klapwijk, Phys. Rev. B **25**, 4515 (1982).
- [10] For a review see: C. J. W. Beenakker and H. van Houten, Solid State Phys. **44**, 1-228 (1991).
- [11] I. O. Kulik, Zh. Eksp. Teor. Fiz. **57**, 1745 (1969) [Soviet Physics JETP, **30**, 944-950 (1970)].
- [12] C. Ishii, Proc. on Theor. Phys. **5**, 1525 (1972).
- [13] J. Bardeen and J. L. Johnson, Phys. Rev. B **5**, 72 (1972).
- [14] B. J. van Wees, K. -M. H. Lenssen, and C. J. P. M. Harmans, Phys. Rev. B **44**, 470 (1991).
- [15] The net supercurrent of a ballistic SNS junction in the long limit however is not given by Eq. 2.12, as the contribution of states at  $E > \Delta$  must be included. These states, which are continuous due to the lack of confinement, exist because the probability of Andreev reflection does not drop instantaneously to 0 when  $E = \Delta$  is reached [9, 6, 14].



# Chapter 3

## Device fabrication and measurement techniques

### 3.1 Introduction

In this chapter we describe in detail the complete fabrication process of semiconductor nanowire devices, including nanowire growth. At the end of the chapter we discuss the measurement techniques. For a successful experiment, nanowire growth and device fabrication are crucial, especially for devices where local gating and superconductivity are involved. The fabrication process can typically be divided into three parts: (i): nanowire growth, (ii) nanowire deposition, and (iii) electrode fabrication. The nanowire growth was performed at Philips Research in Eindhoven, The Netherlands. After growth, further device processing was carried out at the Delft Institute of Microelectronics and Submicron-technology (DIMES).

### 3.2 Semiconductor nanowire growth

Several fabrication methods are available to grow semiconductor nanowires. They can be divided into two classes: top-down and bottom-up methods. In top-down methods the strategy is to start with a large piece of semiconductor material and use techniques to obtain nanoscale wires, like nanolithography and etching. In bottom-up methods the starting point is a nano-scale object and a chemical process is used to obtain semiconductor nanowires. The nanowires studied in this thesis were grown using a bottom-up process based on the vapor-liquid-solid (VLS) growth method [1]. We have mainly studied InP and InAs nanowires grown

---

Parts of this chapter have been published in MRS symposium proceedings.

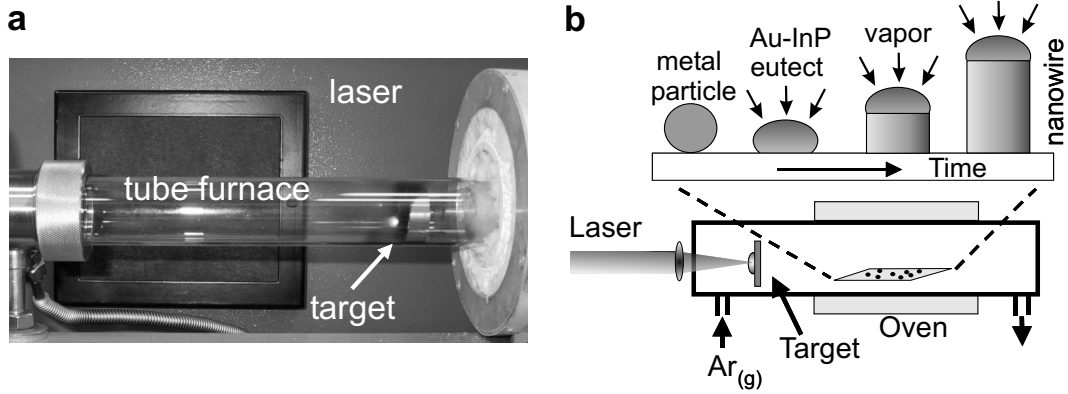


**Figure 3.1:** **a**, Photograph of the laser ablation setup. The InP target is indicated by the white arrow and light from the laser pulse is visible. **b**, Schematic of the laser ablation setup for the VLS growth of InP nanowires. The upper part of the panel shows the different stages of nanowire growth. Starting from a gold particle on the left, the second stage is a Au-InP eutect when semiconductor vapor is dissolved in the particle. When the particle is saturated with semiconductor material the single-crystal nanowire starts to grow.

by two different types of VLS growth methods. The most important difference between the two methods is the way semiconductor vapor is supplied. In the laser-ablation method, semiconductor vapor is supplied by focusing a high-intensity laser on a semiconductor material [2]. In the case of Metal-Organic Vapor-Phase Epitaxy [3] (MOVPE) or Chemical Beam Epitaxy [4] (CBE) the semiconductor material is supplied through organic molecules like trimethylindium (TMI) and phosphine ( $\text{PH}_3$ ). Despite the fact that we use two different growth methods and various semiconductor materials, all wires are grown by the VLS growth mode. We will now discuss in detail the growth of InP nanowires by laser ablation (see Fig. 3.1a). Details on wire growth for other materials and MOVPE growth are given in the following chapters when necessary.

We start with a silicon sample covered with a native oxide layer and deposit the equivalent of a 2-20 Å gold film. The substrate is mounted onto an  $\text{Al}_2\text{O}_3$  block at the downstream end of the tube oven. After evacuating the quartz tube to a pressure of  $1 \cdot 10^{-7}$  mbar the tube is flushed with argon (6N). We heat the oven to 730-850°C and monitor the substrate temperature with a thermocouple located 0.5 mm below the substrate. Upon heating, the thin Au film breaks up into small nanoscale gold particles, acting as catalysts for nanowire growth. The beam of an ArF laser ( $\lambda=193$  nm, 100 mJ/pulse, 2.5-10 Hz) is focused on either a pressed InP target (density 65%) or on a piece of single crystalline InP. The ablated In and P species are carried by the argon gas flow (210 sccm, 140 mbar) towards the

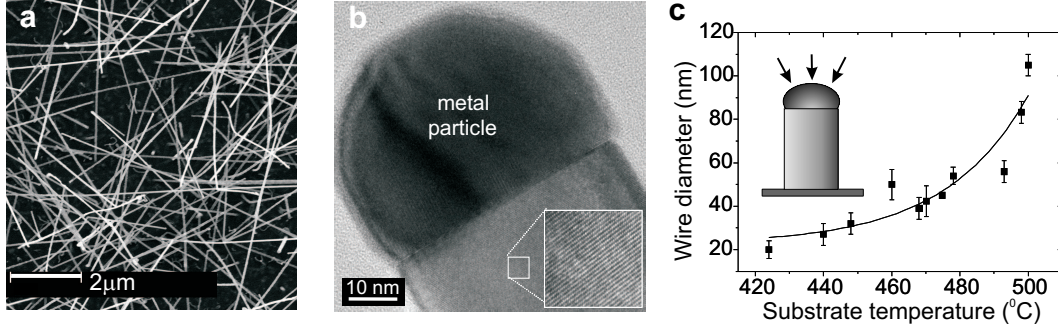


**Figure 3.2:** **a**, SEM image of InP nanostructures grown on a silicon substrate from a 2 Å Au film. **b**, HR-TEM image of an InP nanowire demonstrating the crystallinity of the nanowires. **c**, Wire diameter versus substrate temperature.

substrate, where they dissolve into the Au particles (see Fig. 3.1b). Once the Au dots are saturated by In and P, a one-dimensional, crystalline structure starts to grow. The length of the InP nanowires is controlled by the growth time, typically ~60 min. This results in nanowires with a length of several micron.

Figure 3.2a shows a typical Scanning Electron Microscopy (SEM) image of the as-grown InP nanowires. Over 95% of the deposited material consists of one-dimensional structures. When the substrate temperature is in the range 425-500°C and an undoped InP (6N) target is used, single-crystalline InP nanowires are formed. We use high-resolution TEM (TECNAI TF30ST, Fig. 3.2b) to determine the growth direction and the crystal structure. The long axis of most of the wires is perpendicular to the (111) lattice plane as has been reported by others [5], but also growth along the [211] direction is observed occasionally. Each wire is terminated by a particle containing Au and an amount of InP (typically 40%, as determined by EDX), indicating that the wires grow via the VLS mechanism. The diameter of the nanowires is initially dictated by the thickness of the Au film. However, the substrate temperature during growth affects the resulting diameter as well. In Fig. 3.2c the resulting wire diameter, obtained from TEM measurements, is plotted versus the substrate temperature in the range 425-500°C for a constant Au layer thickness of 5 Å. The wire diameter increases with temperature, which is expected considering the Au-InP-phase diagram. An additional amount of InP will dissolve in the Au particle when the temperature is raised. This results in an increase of the particle diameter leading to a thicker wire. The thinnest wires we obtained, starting with a 2 Å Au film, have diameters of 4 nm.

As mentioned at the beginning of this section, the growth of InP by laser ablation is only one of several growth processes used throughout this thesis. Other

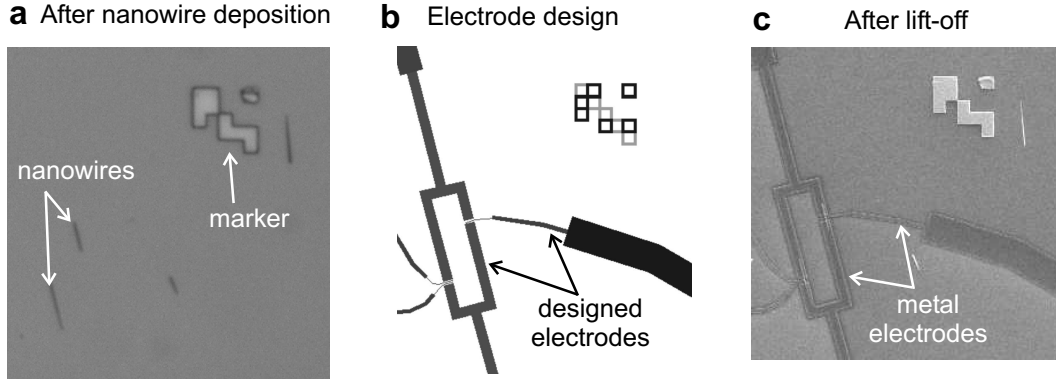


**Figure 3.3:** Device fabrication. **a**, Optical image used to determine the position of nanowires with respect to alignment markers. **b**, Computer design of the metallic contacts. **c**, Scanning electron microscope image of the device after fabrication.

semiconductor materials have been grown, and for some studies MOVPE has been used instead of laser ablation, like in chapter 8. Moreover, instead of growth on oxidized silicon substrates we also studied epitaxial growth of nanowires on crystalline substrates. In chapter 4, for instance, we study the epitaxial growth of InP on germanium substrates.

### 3.3 Device fabrication

In this section we discuss the techniques for device fabrication. After describing the nanowire deposition on suitable substrates we present the principle of electron beam lithography, which is used for defining the electrodes. Finally, we discuss the deposition of ohmic contacts and local gates.

#### 3.3.1 Nanowire deposition

After nanowire growth at Philips Research the wires are transported to Delft and subsequent processing takes place at the DIMES nanofacility. The first step is the deposition of nanowires on suitable substrates for further device fabrication. We use degenerately doped  $p^{++}$  silicon wafers covered by a 250 nm thick dry thermal oxide. This allows us to use the substrates as a global gate for field-effect devices where the thermal oxide acts as the gate dielectric.

Several different methods are available for the transfer of nanowires from the growth chip to the doped silicon substrates. Here we describe two processes, namely: (i) deposition from solution, and (ii) direct transfer. When the wires are deposited from solution, we first put the chip with as-grown nanowires (as in

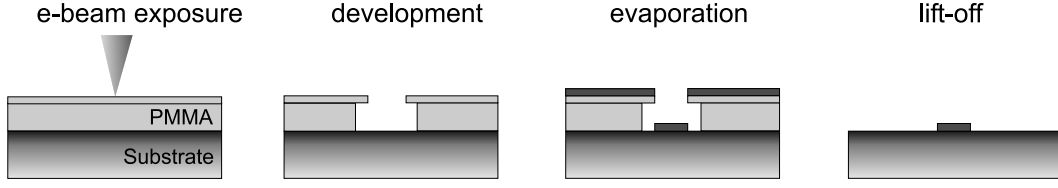


**Figure 3.4:** Schematic of the electrode fabrication process. In the first step a double-layer of e-beam resist (PMMA) is exposed using an e-beam pattern generator (EBPG). Then the exposed areas are dissolved with a suitable developer and a metal film is deposited using e-beam evaporation. In the last step the remaining resist is removed using a solvent (right panel).

Fig. 3.2a) in 2-propanol (IPA). By low-power ultrasonic agitation the nanowires are released from the growth-chip and suspended in solution. The nanowires in the IPA can now be transferred to the silicon substrate using a pipette. As a last optional step a spinner is used to dry the chip in order to prevent undesirable deposits on the chip. The second deposition method, called direct transfer, is even more straightforward than deposition from solution. We gently put the growth chip on top of the oxidized silicon substrate resulting in the direct transfer of nanowires to the silicon substrate.

After nanowire deposition the position of the nanowires on the substrate have to be determined in order to fabricate individual electrodes. This is done by using pre-deposited markers on the silicon substrate. These markers are defined by electron beam lithography, a technique we discuss in section 3.3.2. Figure 3.3a shows an optical image of InAs nanowires deposited on a substrate with markers. We have used Computer Aided Design (CAD) software in order to design individual electrodes to the nanowires. An example of a design connecting the two nanowires indicated by the white arrows is shown in Fig. 3.3b.

### 3.3.2 Electron beam lithography

We have used electron beam lithography (EBL) for defining the electrodes in a layer of resist. This process is illustrated schematically in Fig. 3.4 and consists of the following steps: (i) Spinning of resist, (ii) E-beam exposure, (iii) Metal deposition, (iv) Lift-off.

(i) For this thesis we have used a double layer of polymethyl methacrylate (PMMA). The double layer improves the lift-off process due to a better resist profile with an undercut. This results from a higher sensitivity of the bottom layer compared to the top layer. The bottom layer (8% PMMA/MMA in ethyl-L-lactate) is spun for 55 seconds at 3000 rpm and subsequently baked at 175°C

for 15 minutes. The top layer (2% 950k PMMA in chlorobenzene) is spun at 4000 rpm for 55 seconds. We use a final bake at 175°C for 60 minutes.

(ii) The CAD design is written in the resist by an e-beam pattern generator (EBPG). Due to the exposure by an electron beam bonds in the polymer are broken and the resist becomes soluble in a developer. We have used methyl-isobutyl-ketone (MIBK):IPA 1:3 as a developer with a development time of 60 seconds. Subsequently, the sample has been rinsed for 60 seconds in IPA.

(iii) Metal deposition is typically done by e-beam evaporation in a vacuum system with a background pressure of  $3 \cdot 10^{-8}$  mBar using deposition rates of 0.1-0.5 nm/s. In order to reduce contact resistances between metal contacts and semiconductor nanowires we have often performed a wet etch just before evaporation. This process consists of a 5 seconds dip in an Ammonium-buffered HF solution (BHF) followed by a rinse in H<sub>2</sub>O.

(iv) The final step in the fabrication process is lift-off. In this step the remaining resist is dissolved by immersing the sample in hot acetone (50°C) for 15 minutes. Subsequently, the sample is rinsed in cold acetone and dried with a nitrogen flow. Figure 3.3c shows a Scanning electron microscope image of a sample after lift-off.

### 3.3.3 Device packaging

The samples (with a typical size of 5×5 mm) are glued on a 32-pin chip-carrier using silver paint. The silver paint ensures a good electrical connection between the silicon substrate and the chip-carrier which is important if we use the substrate as a global gate. Electrical connections from the chip to the chip-carrier are made by ultrasonic bonding using Al/Si(1%) wires. Because the electrical contacts on the chip are separated from the substrate by a thin silicon oxide of 250 nm, the bonding has to be done carefully in order to prevent gate leakage. Therefore we use a flat bonding-tool and minimize the force during bonding (equivalent to ~18 gram).

## 3.4 Measurement techniques

Measurements have been performed at low temperatures in order to study the quantum mechanical phenomena of interest, like superconductivity and discrete energy spectra. The temperature ranges from 4.2 Kelvin down to 30 mK. For measurements between 1.5 and 4.2 Kelvin we have used a dip-stick which is immersed in a liquid helium dewar. By pumping on a 1-K pot the temperature



can be reduced to 1.5 Kelvin. For most other measurements we have used a dilution refrigerator in order to reach temperatures as low as 30 mK.

Although various different systems have been used throughout this thesis to cool down samples, the equipment for the electrical measurements has always been very similar. We have used battery-powered, in-house-built measurement equipment for all our electrical measurements in order to minimize the noise level. Voltage and current sources are computer-controlled and optically isolated from the electrical environment of the sample. Also the outputs of voltage amplifiers and IV-converters are optically isolated from the measurement computer.

In many experiments the filtering of noise is a crucial ingredient for a successful experiment. This is particularly important for measuring supercurrents because noise strongly suppresses the magnitude of the supercurrent. For these measurements we have used three stages of filtering: a  $\pi$ -filter, a copper-powder filter (CuF), and a two-stage RC filter (RCF). Together these filters cover the whole spectrum from low frequencies ( kHz) up to the microwave regime. More details about filtering are given in section 7.4.

## References

- [1] Wagner, R. S., & Ellis, W. C. Appl. Phys. Lett. **4**, 89 (1964).
- [2] Morales, A. M., & Lieber, C. M. Science **279**, 208 (1998).
- [3] Hiruma, K., *et al.* J. Appl. Phys. **77**, 447 (1995).
- [4] Björk *et al.* Nano Lett. **2**, 87 (2002).
- [5] Gudiksen, M. S., Wang, J., & Lieber, C. M. J. Phys. Chem. **105**, 4062 (2001).



# Chapter 4

## Epitaxial growth of InP nanowires on germanium

Erik P. A. M. Bakkers, Jorden A. van Dam, Silvano De Franceschi, Leo P. Kouwenhoven, Monja Kaiser, Marcel Verheijen, Harry Wondergem, & Paul van der Sluis

The growth of III-V semiconductors on silicon would allow the integration of their superior (opto-)electronic properties [1, 2, 3] with silicon technology. But fundamental issues such as lattice and thermal expansion mismatch and the formation of antiphase domains have prevented the epitaxial integration of III-V with group IV semiconductors [4, 5, 6]. Here we demonstrate the principle of epitaxial growth of III-V nanowires on a group IV substrate. We have grown InP nanowires on germanium substrates by a vapor-liquid-solid [7] method. Although the crystal lattice mismatch is large (3.7%), the as-grown wires are monocrystalline and virtually free of dislocations. X-ray diffraction unambiguously demonstrates the heteroepitaxial growth of the nanowires. In addition, we show that a low-resistance electrical contact can be obtained between the wires and the substrate.

---

This chapter has been published in Nature Materials.

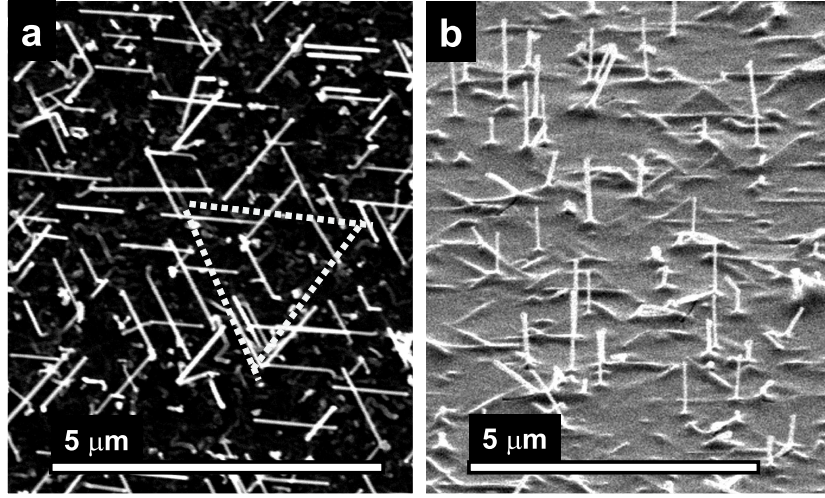


**Figure 4.1:** Scanning Electron Microscopy images of two samples with InP nanowires grown on Ge(111). **a**, Topview image showing wires aligned according to the crystal symmetry of the substrate. **b**, Sideview image after spin-coating of a PMMA layer.

## 4.1 Introduction

With the development of the VLS (vapor-liquid-solid) wire growth method [7] it has become possible to grow nanowires with built-in heterojunctions [8, 9, 10]. The formation of an almost atomically sharp heterojunction has been demonstrated in an InAs/InP nanowire [8]. For these wires it was suggested that the mechanical stress induced by the lattice mismatch (3.1%) is relieved laterally at the wire surface, and this idea is supported by a detailed analysis of the electrical characteristics [11]. Homoepitaxial growth of nanowires on bulk substrates has been proposed for several semiconductor systems such as Ge [12], Si [13], InAs and GaAs [14], and heteroepitaxial growth has been suggested for Ge wires on silicon [15] and GaN [16] and ZnO [17] on sapphire substrates. In these systems, the nanowires are geometrically oriented, which gives an indication for epitaxial growth. However, crystallographic evidence for epitaxial wire growth has not been presented so far. Moreover, heteroepitaxial growth of III-V nanowires on a group IV semiconductor has not been addressed at all.

## 4.2 Nanowire growth and characterization

Here we demonstrate the viability of integrating III-V nanowires structurally and electrically with a group IV substrate. For this study, InP nanowires were grown on Ge(111), which corresponds to the preferential growth direction for

these nanowires, and on Ge(100) substrates, which relates to the standard orientation for silicon technology. Germanium was chosen (instead of the more used silicon) because of the less troublesome procedure for removing the surface oxide. The substrates were cleaned in a buffered HF etch and were provided with the equivalent of a 2 Å gold film by thermal evaporation. Upon heating, the gold film breaks up into small particles from which the nanowires grow via the VLS method [7]. The substrate temperature during synthesis was 430-490°C, as reported previously [18].

A top-view scanning electron microscopy (SEM) image of a Ge(111) substrate with as-grown InP wires is shown in Fig. 4.1a. The wires have a uniform diameter and a length of  $\sim 1 \mu\text{m}$ . There are three clearly noticeable orientations with in-plane components parallel to the sides of an equilateral triangle, which is drawn as a guide to the eye. Some wires are oriented perpendicular to the surface, and in this top view they appear just as small bright spots. The observed preferential orientations correspond to the four  $\langle 111 \rangle$  directions typical for a (111) oriented crystal; one orientation perpendicular to the surface and three orientations forming a  $19^\circ$  angle with the surface and having in-plane components at  $120^\circ$  from each other. The fact that nanowires have well-defined orientations consistent with the substrate's crystal symmetry is a clear indication of epitaxial growth. To substantiate this claim further we have performed X-ray diffraction (XRD) and transmission electron microscopy (TEM) measurements.

The crystallographic relation between the Ge substrate and (a large number of) InP nanowires was studied by XRD pole figure measurements. Pole figures were measured for the (111) and (220) reflections as explained in the caption of Fig. 4.2a. The pole pattern (Fig. 4.2b) associated with the majority of the wires (i.e., about two-thirds of the total signal) matches the pole pattern of the substrate, providing an unambiguous signature of heteroepitaxial growth. The rest of the wires exhibit a  $180^\circ$  in-plane rotation with respect to the Ge crystal, which we ascribe to twinning defects at the Ge/InP interface or inside the wires. The fact that the mirrored orientations give a lower signal than the orientation identical to the substrate reveals that the density of twinning defects is low. Most likely a large fraction (half) of the wires was grown without twinning defects at all. Also in the case of InP wires grown on Ge(100) substrates, XRD pole figures illustrate that wire growth is epitaxial (data not shown).

The possible existence of a tilt in the crystal structure of the nanowires with respect to the substrate was studied in more detail by means of high-resolution pole measurements (Fig. 4.2c). These measurements demonstrate that the crystal lattice orientation of the wires is identical ( $\pm 0.09^\circ$ , see Fig. 4.2d) to that of the substrate. In particular, we haven't observed reflections at  $\omega = \pm 1.4^\circ$  from the

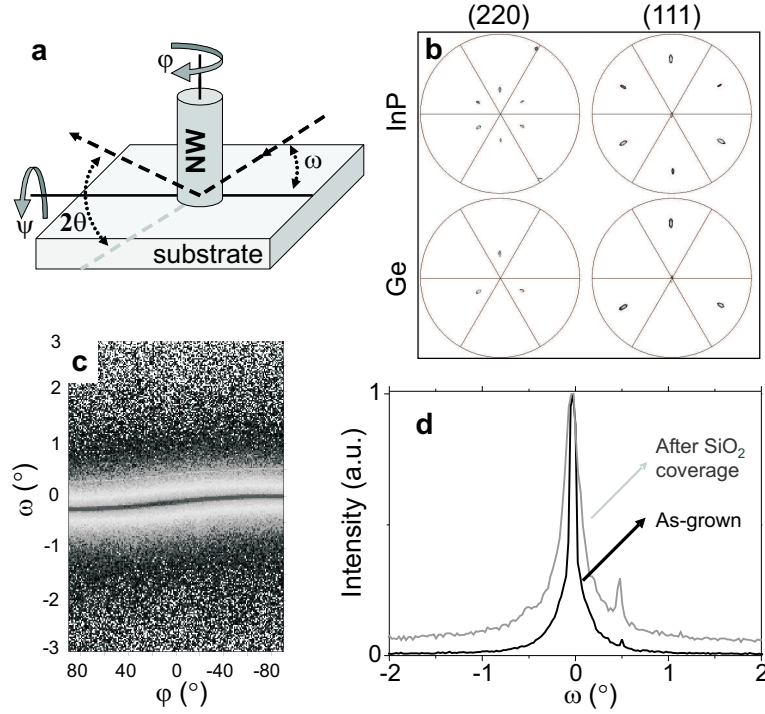


**Figure 4.2:** The crystallographic relation between the InP wires and the Ge substrate studied by X-ray diffraction. NW indicates an InP nanowire. **a**, Illustration of the experimental geometry. **b**, X-ray diffraction pole figures for the (111) and (220) reflections from the InP nanowires and the Ge(111) substrate. To record the pole figure, the detector was set at a  $2\theta$  angle corresponding to one of these reflections and the substrate was rotated continuously around  $\phi$  (see Fig. 4.2a), and stepped around  $\psi$  ( $\Delta\psi=2^\circ$ ). **c**, High-resolution pole figure (intensity increases from black to white, and gray) of the (111) InP planes parallel to the Ge surface. A scan in the  $\omega$  direction (with a resolution of  $0.005^\circ$ ) was recorded at different  $\phi$  rotation angles ( $\phi$  was varied in steps of  $1^\circ$ ). The small curvature in the maximum is due to a small physical misalignment of the sample. **d**, Normalized rocking curves ( $\omega$  scans), extracted from the high resolution pole figure, of an as-grown sample (black) and of a sample covered with PECVD  $\text{SiO}_x$  (gray). The full width at half maximum (FWHM) of the peak corresponds to  $0.09^\circ$  for an as-grown sample and to  $0.25^\circ$  after the wires were embedded in  $\text{SiO}_x$ . The small signal at  $\omega=0.5^\circ$  is a detector artefact.

main peak (at every  $\Delta\phi=120^\circ$ ), which would be expected if a fraction of the wires had Shockley partial dislocations (see TEM results below).

The wire/substrate interface of individual wires was investigated by TEM. For this study, a vertical cross section was sliced and thinned with a focused ion beam (FIB). To provide mechanical support during this process, the wires were embedded in a 2-micron-thick  $\text{SiO}_x$  layer, deposited by spin-on process or

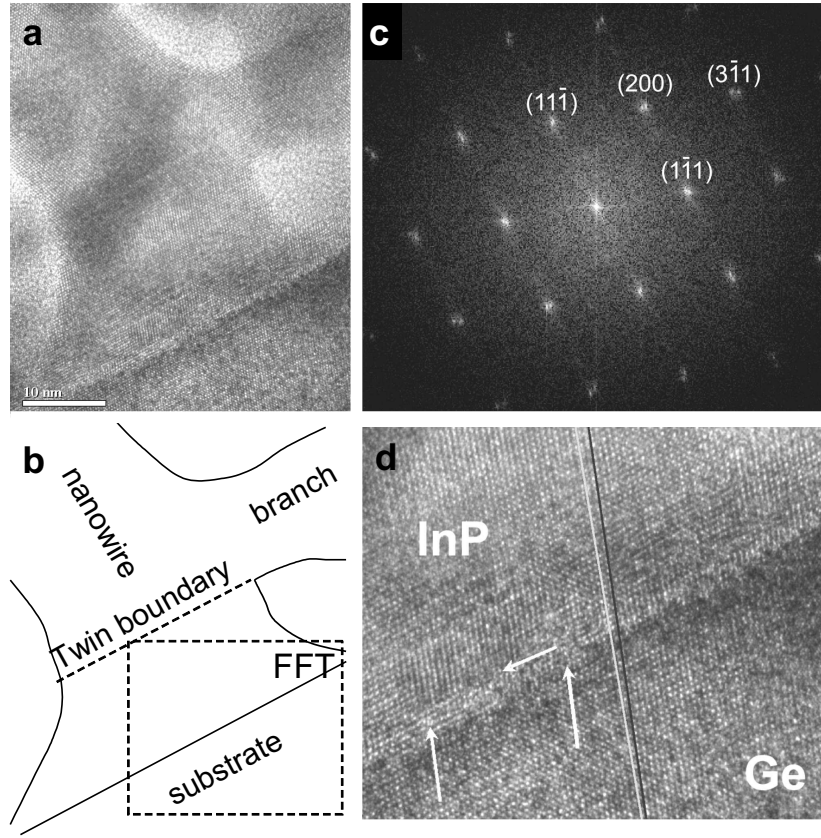


**Figure 4.3:** Transmission electron microscopy (TEM) images of an InP wire on a germanium substrate. **a**, High-resolution TEM image of an InP wire on a Ge(111) substrate. The dark spots are amorphous deposits resulting from the focussed-ion-beam treatment. **b**, Contour drawing of the sample elucidating the geometry in (a). **c**, Fourier transformation (FFT) calculated for the rectangular field delimited by a dashed line in (b). The double spots in the FFT pattern correspond to the InP and Ge reciprocal lattices. **d**, The interfacial area between the InP wire and the Ge crystal. The arrows indicate the locations of three misfit dislocations. The lines parallel to the  $(1\bar{1}1)$  lattice planes of the substrate (black) and the wire (gray) illustrate the counter clockwise lattice tilt of the wires.

by plasma-enhanced chemical vapor deposition (PECVD). Figure 4.3a shows a cross-sectional high-resolution TEM image taken at the base of an InP wire; the epitaxial relation between the nanowire and the substrate is apparent from this image. The wire has a uniform diameter of 21 nm with a significant broadening at the base. The tapering of the base of the wire is a result of the fact that a concave region (wire/surface interface) has to grow much faster than the rest of the crystal face to reduce the surface energy. At 15 nm from the substrate surface a second

(thinner) wire intersects the vertical wire (illustrated in Fig. 4.3b), causing a rotational twin dislocation; no more dislocations can be found further up. We note that similar inspections done on four other wires also showed the epitaxial relation between the wire and the substrate, but did not show such accidental branching. In all these cases, however, the wire-substrate interface is less clear due to poor transparency of the slice or to the damage caused by FIB milling.

A fast Fourier transformation (FFT) of the TEM image was taken on a  $25 \times 25$  nm<sup>2</sup> rectangular field across the InP/Ge interface (see Fig. 4.3b). Double spots were observed (Fig. 4.3c) corresponding to the InP and Ge reciprocal lattices along the [011] zone axis. The lattice spacings corresponding to the InP wire, as extracted from the FFT pattern, are 0.5% lower than the literature values for InP [19]. This shows that for this wire the InP lattice is almost, but not fully, relaxed within a few nanometers from the Ge substrate. (High-resolution XRD measurements revealed that the crystal lattice parameters of the bulk of the wires correspond to the literature values.)

Additionally, the angle between equivalent spots of Ge and InP was studied. This shows that the InP lattice is rotated  $1.4 \pm 0.3^\circ$  around the [011] zone-axis with respect to the Ge lattice. A similar lattice tilt angle was observed in the four other wires studied by high-resolution TEM. In Fig. 4.3d the interfacial area is shown in detail. The arrows point to the position of three misfit dislocations, one parallel to the surface, and two parallel to the (1 $\bar{1}$ 1) planes. The parallel dislocation, which is a result of an inserted lattice plane parallel to the substrate surface, leads to the tilt of the wire crystal lattice with respect to that of the substrate. This combination of Shockley partial dislocations (SPD) has been indicated as a mechanism to accommodate strain in Si-Ge systems [20].

The presence of SPDs in all the wires studied by TEM contrasts the previously discussed XRD results for the as-grown samples, where no traces of such dislocations were found. In order to investigate the role of sample processing we compared XRD measurements done before and after SiO<sub>x</sub> deposition. No relevant changes were found in the pole figures, except for a broadening of the peaks in the high-resolution pole measurements, which could be ascribed to a small fraction of bent wires (Fig. 4.2d). Since no evidence of a tilt was found in the XRD experiments we conclude that SPDs were induced during the FIB process. The atomic layers closest to the heterointerface of the as-grown nanowires are under compressive strain, which can relax during sample preparation via the introduction of SPDs.



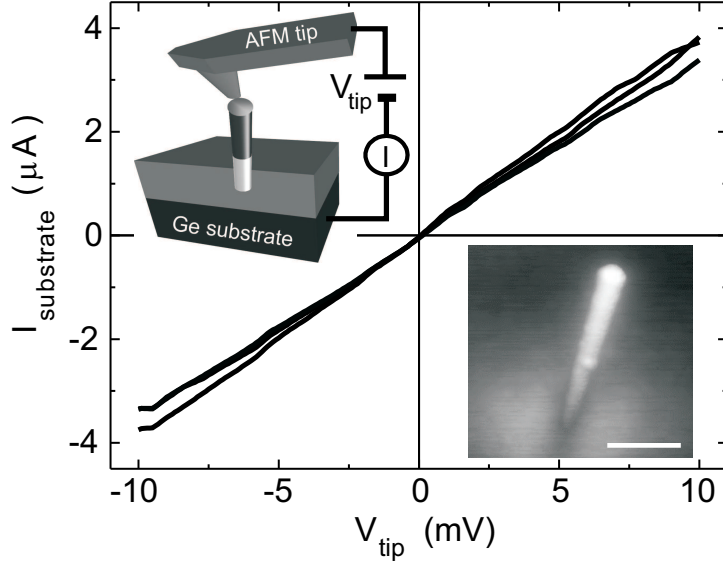


**Figure 4.4:** Transport measurements through an epitaxially grown nanowire by means of an Atomic-force microscope (AFM). Current-voltage curves of a single n-type InP nanowire grown on n-type Ge(111). The three traces were taken on the same wire after lifting and repositioning the conducting AFM tip on the catalytic particle. Inset (top): Schematics of the measurement configuration. Inset (bottom): AFM image of an InP nanowire grown on n-type Ge(111). The scale bar corresponds to 250 nm.

### 4.3 Electrical measurements

The structural studies presented so far demonstrate that crystalline InP nanowires can be epitaxially grown on a Ge substrate, despite the substantial lattice mismatch. The next step is to prove that the heterointerface can form a good (low-resistance) electrical connection between the wire and the substrate. This is the premise for an efficient electrical integration between III-V vertical devices (light-emitting diodes, lasers, or gate-around transistors [21]) with the group-IV substrate. To address this important issue, we used Se-doped n-type InP nanowires on n-type Ge(111). The wires were partially embedded in an insulating poly(methylmethacrylate) (PMMA) layer deposited by spin-coating (1000 rpm) and annealed at 175°C. Figure 4.1b shows an SEM image of a sample provided with a 100 nm PMMA layer. Evidently, many wires protrude from the PMMA layer and have preserved their orientation even after the spin-coating process.

Electrical transport measurements through individual wires were performed in an atomic-force microscopy (AFM) set-up. A platinum-coated AFM tip was scanned in contact mode over the surface, while a tunable dc voltage was simul-

taneously applied between the tip and the back of the Ge substrate (Fig. 4.4). A non-zero current through the substrate was measured when an electrical contact was established between the tip and the catalytic metal particle at the top a nanowire. Because of PMMA residues, the resistance varied from place to place on the catalyst particle. Current-voltage characteristics of tens of individual wires were measured, yielding resistance values down to a few k $\Omega$ . This value represents an upper limit for the wire/substrate interface resistance, which corresponds to a very low contact resistivity of less than  $\sim 10^{-8}\Omega\text{cm}^2$ . This low-resistance Ohmic behaviour can be explained by the relatively small ( $\sim 40$  meV) conduction band offset between Ge and InP [22] and by the deliberately high doping levels ( $10^{18}$ - $10^{19}\text{ cm}^{-3}$ ) in both the InP wires and the Ge substrate. Since Ge is preferentially an n-type dopant for InP [23, 24] we expect that a very good electrical contact can also be achieved with moderately doped InP wires by means of interdiffusion.

The current progress in growing strain-relaxed germanium layers on silicon wafers [25] implies that III-V semiconductor nanowires can be combined structurally and electrically with silicon technology. This represents an important step towards the final goal of bringing new materials and hence new device architectures into silicon-based integrated circuits. However, the most desirable goal of epitaxially growing III-V nanowires directly on silicon remains still unattained. Besides the problem of a suitable procedure for oxide-free surface preparation, the limits to the lattice mismatch for heteroepitaxial nanowire growth should be explored (e.g. the lattice parameter of InP is 8.7% larger than that of Si). The VLS growth of ternary compound semiconductor nanowires [26] may be a way to engineer the lattice parameter and overcome possible limitations coming from an exceedingly high lattice mismatch. Based on the results of this work, and the versatility of the VLS method, we believe that the growth of III-V semiconductor wires directly on silicon is now a step closer.

## References

- [1] Berg, A. A. & Dean, P. J. Light-Emitting Diodes. Clarendon, Oxford (1976).
- [2] Nguyen, L. D., Larson, L. E. & Mishra, U. K. Ultra-high speed modulation-doped field-effect transistor. A tutorial review. *Proc. of the IEEE* **80**, 494-518 (1992).
- [3] Eisenbeiser, K., Huang, J-H., Salih, A., Hadizad, P. & Pitts, B. Manufacturable GaAs VFET for power switching applications. *IEEE Elec. Dev. Letters* **21**, 144-145 (2000).
- [4] Krost, A., Heinrichsdorf, F. & Bimberg, D. InP on Si(111): Accomodation of lattice mismatch and structural properties. *Appl. Phys. Lett.* **64**, 769-771 (1994).
- [5] Carlin, J. A., Ringel, S. A., Fitzgerald, E. A., Bulsara, M. & Keyes, B. M. Impact of GaAs buffer thickness on electronic quality of GaAs grown on graded Ge/GeSi/Si substrates. *Appl. Phys. Lett.* **76**, 1884-1886 (2000).
- [6] Shichijo, H., Matyi, R., Taddiken, A. H. & Kao, Y. C. Monolithic integration for co-integration of GaAs MESFET and silicon CMOS devices and circuits. *Trans. on the IEEE Elec. Dev.* **37**, 548-555 (1990).
- [7] Wagner, R. S. & Ellis, W. C. Vapor-liquid-solid mechanism of single crystal growth. *Appl. Phys. Lett.* **4**, 89-90 (1964).
- [8] Björk, M. T. et al. One-dimensional heterostructures in semiconductor nanowhiskers. *Appl. Phys. Lett.* **80**, 1058-1060 (2002).
- [9] Wu, Y., Fan, R. & Yang, P. Block-by-block growth of single-crystalline Si/SiGe superlattice nanowires. *Nano Lett.* **2**, 83-86 (2002).
- [10] Ertekin, E., Greaney, P. A., Sands, T. D. & Chrzan, D. C. Equilibrium analysis of lattice-mismatched nanowire heterostructures. *Mat. Res. Soc. Symp. Proc.* **737**, F10.4.1-6 (2003).
- [11] Zervos, M. & Feiner, L. F. Electronic structure of piezoelectric double-barrier InAs/InP/InAs/InP/InAs (111) nanowires. *J. Appl. Phys.* **95**, 281-291 (2004).
- [12] Givargizov, E. I. Periodic instability in whisker growth. *J. of Cryst. Growth* **20**, 217-226 (1973).
- [13] Givargizov, E. I. Fundamental aspects of VLS growth. *J. of Cryst. Growth* **31**, 20-30 (1975).
- [14] Hiruma, K. et al. Growth and optical properties of nanometer-scale GaAs and InAs whiskers. *J. Appl. Phys.* **77**, 447-462 (1995).

- [15] Kamins, T. I., Li, X., Williams, R. S. & Liu, X. Growth and structure of chemically vapor deposited Ge nanowires on Si substrates. *Nano Lett.* **4**, 503-506 (2004).
- [16] Zhong, Z., Qian, F., Wang, D. & Lieber, C. M. Synthesis of p-type Gallium Nitride nanowires for electronic and photonic nanodevices. *Nano Lett.* **3**, 343-346 (2003).
- [17] Huang, M. H. et al. Room-temperature ultraviolet nanowire nanolasers. *Science* **292**, 1897-1899 (2001).
- [18] Bakkers, E. P. A. M. & Verheijen, M. A. Synthesis of InP nanotubes. *J. Am. Chem. Soc.* **125**, 3440-3441 (2003).
- [19] Handbook of chemistry and physics. edited by Lide, D. R. CRC Press (1995).
- [20] Horn-von Hoegen, M., LeGoues, F. K., Copel, M., Reuter, M. C. & Tromp, R. M. Defect self-annihilation in surfactant-mediated epitaxial growth. *Phys. Rev. Lett.* **67**, 1130-1133 (1991).
- [21] Wong, H. S. P. Beyond the conventional transistor. *IBM J. Res. & Dev.* **46**, 133-167 (2002).
- [22] Ruan, Y. C. & Ching, W. Y. An effective dipole theory for band lineups in semiconductor heterojunctions. *J. Appl. Phys.* **62**, 2885-2897 (1987).
- [23] Yu, K. M., Moll, A. J. & Walukiewicz, W. Amphoteric behavior and precipitation of Ge dopants in InP. *J. Appl. Phys.* **80**, 4907-4915 (1996).
- [24] Krinhøj, P., Hansen, J. L. & Shiryaev, S. Y. Structural and electrical characteristics of Ge and Se implanted InP after thermal annealing. *J. Appl. Phys.* **72**, 2249-2255 (1992).
- [25] Sakai, A., Tatsumi, T. & Aoyama, K. Growth of strain-relaxed Ge films on Si(001) surfaces. *Appl. Phys. Lett.* **71**, 3510-3512 (1997).
- [26] Duan, X. & Lieber, C. M. General synthesis of compound semiconductor nanowires. *Adv. Mat.* **12**, 298-302 (2000).

# Chapter 5

## Single-electron tunneling in InP nanowires

S. De Franceschi, J. A. van Dam, E. P. A. M. Bakkers,  
L. F. Feiner, L. Gurevich, & L. P. Kouwenhoven

We report on the fabrication and electrical characterization of field-effect devices based on wire-shaped InP crystals grown from Au catalyst particles by a vapor-liquid-solid process. Our InP wires are n-type doped with diameters in the 40–55 nm range and lengths of several  $\mu\text{m}$ . After being deposited on an oxidized Si substrate, wires are contacted individually via e-beam fabricated Ti/Al electrodes. We obtain contact resistances as low as  $\sim 10\text{ k}\Omega$ , with minor temperature dependence. The distance between the electrodes varies between 0.2 and 2  $\mu\text{m}$ . The electron density in the wires is changed with a back gate. Low-temperature transport measurements show Coulomb-blockade behavior with single-electron charging energies of  $\sim 1\text{ meV}$ . We also demonstrate energy quantization resulting from the confinement in the wire.

---

This chapter has been published in Applied Physics Letters.

## 5.1 Introduction

Chemically synthesized semiconductor nanowires (or nanowhiskers) attract increasing interest as building blocks for a bottom-up approach to the fabrication of nanoscale devices and sensors. A key property of these material systems is the unique versatility in terms of geometrical dimensions and composition. Nanowires have already been grown from several semiconductor materials (group-IV elements [1, 2], III-V [3, 4, 5, 6] and II-VI compounds [7]), including structures with variable doping and composition, such as n-type/p-type InP [8], InAs/InP [5], GaAs/GaP [8], and Si/SiGe [2]. The growth technique is based on the vapor-liquid-solid (VLS) process [9] occurring at metallic catalysts, such as nanometer-sized Au particles. The nanowire diameter is set by the catalyst dimension, typically 10–100 nm. The nanowire length is proportional to the growth time and can exceed hundreds of microns. The semiconductor is provided either by metalorganic vapor-phase sources [3, 5], or by laser ablation [10]. Many room-temperature applications have already been shown, such as single-nanowire field-effect transistors (FETs) [4], diodes [8], and logic gates [11] combining both n-type and p-type nanowires. Nanowire heterostructures have been operated as resonant tunneling diodes at 4.2 K [12]. Yet, the low-temperature properties of nanowires and their potential for novel quantum devices are still widely unexplored.

## 5.2 Device fabrication

In this Letter we describe the realization of FET devices from individual n-type InP nanowires. We discuss their transport properties down to 0.35 K, where single-electron tunneling and quantum effects play a dominant role. We also provide details on the fabrication of the electrical contacts to the nanowires, a crucial aspect of the present work. Our InP nanowires are grown via the laser-assisted VLS method. A pulsed laser (193-nm ArF laser, 10 Hz, 100 mJ/pulse) is used to ablate from a pressed InP powder enriched with 1 mol% of Se, which acts as a donor impurity in InP. Nanowires grow from Au seeds formed after annealing a 2 Å-equivalent Au film deposited on a Si substrate with a superficial native oxide. During growth time ( $\sim 30$  min) the substrate temperature is kept at 475°C. The resulting nanowires are 5–10  $\mu\text{m}$  long with a diameter of 40–55 nm.

Immediately after growth, the nanowires are dispersed in Chlorobenzene. A few droplets of this dispersion are deposited on a  $\text{p}^+$  Si substrate with a 250-nm-thick  $\text{SiO}_2$  overlayer. To favor the adhesion of the nanowires, the surface is

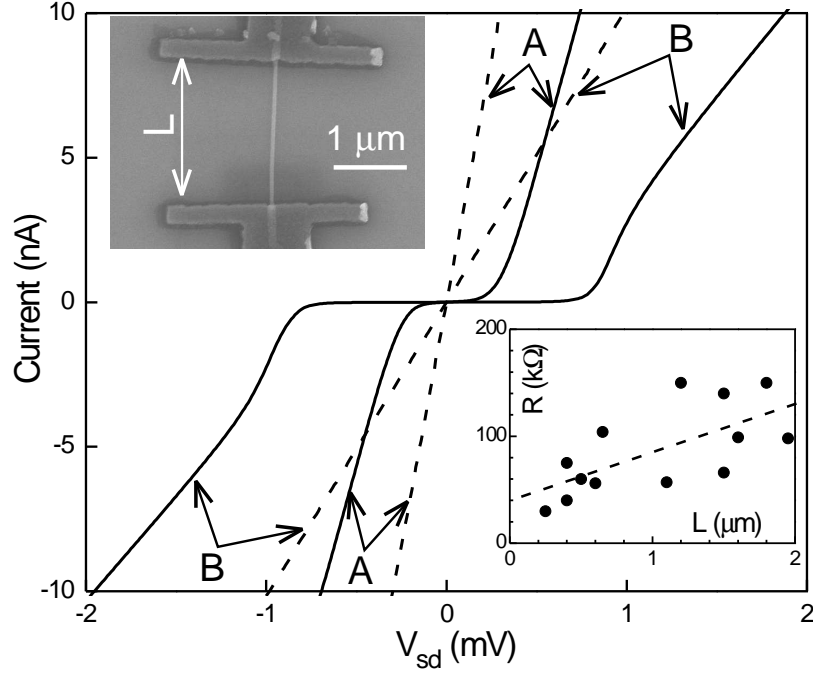


**Figure 5.1:** Current-voltage characteristics at room temperature (dashed lines) and 0.35 K (solid lines), for devices A and B. Upper inset: scanning-electron micrograph of device B. Lower inset: length dependence of the room-temperature source-drain resistance. Each solid circle refers to a different device. The dashed line is a linear fit.

functionalized with a self-assembled monolayer of 3-aminopropyltriethoxysilane (APTES) [13]. Optical imaging is used to locate the nanowires with respect to a reference pattern of predefined Pt markers. The nanowires are then individually contacted with a pair of metal electrodes (source and drain leads) defined by electron-beam lithography (see upper inset to Fig. 5.1). The distance,  $L$ , between the source and drain electrodes is varied between 0.2 and 2  $\mu\text{m}$ .

The contact electrodes consist of thermally evaporated Ti(100 nm)/Al(20 nm). Before metal deposition, samples are treated with BHF for 20 s in order to etch the oxide layer around the nanowires [14]. As-deposited contacts show high resistance, typically in excess of 10 G $\Omega$ . The contact resistance improves drastically after forming-gas rapid-thermal annealing at 475°C for 60 s (for a discussion of the interface reaction between Ti and InP we refer to Ref [15]). We have characterized over ten devices at different temperatures,  $T$ . At room temperature, current-voltage ( $I - V$ ) characteristics are linear (see dashed lines in Fig. 5.1) with resistances,  $R$ , as low as 30 k $\Omega$ . Despite sample-to-sample fluc-

tuations,  $R$  appears to increase with  $L$ , as shown in the lower inset to Fig. 5.1. A linear fit yields  $R = 40 \text{ k}\Omega + 45 \text{ k}\Omega/\mu\text{m} \times L$ , where the constant term and the slope coefficient can be taken as rough estimates of the total contact resistance and the wire resistivity, respectively.

### 5.3 InP nanowire Quantum Dots

Below a few Kelvin, the  $I - V$  characteristics develop a non-linearity around zero bias. This behavior, common to all measured devices, is shown in Fig. 5.1 for device *A* ( $L = 0.20 \mu\text{m}$ ), and *B* ( $L = 1.95 \mu\text{m}$ ), respectively the shortest and longest devices measured. The zero-bias suppression of the conductance has a pronounced dependence on the voltage,  $V_g$ , applied to the  $\text{p}^+$  Si substrate. This is a characteristic fingerprint of Coulomb-blockaded transport which becomes dominant at low temperatures. In fact, an electronic island, formed inside the nanowire segment between source and drain electrodes, leads to Coulomb blockade of transport when  $k_B T < e^2/C$ , where  $C$  is the total capacitance of the island [16]. At source-drain voltages,  $V_{sd}$ , larger than  $e/C$ , the slope of the low- $T$  trace is close to the corresponding room- $T$  value, indicating little  $T$ -dependence of the contact resistance.

Figure 5.2a shows conductance,  $G$ , versus  $V_g$  for device *C* ( $L = 0.65 \mu\text{m}$ ) and *D* ( $L = 1.6 \mu\text{m}$ , inset). Both traces exhibit sharp peaks corresponding to Coulomb-blockade oscillations. This clearly demonstrates that we have achieved single-electron control over the electronic charge and the transport properties of the nanowire. The Coulomb peaks have irregularly distributed sizes, and their  $V_g$ -spacing varies considerably, suggesting the formation of more than one electronic island along the nanowire. This interpretation is supported by the measurement shown in Fig. 5.2b where the differential conductance,  $dI/dV_{sd}$ , of device *C* is plotted on gray scale as a function of  $(V_g, V_{sd})$ . In this plot, Coulomb blockade takes place within dark regions with the characteristic diamond shape. In some cases, such as for  $V_g$  between  $-40$  and  $-90 \text{ mV}$ , Coulomb diamonds are clearly separated from each other and have all their edges fully defined. This is characteristic of Coulomb-blockaded transport through a single electronic island. In other  $V_g$ -regions, however, diamonds overlap with each other, as we would expect for a nanowire containing more than one (most likely two) islands in series. The  $V_g$ -dependent alternation of single- and double-island regimes, shown in Fig. 5.2b, is representative of the general behavior in our devices. We would like to stress that such charge reconfigurations are found to be very stable and reproducible.



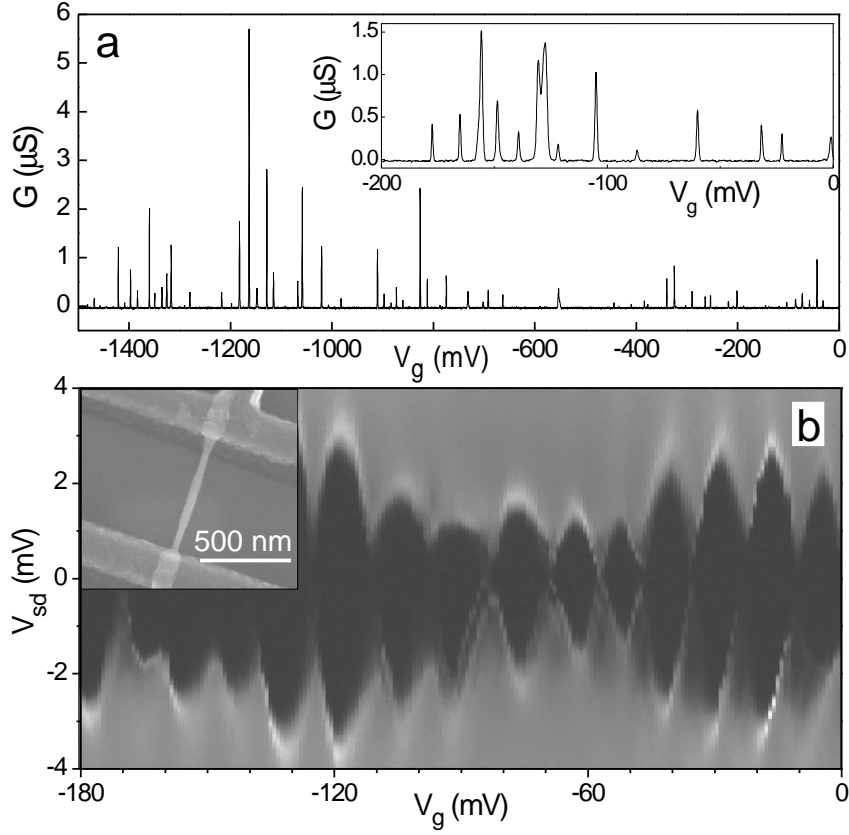


**Figure 5.2:** (a) Conductance,  $G$ , versus back-gate voltage,  $V_g$ , measured at 0.35 K with a dc bias  $V_{sd} = 20\mu\text{V}$ . The two traces refer to device C, and D (inset). (b) Gray-scale plot of differential conductance,  $dI/dV_{sd}$ , versus  $(V_g, V_{sd})$ .  $dI/dV_{sd}$  increases when going from dark to light gray. The measurement refers to device C, and was taken at 0.35 K with lock-in technique at an ac bias excitation of  $20\mu\text{V}$ . Inset: scanning-electron micrograph of device C.

Each Coulomb diamond is associated with a well-defined number of confined electrons,  $N$ . From the half-height (along  $V_{sd}$ ) of the diamonds we estimate a charging energy  $e^2/C \sim 1\text{ meV}$ . The  $V_g$ -width of the diamonds is around 10–20 mV, from which we deduce  $C_g/C \sim 1/7$ , where  $C_g$  is the capacitance to the back gate [17]. This implies that  $N$  decreases by  $\sim 100$  when moving from right to left in Fig. 5.2a. Based on separate studies, we believe this is only a small fraction of the total amount of conduction electrons in the nanowire.

## 5.4 Excited state spectroscopy

We now focus on a small  $V_g$ -range where device  $C$  exhibits single-island behavior. Figure 5.3 shows several  $dI/dV_{sd}$ -vs- $V_g$  traces taken at different values of  $V_{sd}$  between 0 and  $-0.6$  mV. The lowest trace ( $V_{sd} = 0$ ) shows two Coulomb peaks denoting transitions between successive charge states: say from  $N - 1$  to  $N$  (left peak), and from  $N$  to  $N + 1$  (right peak).

At finite bias, each peak in  $dI/dV_{sd}$  splits proportionally to  $V_{sd}$ , as expected from ordinary Coulomb-blockade theory. The left-moving (right-moving) split-peak corresponds to the onset of tunneling from (to) the source (drain) lead. Interestingly, at larger  $V_{sd}$  extra resonances appear between the split-peaks. Increasing  $V_{sd}$ , the  $V_g$ -positions of such resonances evolve parallel to one of the split-peaks, as emphasized by dashed lines. We recognize this behavior as characteristic of transport through a quantum-dot with a discrete energy spectrum [18]. The two extra resonances can be readily explained as the result of tunneling processes involving excited states of the quantum dot. The resonance on the right side of Fig. 5.3 denotes the onset of tunneling from the source lead to the first excited state with  $N + 1$  electrons (see top-right inset). The one on the left can be ascribed to the tunneling of an electron from the dot to the drain which leaves the dot in an excited state with  $N - 1$  electrons (see top-left inset). The bias voltage for which the resonance associated to an  $N$ -electron excited-state begins to emerge is a direct measurement of the corresponding excitation energy,  $\Delta E(N)$ . We find  $\Delta E(N - 1) \approx 0.36$  meV and  $\Delta E(N + 1) \approx 0.30$  meV.

Another sign of energy quantization is based on the  $T$ -dependence of the conductance peaks at  $V_{sd} = 0$ . As expected for single-electron tunneling in quantum dots, lowering  $T$  gives an increased peak height as a result of resonant tunneling [16]. This is in fact observed in the low- $T$  limit (data not shown). The full-width at half maximum increases linearly with  $T$ , but with two different slopes, associated with the quantum ( $k_B T < \Delta E$ ) and the classical ( $k_B T > \Delta E$ ) regime [19]. In our case, the transition between the two regimes occurs at about 1.2 K, (see Fig. 5.3b) corresponding to  $\Delta E \sim 0.1$  meV, in agreement with the previous findings. Our observation of a discrete energy spectrum represents an important premise for a deeper investigation of quantum phenomena and the development of controllable quantum devices based on semiconductor nanowires.

We thank T. Nolst Trenité and S. Tarucha for help and discussions. We acknowledge financial support from the Specially Promoted Research, Grant-in-Aid for Scientific Research, from the Ministry of Education, Science and Culture in Japan, and from the Dutch Organisation for Fundamental Research on Matter (FOM).

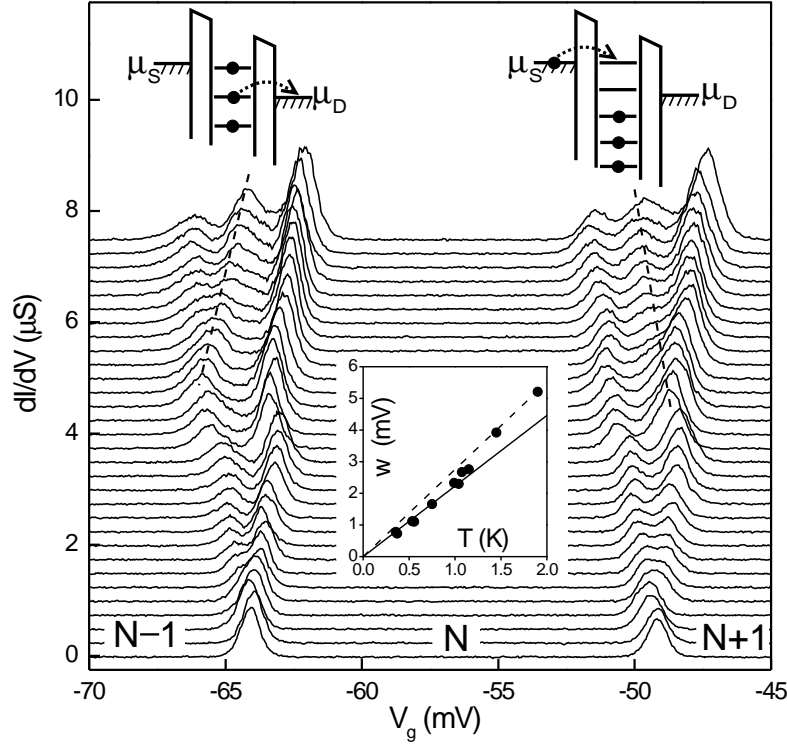


**Figure 5.3:**  $dI/dV_{sd}$  vs  $V_g$ , for different dc values of  $V_{sd}$ , from 0 (lower trace) to  $-0.6$  mV (upper trace) in steps of  $-0.02$  mV. Dashed lines indicate the evolution of the peaks associated with tunneling via excited states. A simplified picture of the corresponding processes is given in the top insets. Bottom inset: full-width at half maximum,  $w$ , vs temperature,  $T$ , for the left Coulomb peak at  $V_{sd} = 0$ . The solid (dashed) line is the theoretical prediction,  $w = (C/eC_g) \times 3.52k_B T$  ( $w = (C/eC_g) \times 4.35k_B T$ ), for the quantum (classical) regime [19]. We used  $C/C_g = 7.35$ , obtained from the  $V_{sd}$ -dependence of the  $V_g$ -splitting.

## References

- [1] Y. Cui and C. M. Lieber, *Science* **291**, 851 (2001).
- [2] Y. Wu, R. Fan, and P. Yang, *Nano Lett.* **2**, 83 (2002).
- [3] K. Hiruma, M. Yazawa, T. Katsuyama, K. Ogawa, K. Haraguchi, M. Koguchi, and H. Kakibayashi, *J. Appl. Phys.* **77**, 447 (1995).
- [4] X. Duan, Y. Huang, Y. Cui, J. Wang, and C. M. Lieber, *Nature* **409**, 66 (2001).
- [5] M. T. Björk, B. J. Ohlsson, T. Sass, A. I. Persson, C. Thelander, M. H.

- Magnusson, K. Deppert, L. R. Wallenberg, and L. Samuelson, Appl. Phys. Lett. **80**, 1058 (2002).
- [6] Y. Huang, X. Duan, Y. Cui, and C. M. Lieber, Nano Lett. **2**, 101 (2002).
- [7] R. Solanki, J. Huo, J. L. Freeouf, and B. Miner, Appl. Phys. Lett. **81**, 3864 (2002).
- [8] M. S. Gudiksen, L. J. Lauhon, J. Wang, D. C. Smith, and C. M. Lieber, Nature (London) **415**, 617 (2002).
- [9] R. S. Wagner and W. C. Ellis, Appl. Phys. Lett. **4**, 89 (1964).
- [10] A. M. Morales and C. M. Lieber, Science **279**, 208 (1998).
- [11] Y. Huang, X. Duan, Y. Cui, L. J. Lauhon, K.-H. Kim, and C. M. Lieber, Science **294**, 1313 (2001).
- [12] M. T. Björk, B. J. Ohlsson, C. Thelander, A. I. Persson, K. Deppert, L. R. Wallenberg, and L. Samuelson, Appl. Phys. Lett. **81**, 4458 (2002).
- [13] J. Liu, M. J. Casavant, M. Cox, D. A. Walters, P. Boul, W. Lu, A. J. Rimerberg, K. A. Smith, D. T. Colbert, and R. E. Smalley, Chem. Phys. Lett. **303**, 125 (1999).
- [14] High-resolution images, obtained by transmission-electron microscopy, revealed an oxide thickness up to 10 nm, with considerable wire-to-wire variations.
- [15] M. B. Takeyama, A. Noya, T. Hashizume, and H. Hasegawa, Jpn. J. Appl. Phys. **38**, 1115 (1999).
- [16] *Single Charge Tunneling*, edited by H. Grabert and M. H. Devoret (Plenum Press, New York, 1992).
- [17] From a simplified model we estimate  $C_g \approx [2\pi\epsilon\epsilon_0/\ln(2d/R)] \times L_0$ , where  $L_0$  is the length of a cylindrical electronic island,  $\epsilon = 4$  (relative dielectric constant for SiO<sub>2</sub>),  $R = 20$  nm (island radius),  $d = 250$  nm (distance to the back gate). Then  $U = e^2/C = 1$  meV and  $C_g/C = 1/7$  yield  $L_0 \approx 0.3 \mu\text{m} \lesssim L$ .
- [18] A. T. Johnson, L. P. Kouwenhoven, W. de Jong, N. C. van der Vaart, C. J. P. M. Harmans, and C. T. Foxon, Phys. Rev. Lett. **69**, 1592 (1992).
- [19] E. B. Foxman, U. Meirav, P. L. McEuen, M. A. Kastner, O. Klein, P. A. Belk, D. M. Abusch, and S. J. Wind, Phys. Rev. B **50**, 14193 (1994).

# Chapter 6

## Tunable supercurrent through semiconductor nanowires

Yong-Joo Doh, Jorden A. van Dam, Aarnoud L. Roest,  
Erik P. A. M. Bakkers, Leo P. Kouwenhoven,  
& Silvano De Franceschi

We have developed a high-yield approach to the fabrication of nanoscale superconductor/semiconductor hybrid devices. The devices are assembled from indium arsenide semiconductor nanowires individually contacted by aluminum-based superconductor electrodes. Below 1 Kelvin, the high transparency of the contacts enables proximity-induced superconductivity. The nanowires form superconducting weak links operating as mesoscopic Josephson junctions with electrically tunable coupling. The supercurrent can be switched on/off by a gate voltage acting on the electron density in the nanowire. A variation in gate voltage induces universal fluctuations in the normal-state conductance which are clearly correlated to critical current fluctuations. The ac Josephson effect gives rise to Shapiro steps in the voltage-current characteristic under microwave irradiation.

---

This chapter has been published in Science.

## 6.1 Introduction

Much of the recent interest in chemically grown semiconductor nanowires arises from their unique versatility which translates into a wide range of potential applications. Many important proofs of concept have already been provided such as field effect transistors, elementary logic circuits, resonant tunneling diodes, light emitting diodes, lasers, and biochemical sensors [1, 2, 3]. These achievements, together with the recent advance in the monolithic integration of III-V nanowires with standard Si technology [4, 5], yield great promise for the development of next-generation (opto-)electronics. Simultaneously, the high degree of freedom in nanowire growth and device engineering creates new opportunities for the fabrication of controlled one-dimensional systems for low-temperature applications and fundamental science. Quantum confinement and single-electron control have been achieved in a variety of single-nanowire devices [6, 7, 8]. In these experiments the transport properties were dominated by Coulomb interactions among conduction electrons due to the presence of high-resistance barriers either at the interface with the metal leads or within the nanowire itself.

Here we address an entirely different regime in which the nanowires are contacted by superconducting electrodes with deliberately low contact resistance. While Coulomb blockade effects are suppressed, the semiconductor nanowires acquire superconducting properties due to the proximity effect, a well-known phenomenon which can be described as the leakage of Cooper pairs of electrons from a superconductor ( $S$ ) into a normal-type conductor ( $N$ ) [9]. The proximity effect takes place only if the  $S$ - $N$  interface is highly transparent to electrons. This requirement is particularly hard to meet when the  $N$  element is a semiconductor, the major obstacle being posed in most cases by the unavoidable presence of a Schottky barrier. In this respect, indium arsenide (InAs) is an exceptional semiconductor since it can form Schottky-barrier-free contacts with metals [10]. This motivates our choice for this material in the present work.

## 6.2 Device fabrication

The InAs nanowires are grown via a catalytic process based on a vapor-liquid-solid mechanism [11]. The nanowires are monocrystalline with diameters in the 40 - 130 nm range and lengths of 3 - 10  $\mu\text{m}$ . From field-effect electrical measurements (discussed below), we find n-type conductivity with an average electron density  $n_s = (2 - 10) \cdot 10^{18} \text{ cm}^{-3}$ , and an electron mobility = 200 - 2000  $\text{cm}^2/\text{Vs}$ . These values correspond to a mean free path,  $l = 10 - 100 \text{ nm}$ . Right after growth, the nanowires are transferred to a  $\text{p}^+$  silicon substrate with a 250-nm-thick  $\text{SiO}_2$

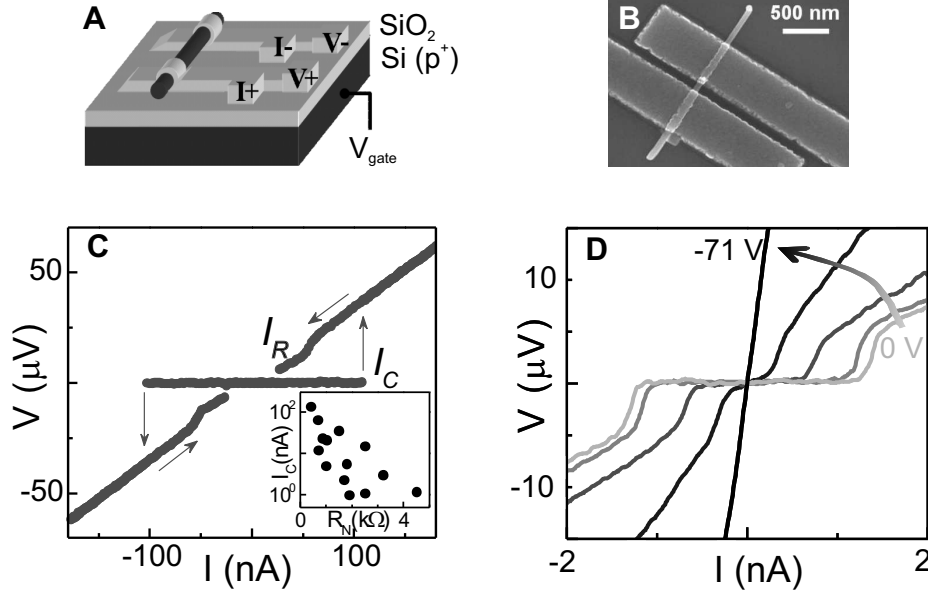


**Figure 6.1:** (A) Schematic representation of a nanowire device. In four-terminal measurements current is driven between I+ and I- and the voltage drop is simultaneously measured between V+ and V-. A gate voltage  $V_g$  is applied to the p<sup>+</sup> Si substrate to vary the electron density in the nanowire. (B) Scanning electron micrograph of a nanowire device. The nanowire diameter is determined by the size of the gold catalytic particle which is visible at the upper end of the nanowire. (C) Voltage-vs-current,  $V(I)$ , characteristic for device no. 1 measured in a four-terminal configuration at  $T = 40$  mK for both increasing and decreasing current bias. Inset: Correlation between  $I_C$  and  $R_N$  (the data points correspond to different devices and  $V_g = 0$  V). (D)  $V(I)$  characteristics of device no. 2 at  $T = 40$  mK for  $V_g = 0, -10, -50, -60, -71$  V (increasing from light gray to black). By making  $V_g$  more negative the critical current is progressively reduced all the way to zero. When the supercurrent vanishes the zero-bias resistance of the device is 70 k $\Omega$ . The characteristic parameters at  $V_g = 0$  V, are  $I_C = 1.2$  nA and  $R_N = 4.5$  k $\Omega$ .

overlayer. The conductive substrate is used as a back gate to vary the electron density in the nanowires. Custom metal electrodes are defined by e-beam lithography followed by e-beam evaporation of Ti(10 nm)/Al(120 nm). Prior to metal deposition the nanowire surface is deoxidized by a 6-s wet etching in buffered hydrofluoric acid. No thermal annealing is performed in order to minimize inter-diffusion at the contacts. The spacing,  $L$ , between the source and drain electrodes is varied between 100 and 450 nm. To perform four-point measurements, both source and drain electrodes are split in two branches as illustrated in Fig. 6.1A. A representative single-nanowire device is shown in Fig. 6.1B.

### 6.3 Gate control of supercurrents through InAs nanowires

The nanowire devices exhibit Ohmic behavior with a normal state resistance,  $R_N$ , in the 0.4 - 4 k $\Omega$  range.  $R_N$  is virtually insensitive to temperature all the way down to the superconducting transition temperature of the Al-based electrodes,  $T_C = 1.1$  K. Below  $T_C$ , the proximity effect manifests itself through the appearance of a dissipation-less supercurrent which can be viewed as a consequence of the diffusion of Cooper pairs throughout the entire length of the nanowire section between the two superconducting electrodes. (This requires the phase-coherence length for electron propagation in the nanowire to be longer or at least comparable to the distance between source and drain contacts.) To investigate this superconductivity regime we performed four-terminal dc measurements, in which the voltage across the nanowire,  $V$ , is measured while sweeping the bias current,  $I$ . In Fig. 6.1C we show a representative measurement taken at base temperature,  $T = 40$  mK. The  $V(I)$  characteristic exhibits a clear supercurrent branch (i.e. a region of zero-resistance) as well as a dissipative quasiparticle branch with a dependence on the sweeping direction of the source-drain current. The switching from superconductive to dissipative conduction occurs when  $I$  approaches a critical current,  $I_C$ , leading to the abrupt appearance of a finite voltage. The reversed switching, from the resistive to the superconductive regime, occurs at a lower current level  $I_R$ . The observed  $V(I)$  characteristics, as well as their hysteretic behavior, are typically found in capacitively shunted Josephson junctions [12]. (In our devices, the shunting capacitors are formed between the source/drain electrodes and the conductive Si substrate.)

The presence of a supercurrent has been assessed in 14 devices (90% yield) with critical currents ranging from a few nA to 135 nA at 40 mK (see Fig. 6.5 for the temperature dependence). On average,  $I_C$  decreases with  $R_N$  (see inset to Fig. 6.1C), and the  $I_C R_N$  product, a typical figure of merit for Josephson junctions, varies between 2 - 60  $\mu$ V. The highest value is comparable to the expectation for an ideal  $S$ - $N$ - $S$  junction embedding a short and diffusive ( $l < L$ ) normal conductor, i.e.  $I_C R_N \sim \Delta_0/e$ , where  $\Delta_0 = 100$ -120  $\mu$ eV is the superconducting energy gap of the contact electrodes obtained from finite-voltage measurements discussed below. The semiconductor nature of the nanowires allows the magnitude of the critical current to be controlled by a voltage,  $V_g$ , applied to the back-gate electrode [13, 14, 15, 16, 17]. Due to their n-type character, a negative  $V_g$  results in a reduction of the electron concentration in the nanowires leading to a higher  $R_N$  and hence a lower  $I_C$ . Thus the nanowires can operate as tunable



superconducting weak links. For sufficiently negative gate voltages,  $I_C$  is entirely suppressed as shown in Fig. 6.1D, where the "off" state ( $I_C = 0$  nA) is reached for  $V_g \sim -70$  V. This large voltage is due to the weak capacitive coupling between the nanowire conducting channel and the back gate. The use of alternative gating geometries, such as local top gates or gate-around configurations, would provide a much stronger coupling and, at the same time, the possibility to individually control different nanowires on the same chip. This allows a bottom-up assembly of superconducting integrated circuits based on independently addressable  $S$ - $N$ - $S$  elements.

To gain more insight in the Josephson behavior of the nanowire  $S$ - $N$ - $S$  junction, we investigate the effect of an external microwave field. Due to phase locking between the microwave angular frequency,  $\omega_{rf}$ , and the voltage-dependent Josephson frequency [18],  $\omega_J = 2eV/\hbar$ , the  $V(I)$  characteristic exhibits voltage plateaus at  $V_n = n\hbar\omega_{rf}/2e$ , the so-called Shapiro steps [12] (here  $\hbar$  is Planck's constant,  $e$  is the electron charge, and  $n=0, \pm 1, \pm 2, \dots$ ). A representative set of plateaus (up to  $|n|=4$ ) is shown in Fig. 6.2A in the case of 4 GHz radiation. A  $V(I)$  curve for the same device in the absence of the microwave field is also shown for direct comparison. We vary the microwave frequencies in the 2 - 10 GHz range in order to verify the proportionality relation between the step height,  $\Delta V$  and  $\omega_{rf}$ . As shown in the inset of Fig. 6.2A, the experimental values fall on top of the expected linear dependence  $\Delta V = (\hbar/2e)\omega_{rf}$ . By increasing the microwave field, proportional to the square root of the externally applied microwave power,  $P_{rf}$ , higher order steps become progressively visible and their step width,  $\Delta I_n$ , exhibits quasi-periodic oscillations. This behavior emerges clearly in a plot of differential resistance,  $dV/dI$ , as a function of  $P_{rf}^{1/2}$  and source-drain current. In Fig. 6.2B we show an example of such plots corresponding to the same microwave frequency (4 GHz). The Shapiro steps appear as dark regions ( $dV/dI = 0$ ) separated by bright (high  $dV/dI$ ) lines corresponding to the sharp boundary between consecutive steps. The wiggling behavior of these lines reflects the quasi-periodic oscillations in  $\Delta I_n$ . These oscillations are quantitatively shown in Fig. 6.2C for  $n=0$  to 4. We find good agreement with the theoretical expectation  $I_n = 2I_C |J_n(2e\nu_{rf}/\hbar\omega_{rf})|$  [12], where  $J_n$  is the  $n^{th}$  order Bessel function and  $\nu_{rf}$  is the amplitude of rf voltage across the nanowire junction.  $I_C$  and a scaling factor,  $\alpha$ , for the horizontal axis ( $\nu_{rf} = \alpha P_{rf}^{1/2}$ ) are the only fitting parameters for all of the five theoretical curves. The observed Shapiro steps represent clear evidence of genuine Josephson coupling through the nanowire.

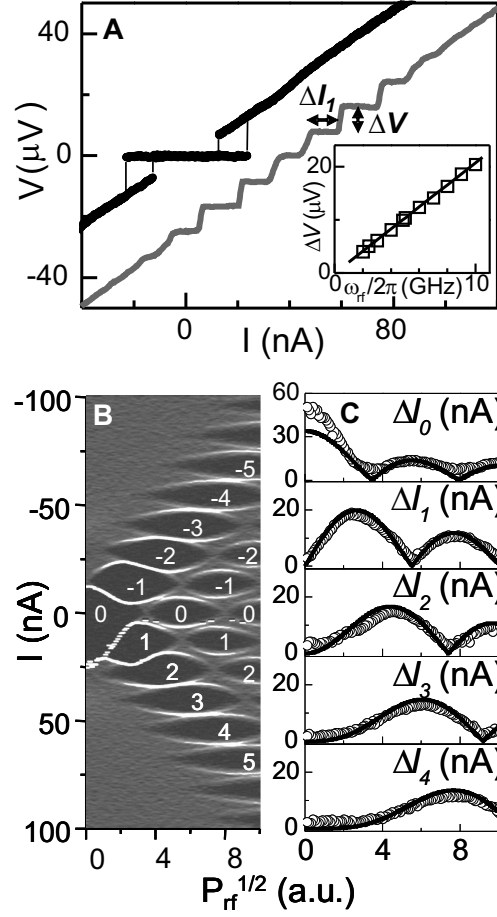


**Figure 6.2:** (A)  $V(I)$  characteristics for device no. 3 at 40 mK, with (gray) and without (black) an externally applied 4-GHz radiation (this device has  $R_N = 860 \, \Omega$  and  $I_C = 26 \, \text{nA}$  at  $T = 40 \, \text{mK}$ ). The gray trace is horizontally offset by 40 nA. The applied microwave radiation results in voltage plateaus (Shapiro steps) at integer multiples of  $\Delta V = 8.3 \, \mu\text{V}$ . Inset: Measured voltage spacing  $\Delta V$  (symbol) as a function of microwave angular frequency  $\omega_{rf}$ . The solid line (theory) shows the agreement with the ac Josephson relation  $\Delta V = \hbar\omega_{rf}/2e$ . (B) Differential resistance,  $dV/dI$ , plotted on gray scale as a function of the bias current,  $I$ , and the square root of the microwave excitation power,  $P_{rf}$ . In this plot the microwave frequency is fixed at 4 GHz. The voltage plateaus at  $V_n = n\hbar\omega_{rf}/2e$  appear as black regions ( $dV/dI = 0$ ) labeled by the corresponding integer index,  $n$ . These regions are delimited by bright lines (high  $dV/dI$ ) corresponding to the sharp increase of the  $V$  between consecutive plateaus. For lower frequencies we have also observed half-integer steps, i.e.  $n = 1/2, 3/2, \dots$  (see Fig. 6.7). (C) Current width  $\Delta I_n$  of the  $n$ -th Shapiro steps ( $n = 0, 1, 2, 3, 4$ ) versus  $P_{rf}^{1/2}$  as extracted from (B). The five solid lines are Bessel-type functions obtained from a single two-parameter fit (see text).

## 6.4 Mesoscopic properties of InAs nanowire junctions

We now discuss in more detail the basic properties of the  $S$ - $N$ - $S$  nanowire devices and elucidate their mesoscopic nature. At the onset of the quasi-particle branch (i.e. just above  $I_C$ ) the device conductance is found to be higher than the normal-state value  $G_N = 1/R_N$ . This is apparent from the slope of the wide-range  $I(V)$  characteristic shown in the inset of Fig. 6.3A (gray trace). Only for  $V > 0.3$  mV the slope changes to the normal-state value as becomes clear by a comparison with an  $I(V)$  trace taken at 100 mT (black trace), a magnetic field high enough to suppress superconductivity in the electrodes. Evidently, the high-bias linear  $I(V)$  at zero field does not extrapolate to the origin, as in the normal state, but to a finite excess current  $I_{exc} = 0.23 \mu\text{A}$ . The enhanced conductance at low bias and the consequent excess current provide a clear indication of strong Andreev reflection [19] - an electron above the Fermi energy coming from the  $N$  region is reflected at the  $S$ - $N$  interface as a phase-conjugated hole (i.e., the lack of an electron below the Fermi energy) while creating at the same time a Cooper pair in the  $S$  region. Andreev reflection at the  $S$ - $N$  interface and phase-coherent electron propagation in the normal conductor can be viewed as the microscopic origin of the proximity effect [10, 20]. Being a two-particle process, Andreev reflection requires high interface transparency. Under this condition, it enables electrical conduction at sub-gap voltages, i.e. for  $eV < 2\Delta_0$ , where the factor 2 accounts for the presence of two  $S$ - $N$  interfaces in series. A sub-gap conductance,  $G_{AR}$ , larger than the normal-state value (up to  $2 G_N$ ) can be observed in the case of almost ideal interfaces having a transmission coefficient,  $T_{int}$ , close to unity. Shown in Fig. 6.3A is a plot of the differential conductance,  $dI/dV$ , versus  $V$  for the same nanowire device. We find  $G_{AR}/G_N \approx 1.4$  and from the value of  $I_{exc}$  we estimate  $T_{int} \approx 0.75$  [21]. Similar values are consistently obtained for most of the devices (see Fig. 6.6). This high transparency is in line with the best results ever achieved for micrometer-scale superconductor-semiconductor interfaces [22]. Besides an overall conductance enhancement, the sub-gap regime is characterized by a series of peaks in  $dI/dV$  occurring at  $V = 2\Delta_0/me$  (and  $m = 1, 2, 3$ ) and denoted by vertical arrows. These peaks are due to multiple Andreev processes [23, 24, 25]. Between two consecutive Andreev reflections the motion of electron-like (or hole-like) quasiparticles between the two  $S$ - $N$  interfaces is diffusive ( $l < L$ ) but phase coherent.

This mesoscopic character of the nanowire  $S$ - $N$ - $S$  junctions emerges clearly from a detailed analysis of the  $V_g$ -dependence.  $I_C$  exhibits reproducible and

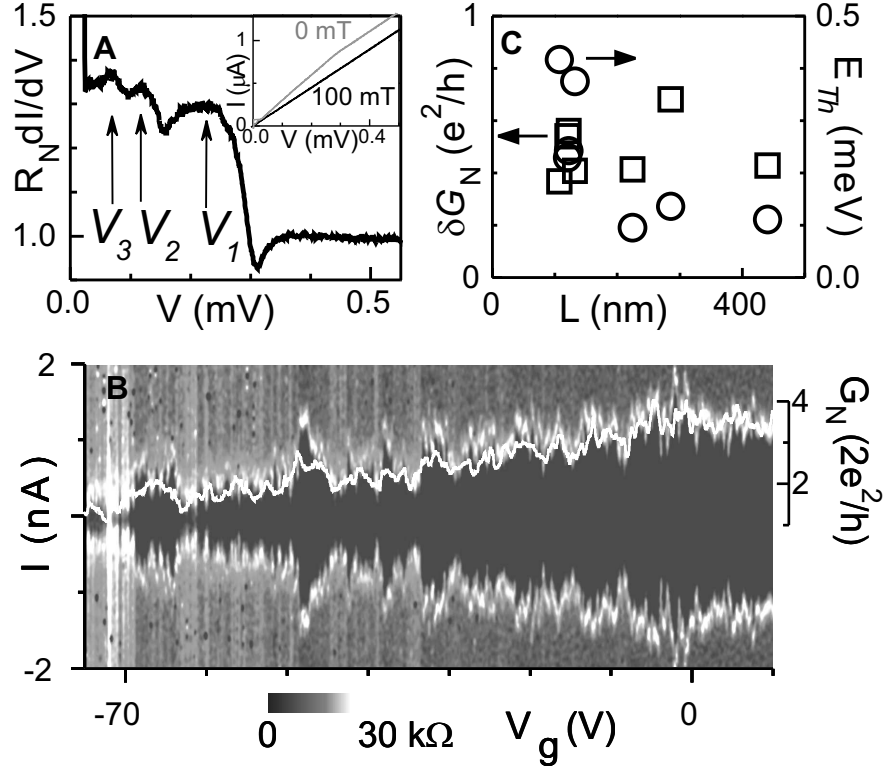


**Figure 6.3:** (A)  $V$ -dependence of the differential conductance,  $dI/dV$ , normalized to the normal-state value  $R_N^{-1}$  for device no. 1. The vertical arrows indicate three  $dI/dV$  maxima at  $V_m = 2\Delta_0/me$  ( $m = 1, 2, 3$ ) due to multiple Andreev reflection. Inset:  $I(V)$  characteristics at 40 mK for zero magnetic field (gray trace) and for 100 mT field perpendicular to the substrate (black trace). The supercurrent branch at zero field is not clearly visible in this large bias range. (B) Differential resistance,  $dV/dI$ , vs. bias current,  $I$ , and gate voltage,  $V_g$ , for device no. 2. As  $V_g$  is varied from 0 to negative values, the supercurrent branch (black region) shrinks and simultaneously exhibits reproducible fluctuations. These fluctuations correlate with those of the normal-state conductance,  $G_N(V_g)$ , as it is shown by the comparison with the superimposed plot (white line) sharing the same horizontal scale. (In practice,  $G_N(V_g)$  is obtained by measuring  $dV/dI$  at  $V > 2\Delta_0/e$ .) (C) The Thouless energy,  $E_{Th}$ , and the rms value,  $\delta G_N$ , of the  $G_N(V_g)$  fluctuations are plotted as a function of the distance,  $L$ , between source and drain contacts.  $E_{Th} = \hbar D/L^2$ , where  $D = lv_F/d$  is the diffusion coefficient for a  $d$ -dimensional conductor expressed in terms of the mean-free path,  $l$ , and the Fermi velocity,  $v_F$ .  $l$  and  $v_F$  are extracted from the mobility and the carrier density obtained from the pinch-off  $G_N(V_g)$  characteristics [6]. Since  $l$  is typically comparable to the nanowire diameter, we take  $d=3$  instead of  $d=1$ . Even with this conservative assumption,  $E_{Th} \geq \Delta_0$ .

time-independent fluctuations. In a color plot of  $dV/dI$  versus  $(V_g, I)$ , shown in Fig. 6.3B, these appear as irregular variations in the  $I$ -width of the zero- $dV/dI$ , supercurrent branch (black region). The superimposed white trace illustrates the evolution of the corresponding normal-state conductance  $G_N$  over the same  $V_g$  range. Interestingly,  $I_C(V_g)$  and  $G_N(V_g)$  fluctuations exhibit a clear correlation which indicates a common physical origin. We interpret these  $G_N(V_g)$  oscillations as universal conductance fluctuations (UCF) [26] associated with the phase-coherent diffusive motion along the nanowire. Similar  $G_N(V_g)$  fluctuations are also found in the other nanowire devices. The corresponding rms amplitudes,  $\delta G_N$ , are reported in Fig. 6.3C. We find an average value of  $0.55 e^2/h$ , which is very close to the expectation for UCF in a phase-coherent quasi one-dimensional conductor ( $\delta G_N = 0.7e^2/h$ ).  $I_C$  fluctuations arising from the diffusive motion of electrons in a disordered weak link have been theoretically addressed for two distinct conditions:  $\Delta_0 \ll E_{Th}$  [27] and  $\Delta_0 \gg E_{Th}$  [28], where  $E_{Th} = \hbar D/L^2$  is the Thouless energy in the normal conductor and  $D$  is the diffusion coefficient. In the first case, which is the most pertinent to the present study (see Fig. 6.3C), a universal limit of  $\delta I_C \sim e\Delta_0/\hbar$  is expected for the rms amplitude of the  $I_C$  fluctuations, in analogy with universal conductance fluctuations in the normal state. Experimentally we find  $\delta I_C = 0.2 - 3$  nA, much smaller than the expected value ( $\sim 25$  nA). This discrepancy could be due to a non ideal interface transparency or to an incomplete screening from the electromagnetic environment.

Finally, we would like to comment on the reproducibility of the results presented above as well as on the prospects for nanowire-based  $S$ - $N$  structures. About 90% of the devices fabricated in this work have a normal-state resistance below a few  $k\Omega$  and exhibit a supercurrent branch at low temperature. This indicates reproducibly low contact resistances, an important requirement for the successful up scaling to even small superconducting circuits incorporating multiple nanowire devices. The functionalities of these circuits could be integrated with conventional silicon technology or with solid-state quantum computer architectures currently under study. For instance, electrically tunable Josephson nanojunctions may be used as building blocks for superconducting quantum interference devices (SQUIDs) in which the circulating supercurrent can be switched on and off by a control voltage. Such devices may serve as switchable coupling elements between superconducting qubits [29, 30]. Several important issues need still to be addressed such as the local gating of individual nanowires and the replacement of aluminum with wider-gap superconductors allowing for higher operation temperatures. We believe, however, that InAs-based semiconductor nanowires can already provide a convenient basis for the development of more complex hybrid nanostructures which may enable the investigation of exotic and

so far elusive phenomena resulting from the interplay between size quantization and different types of electron-electron correlations such as superconductivity, Coulomb interactions, and Kondo-type correlations.

We gratefully acknowledge discussions with J. Eroms, R. Schouten, C. Harman, P. Hadley, Yu. Nazarov, C. Beenakker, T. Klapwijk, B. van Wees, and F. Giazotto. Financial support was obtained from the Dutch Fundamenteel Onderzoek der Materie (FOM), from the Japanese Solution Oriented Research for Science and Technology (SORST) program, and from the Korean Science and Engineering Foundation (KOSEF).

## References

- [1] C. M. Lieber, MRS Bull. **28**, 486 (2003).
- [2] P. Yang, MRS Bull. **30**, 85 (2005).
- [3] L. Samuelson, *et al.*, Physica E **25**, 313-318 (2004).
- [4] E. P. A. M. Bakkers, *et al.*, Nature Materials **3**, 769 (2004).
- [5] T. Mårtensson, *et al.*, Nano Lett. **4**, 1987 (2004).
- [6] S. De Franceschi *et al.*, Appl. Phys. Lett. **83**, 344 (2003).
- [7] M. T. Björk *et al.*, Nano Lett. **4**, 1621 (2004).
- [8] Z. Zhong, Y. Fang, W. Lu, C. M. Lieber, cond-mat/0412756.
- [9] P. G. de Gennes, Rev. Mod. Phys. **36**, 216 (1964).
- [10] B. J. van Wees, Physics World **9** (11), 41 (1996).
- [11] See section 6.5 for details.
- [12] M. Tinkham, Introduction to Superconductivity (McGraw-Hill, Singapore, ed. 2, 1996).
- [13] T. D. Clark, R. J. Prance, A. D. C. Grassie, J. Appl. Phys. **51** 2736 (1980).
- [14] T. Nishino, M. Miyake, Y. Harada, U. Kawabe, IEEE Electron Device Lett. EDL-6, 297 (1985).
- [15] H. Takayanagi, T. Kawakami, Phys. Rev. Lett. **54**, 2449 (1985).
- [16] A.W. Kleinsasser, *et al.*, Appl. Phys. Lett. **55**, 1909 (1989).
- [17] C. Nguyen, J. Werking, H. Kroemer, E.L. Hu, Appl. Phys. Lett. **57**, 87 (1990).
- [18] B. D. Josephson, Phys. Lett. **1**, 251 (1962).

- [19] A. F. Andreev, Zh. Eksp. Theor. Fiz. **46**, 1823 (1964) [Sov. Phys. JETP **19**, 1228 (1964)].
- [20] B. Pannetier, H. Courtois, J. Low. Temp. Phys. **118**, 599 (2000).
- [21] K. Flensberg, J. B. Hansen, M. Octavio, Phys. Rev. B **38**, 8707 (1988).
- [22] A. Chrestin, U. Merkt, Appl. Phys. Lett. **70**, 3149 (1997).
- [23] M. Octavio, M. Tinkham, G. E. Blonder, T. M. Klapwijk, Phys. Rev. B **27**, 6739 (1983).
- [24] E. Scheer *et al.*, Phys. Rev. Lett. **86**, 284 (2001).
- [25] M. R. Buitelaar *et al.*, Phys. Rev. Lett. **91**, 057005 (2003).
- [26] P. A. Lee, A. D. Stone, Phys. Rev. Lett. **55**, 1622 (1985).
- [27] C. W. J. Beenakker, Phys. Rev. Lett. **67**, 3836 (1991).
- [28] B. L. Al'tshuler, B. Z. Spivak, Zh. Eksp. Theor. Fiz. **92**, 609 (1987) [Sov. Phys. JETP **65**, 343 (1987)].
- [29] Y. Makhlin, G. Schön, A. Shnirman, Rev. Mod. Phys. **73**, 357 (2001).
- [30] M. J. Storcz, F. K. Wilhelm, Appl. Phys. Lett. **83**, 2387 (2003).

## 6.5 Appendix

The nanowires are grown epitaxially on InP and InAs (001) substrates. The catalytic particles form spontaneously from a 2-Å equivalent gold layer deposited on the surface of the substrate. This occurs by self aggregation when the substrate approaches the growth temperature (450°C). The size of the gold particles ranges from a few tens to about 100 nm causing a spread in nanowire diameters. The vapor-liquid-solid growth process takes place at the catalytic particle [1]. The semiconductor is provided to the vapor phase (an argon gas flow) by pulsed laser ablation (193 nm ArF laser, 10 Hz, 100 mJ/pulse) of a nominally undoped InAs target [2,3]. The single-crystalline structure is assessed by high-resolution transmission-electron microscopy (TEM).

### References

- [1] R. S. Wagner, W. C. Ellis, Appl. Phys. Lett. **4**, 89 (1964).
- [2] M.S.Gudiksen, J.F. Wang, C.M. Lieber, J. Phys. Chem. B **105**, 4062 (2001).
- [3] E.P.A.M. Bakkers, M.A. Verheijen, J. Am. Chem. Soc. **125**, 3440 (2003).
- [4] Lehnert *et al.*, Phys. Rev. Lett. **82**, 1265 (1999).

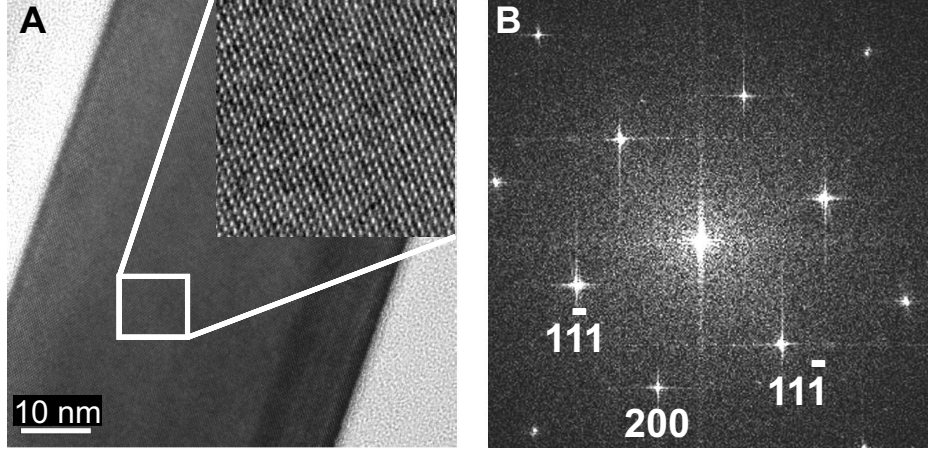


**Figure 6.4:** (A) A representative high-resolution transmission-electron microscopy image. Crystal defects such as twin boundaries or other dislocations are rarely seen. (B) Fast Fourier transformation of Fig. 6.4A. The nanowire longitudinal axis (growth direction) is  $\langle 100 \rangle$ .

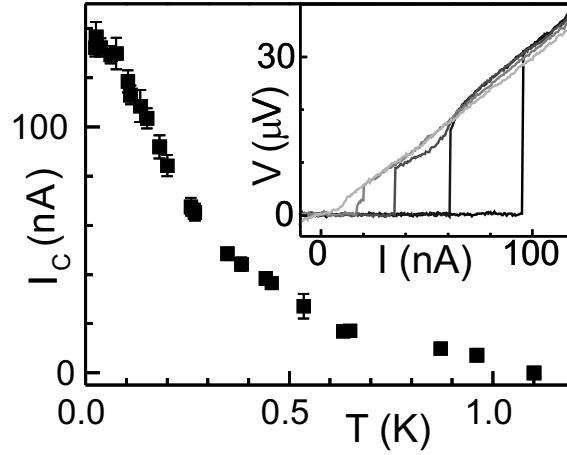


**Figure 6.5:** Temperature dependence of the critical current,  $I_C(T)$ , for device n.1. For every data point (solid circles),  $I_C$  is determined through a statistical average of 2000 reiterated measurements at a repetition frequency of 40 Hz. Representative  $V(I)$  measurements are shown in the inset of Fig. 6.5 for different temperatures  $T = 60$  (black), 200, 380, 630, 960 mK (light gray). In each measurement, the bias current is ramped and the switching current is recorded (the switching event from supercurrent to quasi-particle branch is determined by the appearance of a source-drain voltage above a threshold value of  $8\mu V$ ). The error bar on  $I_C$  corresponds to the standard deviation. Notably,  $I_C$  remains finite up to  $T \approx T_C$ .



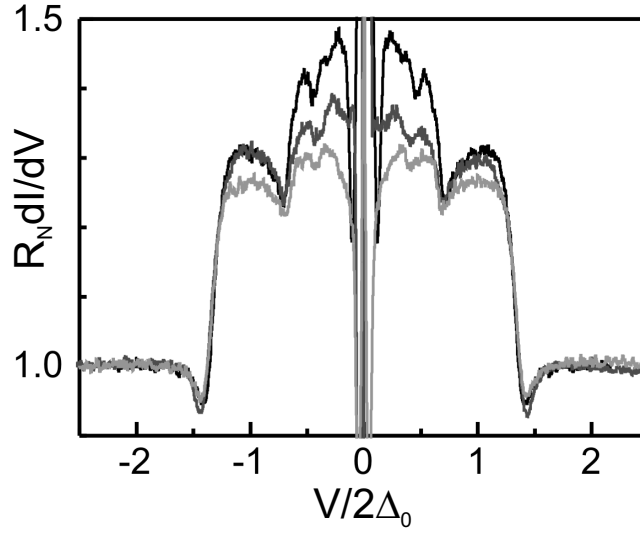


**Figure 6.6:** Differential conductance,  $dI/dV$ , as a function of bias voltage,  $V$ , measured for three different devices: n.1 (dark gray), n.3 (black), and n.4 (light gray).  $dI/dV$  is normalized to the corresponding normal-state value,  $R_N^{-1}$ . The three measurements exhibit a comparable enhancement in the  $dI/dV$  for  $V < 2\Delta_0$  which denotes a reproducibly high transparency of the  $S$ - $N$  interfaces. Sub-gap structures due to multiple Andreev reflection are also observed. Their position is determined by the value of the superconducting energy gap, which is approximately the same for all devices.

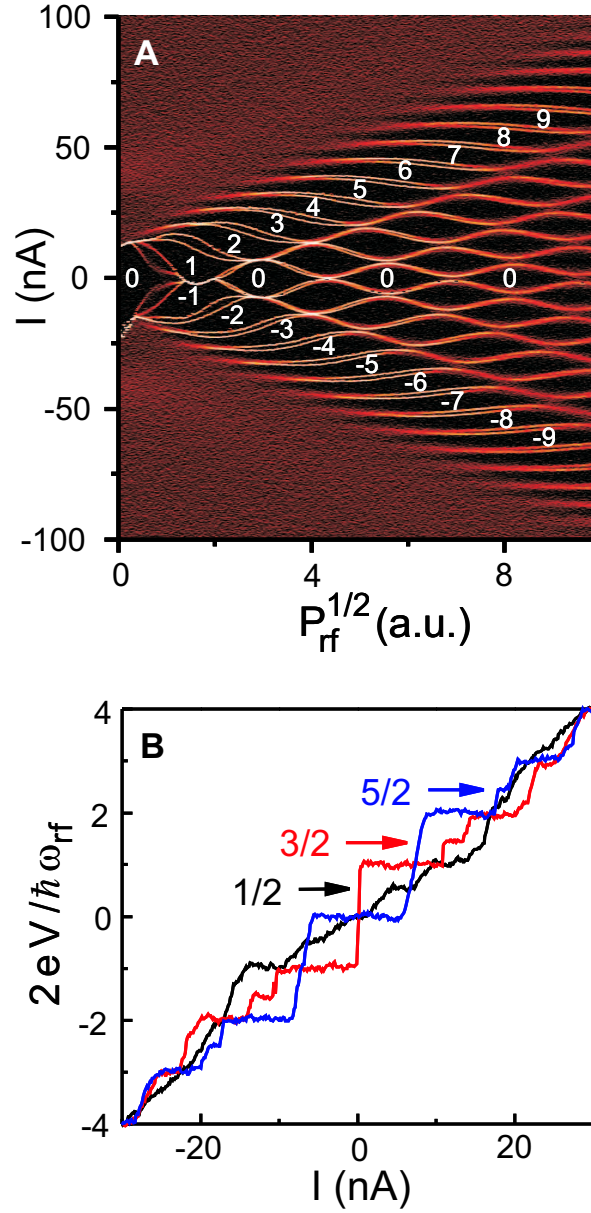


**Figure 6.7:** (A) Color-scale plot of  $dV/dI$  versus bias current,  $I$ , and the square root of the applied microwave power,  $P_{rf}^{1/2}$ , at 2 GHz and for device n. 3 (the same device to which Fig. 6.2 is referred in the main text). With respect to Fig. 6.2B, this measurement differs only for the value of the microwave frequency. The wide regions in black ( $dV/dI = 0$ ) correspond to the Shapiro steps and are labeled by an integer  $n$  such that  $V_n = n\hbar\omega_{rf}/2e$ . The narrow black regions between consecutive Shapiro steps correspond to the presence of half-integer steps (i.e.  $n = 1/2, 3/2, 5/2, \dots$ ). (B) Selected  $V(I)$  traces which clearly show the half-integer steps. Similar half-integer steps have previously been reported for other S-N-S systems and they were interpreted as a consequence of a non-sinusoidal current-phase Josephson relation [4]. In our experiments, half-integer steps appear only for microwave frequencies below 3 GHz.

# Chapter 7

## Quantum supercurrent transistors in carbon nanotubes

P. Jarillo-Herrero, J. A. van Dam, & L. P. Kouwenhoven

Electronic transport through nanostructures is greatly affected by the presence of superconducting leads [1, 2, 3]. If the interface between the nanostructure and the superconductors is sufficiently transparent, a dissipationless current (supercurrent) can flow through the device due to the Josephson effect [4, 5]. A Josephson coupling, as measured via the zero-resistance supercurrent, has been obtained via tunnel barriers, superconducting constrictions, normal metals, and semiconductors. The coupling mechanisms vary from tunneling to Andreev reflection [6, 7, 8, 5]. The latter process has always occurred via a normal-type system with a continuous density of states. Here we investigate a supercurrent flowing via a discrete density of states, i.e., the quantized single particle energy states of a quantum dot [9], or artificial atom, placed in between superconducting electrodes. For this purpose, we exploit the quantum properties of finite-sized carbon nanotubes [10] (CNTs). By means of a gate electrode, successive discrete energy states are tuned ON and OFF resonance with the Fermi energy in the superconducting leads, resulting in a periodic modulation of the critical current and a non-trivial correlation between the conductance in the normal state and the supercurrent. We find, in good agreement with existing theory [11], that the product of the critical current and the normal state resistance becomes an oscillating function, in contrast to being constant as in previously explored regimes.

---

This chapter has been published in Nature.

## 7.1 Introduction

In artificial atoms current can flow via discrete states according to the general process of resonant tunneling, i.e., resonant when the Fermi energy in the leads is aligned with discrete energy states [9]. The maximum conductance,  $G$ , through a single spin-degenerate energy level depends on the coupling to the leads. For the case of phase-coherent tunneling,  $G$  can reach  $2e^2/h$ , when charging effects are unimportant. If charging effects are significant, still  $G = 2e^2/h$  can be achieved (even off-resonance) by means of the Kondo effect [12], which establishes spin coherence between the quantum dot (QD) and the leads. An entirely new situation arises in the case of superconducting leads, i.e., when two superconductors are coupled via a discrete single particle state. As we show below, the conductance can reach infinity, that is, a supercurrent can flow through the QD. So, far beyond the perfect conductance level of  $2e^2/h$  occurring when the transmission probability reaches one. This zero resistance state is peculiar since just a single discrete state, that can be occupied only with two spin degenerate electrons simultaneously, is available for coupling the collective macroscopic states in the leads. In contrast to previously accessible regimes, we can study Josephson coupling for ON and OFF resonant tunneling, which enables a transistor-like control of the supercurrent through the quantum dot.

The carbon nanotube devices are fabricated by means of standard nanofabrication techniques and geometries (e-beam lithography to define customized electrodes on CNTs grown by chemical vapour deposition on top of oxidized silicon substrates [13] with two extra important ingredients: the choice of superconducting material and a multiple-stage filtering system to suppress electronic noise over a wide frequency range (see Fig. 7.1a and appendix for details).

## 7.2 Quantum supercurrent transistor action

The quantum behaviour of electrons in carbon nanotubes in good contact with metallic electrodes emerges clearly in a measurement of the differential resistance,  $dV/dI$ , versus measured source-drain voltage,  $V$  and gate voltage,  $V_G$ , as shown in Fig. 7.1b for one of our devices in the normal state. The differential resistance exhibits a pattern of high and low conductance regions, typical of nanotube devices well coupled to the leads [14, 15], with a characteristic voltage scale,  $V \sim 3.5$  mV. This energy corresponds to the energy level separation between the discrete electronic states due to the finite length of the CNT,  $\Delta E = \hbar v_F/2L$ , where  $\hbar$  is Planck's constant,  $v_F = 8.1 \cdot 10^5$  m/s is the Fermi velocity in the CNT, and  $L$  its length. The value obtained from this measurement,  $L \sim 480$  nm,

is in good agreement with the length of the nanotube segment in between the metallic electrodes, 470 nm. When the sample is cooled down below the superconducting critical temperature of the electrodes ( $\sim 1.3\text{K}$ ), the electronic transport through the nanotube is strongly affected due to the superconducting proximity effect [1, 16, 17, 18, 19], which can be viewed as the leakage of Cooper pairs from a superconductor into a normal metal-type material. This proximity effect is evident from the observation of multiple Andreev reflections (MAR) [20] and the flow of a supercurrent through the device (Figs. 7.1c,d). We note that we have observed similar supercurrents in 4 out of 7 measured metallic CNT devices with room temperature resistances below  $35\text{k}\Omega$  (see appendix for additional data and magnetic field dependence). The most interesting feature of this supercurrent is that its maximum value (critical current,  $I_C$ ) can be strongly modulated by means of a gate electrode [21], as shown in Fig. 7.1d. Since the CNTs are metallic, this means that the supercurrent transistor action must have a different mechanism than in conventional semiconductor structures. It is also remarkable that the gate voltage necessary to change from maximum to minimum  $I_C$  is of only  $\sim 50\text{ mV}$ , much smaller than the typical gate voltages necessary to significantly vary the charge density of semiconducting carbon nanotubes [22] or nanowires with similar geometries [23].

In order to establish the origin of the modulation of  $I_C$ , it is important to characterize the sample over a larger gate voltage range. A measurement of  $dV/dI(I, V_G)$  (Fig. 7.2b) shows a non-monotonic, quasi-periodic set of low differential resistance regions, where  $I_C$  is largest, in between regions of high  $dV/dI$ , where  $I_C$  is strongly suppressed (Fig. 7.2a). This pattern follows closely the low-bias pattern of Fig. 7.1b, but now the vertical axis is current, instead of voltage. The correspondence between the two patterns indicates that the modulation of  $I_C$  is due to the tuning ON and OFF resonance with gate voltage of the energy levels in the CNT with respect to the Fermi energy in the leads (as shown schematically in Fig. 7.2e). Such Josephson transistor mechanism, purely due to the discrete nature of the energy levels in a nanostructure (in this case finite-sized CNTs), has not been previously observed.

Before turning to a more quantitative description, we note that the modulation of  $I_C$  is followed by a series of  $dV/dI$  peaks and dips moving up and down in the current axis. These are better seen in the high-resolution measurement shown in Fig. 7.2c and reflect the multiple Andreev reflection processes (see also Fig. 7.1c) taking place at the CNT-metal interfaces. MAR processes occur at voltages  $V = 2\Delta_g/en$  ( $\Delta_g$  is the superconducting energy gap,  $e$  is the electron charge,  $n$  an integer number). The  $dV/dI$  curves in fact occur at constant voltage in this current-biased sample (see appendix). Two individual  $dV/dI$  traces

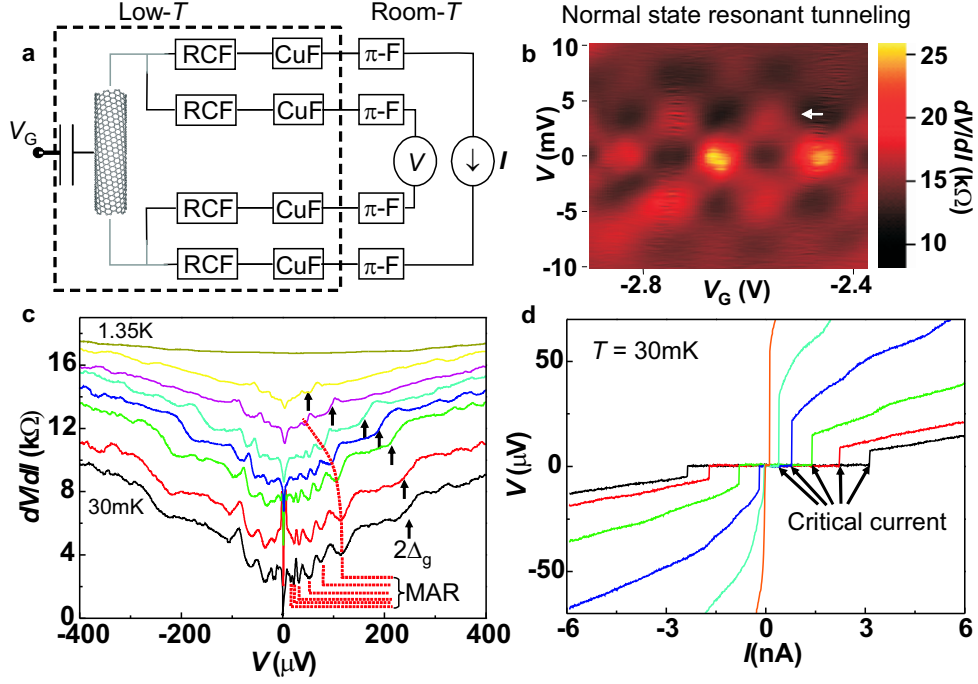


**Figure 7.1:** Measurement scheme and basic sample characterization. **a**, Diagram showing the measurement circuit. Grey represents Ti/Al electrodes (10nm/60nm). Titanium ensures a good electrical contact to the CNT, while aluminium becomes superconducting below  $\sim 1.3\text{K}$ , well above the base temperature of our dilution refrigerator. The CNTs are probed in a four-terminal geometry (current bias, voltage measurement). An important element is the incorporation of three sets of filters for each measurement wire: a copper-powder filter (Cu-F) for high frequency noise,  $\pi$ -filters for intermediate frequencies and a two-stage RC filter to suppress voltage fluctuations at low frequencies. The dashed box region indicates the low temperature part of the circuit. The rest is at room temperature. **b**, Color-scale plot of the differential resistance,  $dV/dI$ , versus measured voltage,  $V$ , and gate voltage,  $V_G$  at  $T = 4.2 \text{ K}$ . The white arrow indicates the energy separation between discrete quantum levels in the CNT. **c**, Differential resistance versus measured source-drain voltage,  $V$ , at different temperatures (0.030, 0.47, 0.7, 0.88, 1.02, 1.18, 1.22 and 1.35 K, from bottom to top). The curves are offset for clarity (by  $2\text{k}\Omega$ , for 0.47 and 0.7 K, and by  $1\text{k}\Omega$  for the rest). The features present in all curves below 1.3 K are due to the induced superconducting proximity effect. The arrows indicate the superconducting gap at  $V = 2\Delta_g/e \sim 250\mu\text{V}$ . The dotted lines indicate multiple Andreev reflection (MAR) processes, which manifest as dips in  $dV/dI$ . **d**,  $V(I)$ -characteristics at base temperature showing the modulation of the critical current,  $I_C$ , with  $V_G$  ( $V_G = -2.59, -2.578, -2.57, -2.563, -2.555$  and  $-2.541 \text{ V}$  from black to orange). For currents larger than  $I_C$  the system goes into a resistive state (abrupt jump from zero to finite  $V$ ).

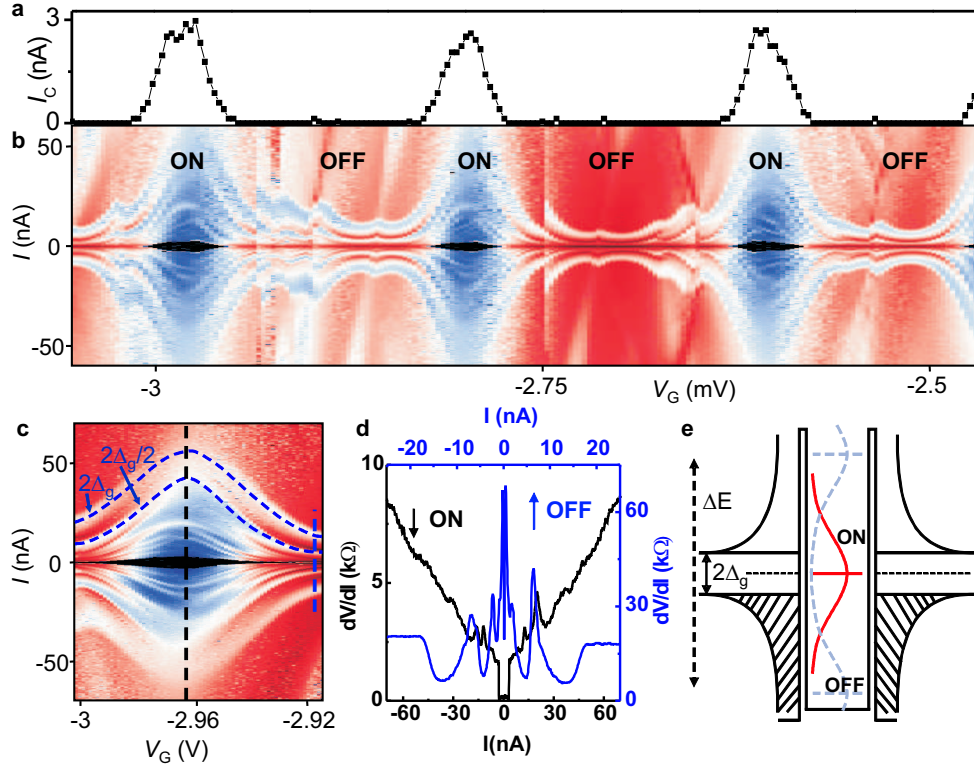


**Figure 7.2:** Quantum supercurrent transistor. **a**, Variation of the critical current,  $I_C$ , with gate voltage,  $V_G$ , extracted from **b** (see **c** and Fig. 7.3a for high resolution).  $I_C$  is measured as the upper half-width of the black region around  $I = 0$ . **b**, Color-scale representation (in log scale) of  $dV/dI(I, V_G)$  at  $T = 30$  mK (black is zero, i.e. supercurrent region, and  $dV/dI$  increases from dark blue to white and red; the scale can be inferred from **d**). Both  $dV/dI$  and  $I_C$  exhibit a series of quasiperiodic modulations with  $V_G$  as the energy levels in the CNT QD are tuned ON and OFF resonance with respect to the Fermi energy in the superconducting leads. The sharp vertical features are caused by random charge switches and shift the diagram horizontally. The narrow tilted features present in the OFF regions (for example at  $V_G \sim -2.87$  V) occur reproducibly and are associated with Fano resonances [29] (see appendix). **c**, High-resolution  $dV/dI(I, V_G)$  plot of the left-most resonance region in **b**. The modulation of  $I_C$  (black central region) as well as multiple Andreev reflection (up to several orders, the first two are highlighted by the dashed blue lines) are clearly visible. **d**, Two representative  $dV/dI(I)$  curves, taken from **c** at the vertical black and blue dashed lines, illustrating the different behaviour of the differential resistance in the ON (black curve/axis) and OFF (blue curve/axis) resonance case. **e**, Schematic diagram showing a strongly coupled QD in between two superconducting leads. The gate voltage tunes the position of the Lorentzian level from the ON (red curve) to the OFF (grey dashed curve) state.

are shown in Fig. 7.2d for the ON and OFF resonance situations. In both cases  $dV/dI$  exhibits oscillations due to MAR, but the overall behaviour of  $dV/dI$  is very different. In the ON resonance case,  $dV/dI$  decreases with decreasing  $|I|$  (on average) until it “switches” to zero when  $\sim I_C$  is reached. For the OFF case,  $dV/dI$  increases with decreasing  $|I|$  (except at the MAR points), until  $|I|$  reaches a very strongly suppressed value of  $I_C$  (barely visible in Fig. 7.2d, see Fig. 7.3). From the normal state resistance values in the ON and OFF resonant cases, we can conclude that the  $dV/dI$  changes between these qualitative behaviours at values of  $dV/dI \sim h/(2e^2) \sim 13 \text{ k}\Omega$ , i.e., once the resistance per channel of the CNT becomes of the order of the quantum of resistance (see also appendix).

### 7.3 Correlation between critical current and normal state conductance

The correlation between the critical current and the normal state resistance,  $R_N$ , is well studied in S - “normal metal” - S (SNS) structures. As a matter of fact, for short junctions in diffusive systems and ideal NS interfaces,  $I_C R_N \sim \Delta_g/e$ , i.e. constant [5]. The situation differs when one considers a single discrete energy level. In this case, the conductance is given by  $G_N = (4e^2/h)T_{BW}$ , where  $T_{BW} = \Gamma_1\Gamma_2/((\epsilon_R/h)^2 + 0.25\Gamma^2)$  is the Breit-Wigner transmission probability,  $\Gamma_{1,2}$  are the tunnel rates through the left/right barriers ( $\Gamma = \Gamma_1 + \Gamma_2$ ), and  $\epsilon_R$  is the energy of the resonant level relative to the Fermi energy in the leads. (Note that we have added a factor of 4 in  $G_N$  to account for the spin and orbital degeneracy of the CNT electronic states [10, 24, 15, 25].) Beenakker and van Houten [11] have studied the lineshape for the critical current in such a system. For the case of a wide resonance,  $h\Gamma \gg \Delta_g$ , they obtained  $I_C = I_0[1 - (1 - T_{BW})^{1/2}]$ , with  $I_0 = 2e\Delta_g/h$ . Experimentally, we can vary the position of the resonant level by means of a gate voltage,  $\epsilon_R \propto V_G$ , as shown for the normal state conductance in Fig. 7.3b. From the maximum value of  $G_N \sim 3.8e^2/h$ , we deduce a barrier asymmetry  $\Gamma_1/\Gamma_2 \sim 0.64$ . We use this to fit  $I_C(V_G)$  and  $G_N(V_G)$  (see Figs. 7.3a,b; red curves). Although the functional form is in good agreement with theory, the values for  $\Gamma$ ,  $\Gamma_I = 0.85 \text{ meV}/h$  and  $\Gamma_G = 1.36 \text{ meV}/h$ , obtained from the  $I_C(V_G)$  and  $G_N(V_G)$  fits, respectively, differ substantially. Also the value of  $I_0$  that we measure, 4.15 nA, is much smaller than the theoretical value ( $2e\Delta_g/h \sim 60 \text{ nA}$ ). Such low critical currents are reminiscent of the behaviour of small, underdamped, current-biased Josephson junctions [26], where the electromagnetic environment leads to a measured critical current,  $I_{CM}$ , much lower than the true critical current  $I_C$ . The dynamics of such a Josephson junction can be visualized as that of



a particle moving in the so-called “tilted washboard” potential [5], where the driving current corresponds to the tilt in the potential. For the case of low dissipation (underdamped junctions), a small fluctuation can cause the particle to slide down the potential and go into a “runaway” state. This occurs at a value of  $I$  much smaller than the true  $I_C$ , and it has been shown [26] that the measured critical current scales as  $I_{CM} \propto (I_C)^{3/2}$ . In order to test the applicability of this model to CNT Josephson junctions, we have fitted  $I_{CM} = I_{0M}[1 - (1 - T_{BW}(V_G, \Gamma)^{1/2})^{3/2}]$ , as shown by the blue curve in Fig. 7.3a. We obtain a similarly low value of  $I_{0M} = 4.57$  nA and this time, the value of  $\hbar\Gamma_I$  obtained, 1.22 meV, is in good agreement with  $\hbar\Gamma_G = 1.36$  meV, resulting also in an improved fit to the data.

The importance of the coupling to the environment manifests itself more explicitly when examining the correlation between the critical current and the normal state conductance. We note that in the case of an ideal diffusive SNS junction the correlation would yield a simple straight line. The experimental data severely deviate from such curve (Fig. 7.3c). First we consider the expected theoretical decay for the case of a discrete state (red curve)  $I_C = I_0[1 - (1 - 0.25G_N)^{1/2}]$  (no fitting parameters), with the value of  $I_0$  obtained from Fig. 7.3a, and  $G_N$  measured in units of  $e^2/h$ . The comparison with the predicted theoretical line shows that the measured  $I_C$  is significantly lower than expected. However, a remarkably better agreement is found when the electromagnetic environment is included, as shown by the blue curve,  $I_{CM} = I_0[1 - (1 - 0.25G_N)^{1/2}]^{3/2}$ , indicating the generality of the  $(I_C)^{3/2}$  dependence of  $I_{CM}$  for very different type of Josephson junctions [26].

The predicted lineshape of  $I_C$  (even in the presence of low dissipation) implies that the  $I_C R_N$  product is not constant, but instead has a maximum on resonance. We plot in Fig. 7.3d the  $I_C R_N$  product, which indeed exhibits a peak structure. The red and blue lines, which contain no extra fitting parameters, result from dividing the theoretical curves in Fig. 7.3a by the curve in Fig. 7.3b, and further substantiate the results from earlier figures.

We emphasize that the above-mentioned analysis confirms the correct order of the relevant energy scales necessary for the observation of the resonant tunneling supercurrent transistor action [11]:  $\Delta E$  ( $\sim 3.5$  meV)  $> \hbar\Gamma$  ( $\sim 1.3$  meV)  $\gg \Delta_g$  ( $\sim 125$   $\mu$ eV)  $> U$ . The last inequality is justified since signatures of Coulomb blockade effects are absent in our data, concluding that the charging energy,  $U$ , is negligible.

We end by noting that, although both superconductivity and the Kondo effect are collective many-body phenomena, their effect on resonant tunneling is very different [18]. The Kondo enhancement occurs OFF-resonance, while the su-

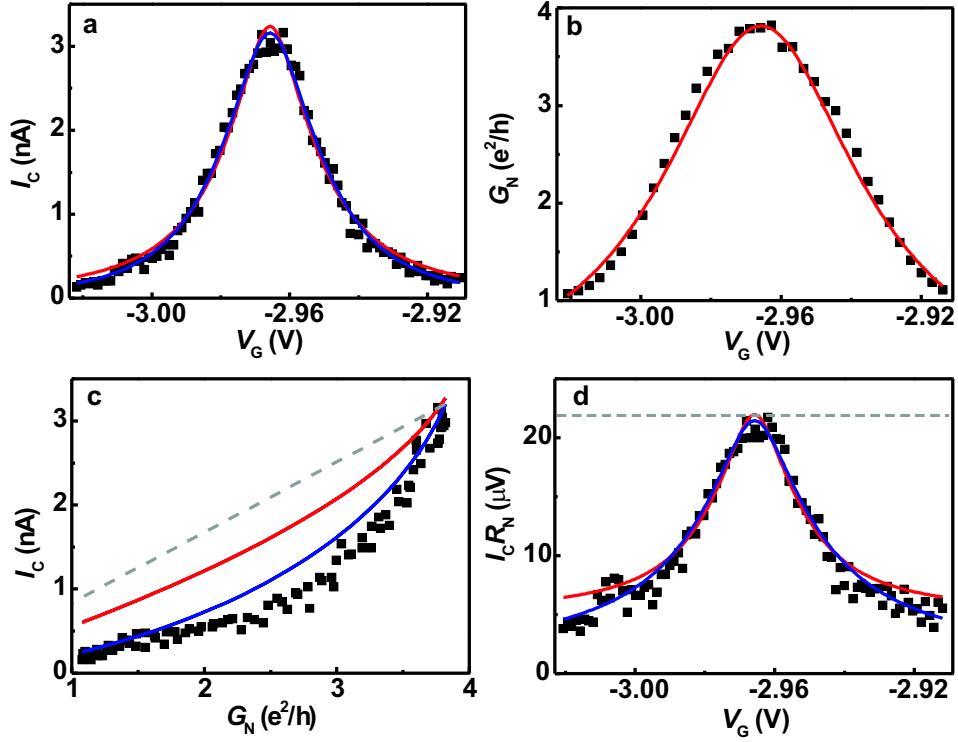


**Figure 7.3:** Correlation between critical current and normal state conductance and modulation of the  $I_C R_N$  product. In all panels, the black dots represent the experimental data points ( $T = 30$  mK) and the red/blue curves are theoretical plots. **a**, Critical current,  $I_C$ , versus  $V_G$  for the resonance shown in Fig. 2c. The theoretical lines are fits to  $I_C = I_0[1 - (1 - \Gamma_1\Gamma_2/((V_G - V_{GR})^2 + 0.25\Gamma^2))^{1/2}]$  (red curve) and  $I_{CM} = I_{0M}[1 - (1 - \Gamma_1\Gamma_2/((V_G - V_{GR})^2 + 0.25\Gamma^2))^{1/2}]^{3/2}$  (blue), as explained in the main text.  $V_{GR}$  is the value of gate voltage on resonance. All gate voltages and  $\Gamma$ 's are converted into energies by multiplying by the gate coupling factor,  $\alpha = 0.02$  meV/mV, obtained from measurements in the non-linear regime. **b**, Conductance,  $G_N$ , as a function of  $V_G$  in the normal state ( $B = 40$  mT) and the corresponding fit to  $G_N = 4e^2/h\Gamma_1\Gamma_2/((V_G - V_{GR})^2 + 0.25\Gamma^2)$ . **c**,  $I_C - G_N$  correlation plot. The data show a non-trivial correlation, with a stronger decrease of  $I_C$  than expected from the theoretical curve  $I_C = I_0[1 - (1 - 0.25G_N)^{1/2}]$  (red curve). The 0.25 factor simply denotes that  $G_N$  is measured in  $e^2/h$  units. The difference can be almost entirely accounted for by the influence of the electromagnetic environment, resulting in a measured  $I_{CM} = I_0[1 - (1 - 0.25G_N)^{1/2}]^{3/2}$  (blue curve). An ideal SNS junction, with N a normal metal with continuous density of states, would exhibit a linear  $I_C - G_N$  correlation curve (grey dashed curve). **d**,  $I_C R_N$  product versus  $V_G$ , resulting from dividing the experimental data and theory curves from **a** and **b**. The grey dashed line indicates a constant  $I_C R_N$  product such as in a SNS junction.

perconducting zero-resistance state, as we have shown, is most pronounced ON-resonance. In fact, we expect that the study of CNT devices with intermediate transmission, and thus, larger Coulomb interactions, will enable the observation of Kondo-enhanced supercurrents in the OFF resonant case [27, 28].

We thank Yu.V. Nazarov, C.W.J. Beenakker, W. Belzig, S. De Franceschi and Y-J. Doh for discussions and C. Dekker for the use of CNT growth facilities. Financial support obtained from the Japanese International Cooperative Research Project (ICORP) and the Dutch Fundamenteel Onderzoek der Materie (FOM).

## References

- [1] de Gennes, P. G. Boundary Effects in Superconductors. *Rev. Mod. Phys.* **36**, 225-237 (1964).
- [2] Ralph, D. C., Black, C. T. & Tinkham, M. Spectroscopic Measurements of Discrete Electronic States in Single Metal Particles. *Phys. Rev. Lett.* **74**, 3241-3244 (1995).
- [3] von Delft, J. & Ralph, D. C. Spectroscopy of discrete energy levels in ultra-small metallic grains. *Phys. Rep.* **345**, 62-173 (2001).
- [4] Josephson, B. D. Possible New Effects in Superconductive Tunnelling. *Phys. Lett.* **1**, 251-253 (1962).
- [5] Tinkham, M. *Introduction to Superconductivity* (McGraw-Hill, Singapore, 1996).
- [6] Andreev, A. F. The Thermal Conductivity of the Intermediate State in Superconductors. *Sov. Phys. JETP* **19**, 1228-1231 (1964).
- [7] Likharev, K. K. Superconducting Weak Links. *Rev. Mod. Phys.* **51**, 101-159 (1979).
- [8] Blonder, G. E., Tinkham, M. & Klapwijk, T. M. Transition from Metallic to Tunneling Regimes in Superconducting Micro-Constrictions - Excess Current, Charge Imbalance, and Super-Current Conversion. *Phys. Rev. B* **25**, 4515-4532 (1982).
- [9] Sohn, L. L., Kouwenhoven, L. P., & Schön, G. (eds). *Mesoscopic Electron Transport* (Kluwer, Dordrecht, 1997).
- [10] Dresselhaus, M. S., Dresselhaus, G. & Eklund, P. C. *Science of Fullerenes and Carbon Nanotubes* (Academic Press, San Diego, 1996).

- [11] Beenakker, C. W. J. & van Houten, H. Single-Electron tunneling and mesoscopic devices (ed. Koch, H., Lübbig, H) (Springer, Berlin, 1992). (see also e-Print available at <http://xxx.lanl.gov/abs/cond-mat/0111505>).
- [12] Kouwenhoven, L. & Glazman, L. Revival of the Kondo effect. *Phys. World* **14**, 33-38 (2001).
- [13] Jarillo-Herrero, P. *et al.* Orbital Kondo effect in carbon nanotubes. *Nature* (London) **434**, 484-488 (2005).
- [14] Liang, W. J. *et al.* Fabry-Perot interference in a nanotube electron waveguide. *Nature* (London) **411**, 665-669 (2001).
- [15] Buitelaar, M. R., Bachtold, A., Nussbaumer, T., Iqbal, M. & Schönenberger, C. Multiwall carbon nanotubes as quantum dots. *Phys. Rev. Lett.* **88**, 156801 (2002).
- [16] Kasumov, A. Y. *et al.* Supercurrents through single-walled carbon nanotubes. *Science* **284**, 1508-1511 (1999).
- [17] Morpurgo, A. F., Kong, J., Marcus, C. M. & Dai, H. Gate-Controlled Superconducting Proximity Effect in Carbon Nanotubes. *Science* **286**, 263-265 (1999).
- [18] Buitelaar, M. R., Nussbaumer, T. & Schönenberger, C. Quantum dot in the Kondo regime coupled to superconductors. *Phys. Rev. Lett.* **89**, 256801 (2002).
- [19] Haruyama, J. *et al.* End-bonding multiwalled carbon nanotubes in alumina templates: Superconducting proximity effect. *Appl. Phys. Lett.* **84**, 4714-4716 (2004).
- [20] Buitelaar, M. R. *et al.* Multiple Andreev reflections in a carbon nanotube quantum dot. *Phys. Rev. Lett.* **91**, 057005 (2003).
- [21] Takayanagi, H. & Kawakami, T. Superconducting Proximity Effect in the Native Inversion Layer on InAs. *Phys. Rev. Lett.* **54**, 2449-2452 (1985).
- [22] McEuen, P. L. Single-wall carbon nanotubes. *Phys. World* **13**, 31-36 (2000).
- [23] Doh, Y. J. *et al.* Tunable supercurrent through semiconductor nanowires. *Science* **309**, 272-275 (2005).
- [24] Liang, W. J., Bockrath, M. & Park, H. Shell filling and exchange coupling in metallic single-walled carbon nanotubes. *Phys. Rev. Lett.* **88**, 126801 (2002).
- [25] Sapmaz, S. *et al.* Electronic excitation spectrum of metallic carbon nanotubes. *Phys. Rev. B* **71**, 153402 (2005).

- [26] Joyez, P., Lafarge, P., Filipe, A., Esteve, D. & Devoret, M. H. Observation of Parity-Induced Suppression of Josephson Tunneling in the Superconducting Single-Electron Transistor. *Phys. Rev. Lett.* **72**, 2458-2461 (1994).
- [27] Glazman, L. I. & Matveev, K. A. Resonant Josephson Current through Kondo Impurities in a Tunnel Barrier. *JETP Lett.* **49**, 659-662 (1989).
- [28] Choi, M. S., Lee, M., Kang, K., & Belzig, W. Kondo effect and Josephson current through a quantum dot between two superconductors. *Phys. Rev. B* **70**, 020502 (2004).
- [29] Babic, B. & Schönenberger, C. Observation of Fano resonances in single-wall carbon nanotubes. *Phys. Rev. B* **70**, 195408 (2004).
- [30] Zhang, Z., Dikin, D. A., Ruoff, R. S. & Chandrasekhar, V. Conduction in carbon nanotubes through metastable resonant states. *Europhys. Lett.* **68**, 713-719 (2004).
- [31] Fano, U. Effects of Configuration Interaction on Intensities and Phase Shifts. *Phys. Rev.* **124**, 1866-1878 (1961).
- [32] Kong, J., Soh, H. T., Cassell, A. M., Quate, C. F. & Dai, H. J. Synthesis of individual single-walled carbon nanotubes on patterned silicon wafers. *Nature* **395**, 878-881 (1998).
- [33] Li, Y. M. et al. Growth of single-walled carbon nanotubes from discrete catalytic nanoparticles of various sizes. *J. Phys. Chem. B* **105**, 11424-11431 (2001).
- [34] Cheung, C. L., Kurtz, A., Park, H. & Lieber, C. M. Diameter-controlled synthesis of carbon nanotubes. *J. Phys. Chem. B* **106**, 2429-2433 (2002).
- [35] Johansson, G., Bratus, E. N., Shumeiko, V. S. & Wendin, G. Resonant multiple Andreev reflections in mesoscopic superconducting junctions. *Phys. Rev. B* **60**, 1382-1393 (1999).

## 7.4 Appendix

This appendix contains some additional discussion and data, and has been submitted as Supplementary Information to the main text.

### *Filtering system*

A filtering system is necessary to prevent electronic noise from reaching the sample (as much as possible) since this suppresses the critical current. As mentioned in the main text we use three filters in series: a copper-powder filter (CuF), a

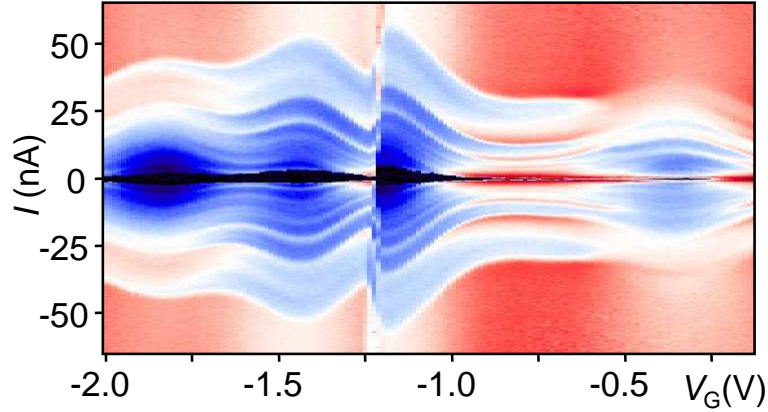


**Figure 7.4:** Differential resistance versus  $V$  and  $V_G$  for a different device. Black means zero and  $dI/dV$  increases from blue to red.

$\pi$ -filter and a two-stage RC filter (RCF). Three filters are used in order to cover the entire spectrum, from low frequency up to the microwave regime. CuFs are widely used in dilution refrigerator measuring setups. They are typically used to suppress the high frequency noise ( $f \geq 1$  GHz), lowering the effective electron temperature. Our CuFs consist of  $\sim 1.5$  m long manganine wires, and give an attenuation  $\geq 50$  dB at 1 GHz. The  $\pi$ -filters cover the intermediate frequency range ( $\sim 10$  MHz - 2 GHz). The two-stage RC filters are useful in the range few kHz - 100 MHz and are widely used to measure small critical currents. The advantage of a two-stage versus a single stage RC filter is that it provides an attenuation of 40 dB per decade (instead of 20 dB/decade) above a certain cut-off frequency. An example of a used configuration is:  $R_1 = 820 \Omega$ ,  $R_2 = 1.2$  k $\Omega$ ;  $C_1 = 20$  nF,  $C_2 = 4.7$  nF, which gives a cut-off frequency in the  $\sim 10$  kHz range.

### ***Additional data & Fano resonances***

Here we show additional data from a different device. Figure 7.4 shows a  $dV/dI$  versus  $(I, V_G)$  plot, similar to Fig. 7.2b. Both multiple Andreev reflection and a modulation of the critical current as a function of gate voltage are clearly visible.

In the center of the figure a sharp resonance can be seen, similar also to the sharp resonances in Fig. 7.2b. Such resonances have been observed and discussed in the context of carbon nanotubes strongly coupled to the leads [30, 29] and attributed to Fano resonances [31], although their origin have not been fully established. Two interfering channels are needed for Fano resonances to occur, a strongly coupled one and a weakly coupled one. The weakly coupled one can be

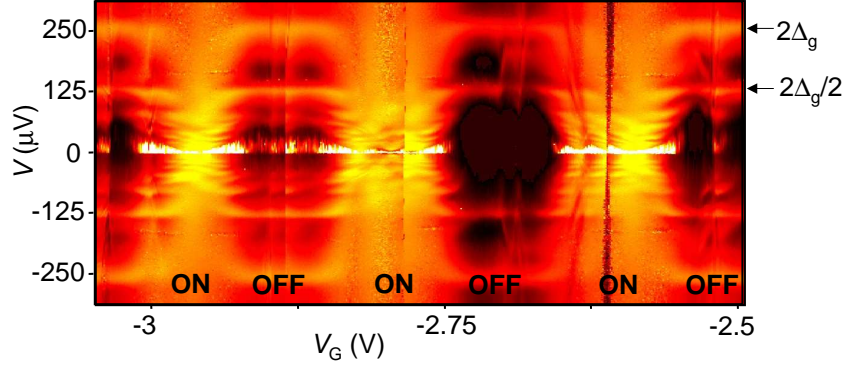


**Figure 7.5:** Differential conductance versus  $V$  and  $V_G$  for the data shown in 7.2b. The horizontal features at  $2\Delta_g$  and  $2\Delta_g/2$  are due to MAR.

an impurity, an inner shell in a multiwall tube or a weakly coupled tube in a thin rope. It has also been suggested that intrinsic resonances may arise for individual single wall tubes [29], due to an asymmetric coupling of the two orbital channels in carbon nanotubes. We have examined the diameters of our samples and they are in the 2 to 7 nm range. While single wall nanotubes of 2-3 nm are usually obtained with our CVD growth method [32], a diameter like 7 nm is more rare. We note however that single wall NTs grown by CVD up to 13 nm in diameter have been reported [33, 34]. Therefore it cannot entirely be excluded that the Fano resonances are due to the fact that those tubes measured are not individual single wall tubes.

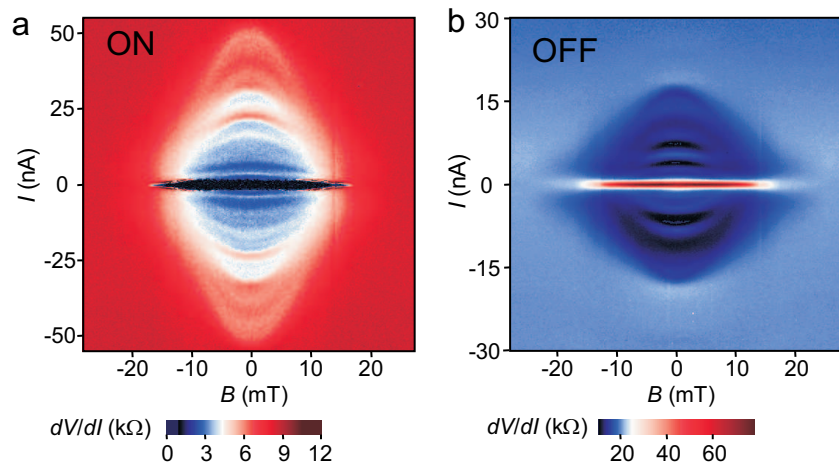


**Figure 7.6:** Differential resistance versus  $I$  and  $B$  showing the suppression of the proximity effect for the ON (a) and OFF (b) resonance case.

Nevertheless, the conductance of our devices in the normal state gets very close to, but doesn't exceed,  $4e^2/h$ , similar to Ref. [29]. Future studies are necessary to clarify the precise origin of the Fano resonances.

### ***Multiple Andreev Reflection***

In order to visualize the regions of supercurrent flow, figure 7.2 shows differential resistance plots as a function of current bias. Because of this, the multiple Andreev reflection (MAR) lines move up and down along the plots (e.g., Fig. 7.2b,c). Figure 7.5 shows the differential conductance,  $dI/dV$  (in log scale), versus measured source-drain voltage and gate voltage (black/dark red is low  $dI/dV$  and yellow is high  $dI/dV$ , the white features at low  $V$  are due to the conversion from current biased to voltage biased near supercurrent). The features in Fig. 7.5 are in good agreement with previous MAR results in carbon nanotubes [20]. For example, the Andreev reflection peaks at  $2\Delta_g$  and  $2\Delta_g/2$  are clearly visible OFF resonance, while they become smeared ON resonance. Also, as predicted theoretically [20, 35], the subgap structure becomes very complex in the vicinity of the resonances.

### ***Magnetic field dependence***

The application of a magnetic field,  $B$ , suppresses superconductivity in the electrodes and, thus, suppresses the proximity effect associated-features in the transport through the nanotube. As an example we show in Figs. 7.6a,b the suppression of MAR and  $I_C$  with  $B$  (shown for the device in Fig. 7.4; other devices exhibit the same behaviour). Figure 7.6a corresponds to the ON resonance case, while fig. 7.6b corresponds to the OFF resonance case. As mentioned in the main text, the differential resistance in the ON-resonance case is lower when the leads are superconducting. On the other hand, in the OFF-resonance case, there is a large 'peak' in  $dV/dI$  at low energies. [Note that the vertical scale is very different for the two figures.] Similar peaks in  $dV/dI$  (although smaller in magnitude) have been observed previously [17] and attributed to electron-electron interactions. While we cannot rule out such effects (for example a small Coulomb interaction effect), it has been shown [20] that a non-interacting model which takes into account only a resonant level in between two superconducting leads, can yield also such an enhancement of the differential resistance at low energies in the OFF-resonance case. A more detailed study, both theoretical and experimental, should shed light on the relative importance of each of the possible effects accounting for these peaks.



## Chapter 8

# Supercurrent reversal in quantum dots

Jorden A. van Dam, Yuli V. Nazarov, Erik P. A. M. Bakkers,  
Silvano De Franceschi, & Leo P. Kouwenhoven

When two superconductors become electrically connected by a weak link a zero-resistance supercurrent can flow [1, 2]. This supercurrent is carried by Cooper pairs of electrons with a combined charge of twice the elementary charge,  $e$ . The  $2e$  charge quantum is clearly visible in the height of Shapiro steps in Josephson junctions under microwave irradiation and in the magnetic flux periodicity of  $h/2e$  in superconducting quantum interference devices [2]. Several different materials have been used to weakly couple superconductors, such as tunnel barriers, normal metals, or semiconductors. Here, we study supercurrents through a quantum dot created in a semiconductor nanowire by local electrostatic gating. Due to strong Coulomb interaction, electrons can only tunnel one-by-one through the discrete energy levels of the quantum dot. This nevertheless can yield a supercurrent when subsequent tunnel events are coherent [3, 4, 5, 6, 7]. These quantum coherent tunnelling processes can result in either a positive or a negative supercurrent, i.e. in a normal or a  $\pi$ -junction [8, 9, 10], respectively. We demonstrate that the supercurrent reverses sign by adding a single electron spin to the quantum dot. When excited states of the quantum dot are involved in transport, the supercurrent sign also depends on the character of the orbital wavefunctions.

---

This chapter has been submitted to Nature.

## 8.1 Introduction

The electronic properties of quantum dots can be probed by attaching a source and drain electrode, allowing charge carriers to tunnel from the dot to both electrodes. If the electrodes are superconducting, transport is strongly affected and largely depends on the transparency of the electrical connection between the electrodes and the quantum dot. A number of experiments have focused on various phenomena in the Coulomb blockade regime but no supercurrents through the quantum dot were observed, mostly due to the lack of a controllable tunnel coupling with the electrodes [11, 12, 13, 14]. Strong coupling and negligible Coulomb interactions were recently obtained in carbon nanotube quantum dots demonstrating resonant tunnelling of Cooper pairs through a single quantum state [15]. In the regime of strong Coulomb interactions the simultaneous occupation of the quantum dot with two electrons is unfavourable. Nevertheless a supercurrent can flow due to the subsequent (but coherent) transport of correlated electrons. This can give rise to a sign change of the Cooper pair singlet (i.e. from  $1/\sqrt{2}(|\uparrow\downarrow\rangle - |\downarrow\uparrow\rangle)$  to  $e^{i\pi}/\sqrt{2}(|\uparrow\downarrow\rangle - |\downarrow\uparrow\rangle)$ ). Therefore, the typical Josephson relation between the supercurrent,  $I_s$ , and the macroscopic phase difference between the superconductors,  $\phi$ , usually given by  $I_s = I_c \cdot \sin(\phi)$ , changes to  $I_s = I_c \cdot \sin(\phi + \pi) = -I_c \cdot \sin(\phi)$  ([5],  $I_c$  is the critical current). Other mechanisms of Cooper pair transport resulting in negative supercurrents have been studied using high- $T_c$  superconductors [8], ferromagnets [9], and non-equilibrium mesoscopic normal metals [10].

## 8.2 Gate controlled SQUIDS

We use indium arsenide (InAs) nanowires as semiconductor weak links [16] in combination with local gate electrodes in order to obtain quantum dots with a tunable coupling to superconducting leads. The mono-crystalline n-type InAs nanowires are grown by a catalytic process based on the vapour-liquid-solid growth method [17, 18, 19, 20]. After growth, the wires are transferred to an oxidized silicon substrate. Previously developed nanofabrication techniques are used to define highly-transparent aluminium-based superconducting contacts [16]. Pairs of nearby nanowires are contacted in parallel forming a superconducting loop with two nanowire junctions (Fig. 8.1a). In a second lithographic step, we define local gate electrodes. One of the nanowires (top nanowire in Fig. 8.1a) is crossed by two gates, labelled  $L$  and  $R$ , in order to define a quantum dot (also see Fig. 8.1b). The bottom nanowire is crossed by one gate, labelled  $REF$ , and will be used as a reference junction with a tunable Josephson coupling. We have

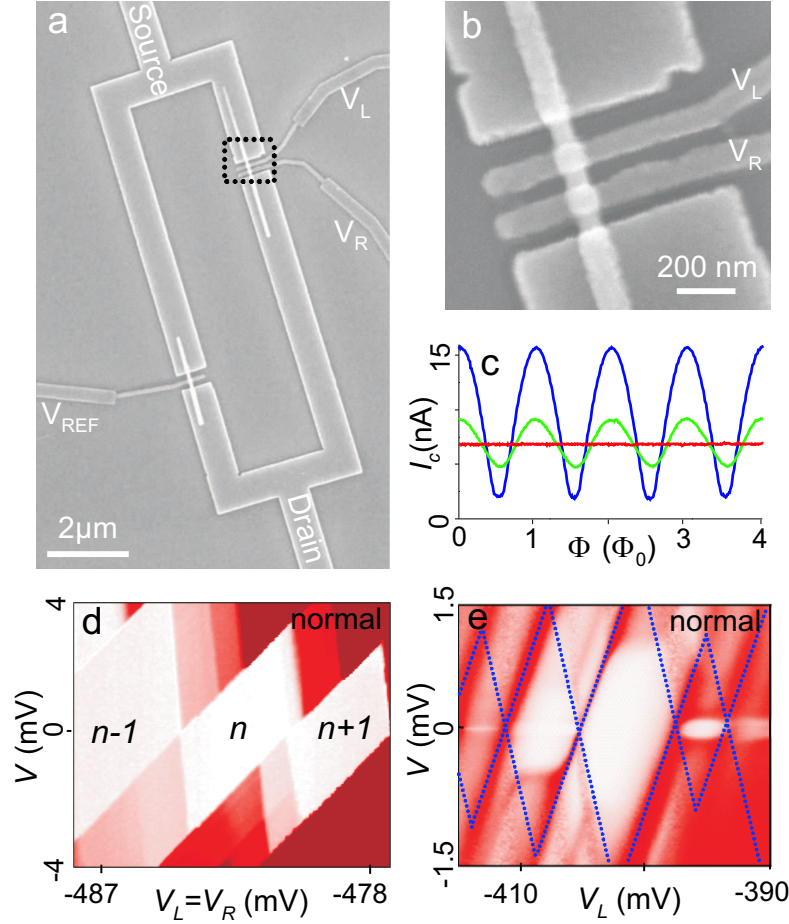


**Figure 8.1:** Sample layout and device characterization. **a**, Scanning electron micrograph of the InAs nanowire SQUID. Two nanowires (diameter  $\sim 60\text{nm}$ ) are incorporated in a superconducting loop (100 nm Al on 10 nm Ti). Aluminium top-gates ( $L$  and  $R$ ) are used to define a quantum dot in the top nanowire. A third gate ( $REF$ ) is used to control the reference junction. **b**, High-resolution image of the top nanowire shown in (a). **c**, Critical current of the SQUID,  $I_c$ , versus magnetic flux,  $\Phi$ , for different voltages applied to the reference gate ( $V_{REF} = 0\text{V}$  (blue),  $-0.64\text{V}$  (green), and  $-0.80\text{V}$  (red)) demonstrating full electrical control over the amplitude of the SQUID oscillations. **d**, Colour plot of absolute current through the dot,  $|I|$ , (increasing from white (0 pA) to red (5 pA)) versus source-drain bias voltage,  $V$ , and  $V_L = V_R$  in the normal state. The Coulomb diamonds are well defined due to the weak tunnel coupling between quantum dot and leads. **e**, Differential conductance,  $dI/dV$ , (increasing from white to red) as a function of  $V$  and  $V_L$  ( $V_R = -0.40\text{V}$ ). The stronger dot-lead coupling results in blurred diamond edges (indicated by dotted lines) and horizontal features inside the diamonds due to inelastic co-tunnelling. Data in (d) and (e) are taken at  $T=30\text{mK}$ , and in a small magnetic field to drive the superconducting contacts into the normal state.

studied two similar devices in detail. Here we present the results for one of them. Similar data from the second device and further details on device fabrication are given in the Appendix.

Below the superconducting transition temperature of the aluminium-based contacts ( $T_c \sim 1.1\text{K}$ ), the two nanowires form superconducting weak links due to the proximity effect [16], thereby realizing a quantum interference device (SQUID) [2]. The critical current of the SQUID,  $I_c$ , as a function of magnetic flux,  $\Phi$ , shows oscillations with a period of  $66\mu\text{T}$ . This is consistent with the addition of a flux quantum,  $\Phi_0 = h/2e$  ( $h$  is Planck's constant,  $e$  the electron charge), to the effective SQUID area of  $30\mu\text{m}^2$  (Fig. 8.1c, blue trace,  $T=30\text{mK}$ ). The maximum (minimum) critical current corresponds to the sum (difference) of the critical currents of the two nanowire junctions. Unlike in other SQUIDs, the critical currents of the individual junctions can be tuned by applying voltages to the respective gates. This is demonstrated by a measurement of the SQUID oscillations for different voltages applied to *REF*. When  $V_{REF}=-0.64\text{V}$  (green trace) the amplitude of the SQUID oscillations is reduced due to the partial local depletion of the nanowire. By further reducing the gate voltage to  $V_{REF}=-0.80\text{V}$ , the reference junction is pinched off resulting in the disappearance of the interference signal. We thus have a unique electrical control over the SQUID operation.

### 8.3 Tunable quantum dots

A quantum dot is formed in the top nanowire by applying negative voltages simultaneously to gates *L* and *R*. The local depletion creates two tunnel barriers which define a quantum dot in the nanowire section between the gates (see inset to Fig. 8.2a) giving rise to discrete energy levels and Coulomb blockade. To show this we pinch off the reference junction ( $V_{REF}=-0.80\text{V}$ ) and apply a small magnetic field in order to suppress superconductivity. Figure 8.1d shows a colour plot of absolute current through the quantum dot,  $|I|$ , as a function of bias voltage,  $V$ , and gate voltages,  $V_L = V_R$ . The sharp diamond edges are due to the weak tunnel coupling between the quantum dot and the source and drain leads. We can increase the coupling by reducing the negative voltages applied to *L* and *R* (see Fig. 8.1e). This results in smoother diamond edges (dotted lines) and the appearance of inelastic co-tunnelling features inside the diamonds. This tunable coupling is particularly important for reaching the narrow transport regime where charging effects dominate but, at the same time, the critical current is large enough to be measurable.

## 8.4 Supercurrent reversal in quantum dots

Switching to the superconducting state but with the reference junction still pinched off, two peaks in  $dI/dV$  develop around  $V \sim \pm 200 \mu\text{V} = \pm 2\Delta^*/e$  (Fig. 8.2b).  $2\Delta^*$  is the superconducting gap induced in the nanowire by the proximity effect (inset Fig. 8.2a). These features are due to second-order co-tunnelling, and their peak shape reflects the singularities in the quasi-particle density of states at the gap edges. In spite of the Coulomb blockade effect, we observe a finite supercurrent,  $I_{c,qd}$ , through the nanowire quantum dot. We exploit the SQUID geometry to determine the critical value and the sign of this supercurrent in a current-biased measurement [21]. When an integer number of flux quanta is applied through the SQUID area the critical current of the SQUID corresponds to the sum of the critical currents of the two junctions [2], i.e.  $I_c = I_{c,qd} + I_{c,REF}$ . We set  $I_{c,REF} = 320 \text{ pA}$ , and extract the  $V_L$ -dependence of  $I_{c,qd}$  directly from the measurement of  $I_c$  (Fig. 8.2a). We find  $I_{c,qd} < 0$  for two charge states of the quantum dot, denoted by  $\diamond$ , and  $\square$  in Fig. 8.2b. The negative supercurrent of the quantum dot junction is confirmed by the  $\Phi_0/2$ -shift between the SQUID oscillations for  $I_{c,qd} < 0$  (Fig. 8.2c, red trace) and those for  $I_{c,qd} > 0$  (blue trace). A colour plot of  $I_c(V_L, \Phi)$  in Fig. 8.2d shows the transitions between positive and negative supercurrents around the charge state denoted by  $\square$ .

Negative supercurrents have been predicted for superconductors coupled by a magnetic impurity or a single-level interacting quantum dot [3, 4, 5, 7]. In these systems resonant tunnelling of Cooper pairs is prohibited due to Coulomb blockade. Nevertheless, Cooper pairs can be transported via fourth-order co-tunnelling events. Three examples of such events are shown in Fig. 8.3. The top and bottom diagrams are the initial and final states, respectively, and the diagrams in between show one of the three intermediate virtual states. Due to Coulomb blockade, a sequence of intermediate states involves an energy cost comparable to the charging energy,  $E_c$  (for  $\Delta^* \ll E_c$ ). Nevertheless, when the tunnel rate is on the order of  $E_c/h$ , a Cooper pair can be transported by higher order co-tunnelling events [22]. In principle, there are 24 possible sequences of 4 tunnel events. However, in a single-level quantum dot only a small number of sequences are allowed. Figure 8.3a illustrates the transfer of a Cooper pair through a quantum dot with a single spin-degenerate level occupied by one electron (with spin up,  $|\uparrow\rangle$ ). The sequence of four tunnel processes, indicated by the numbers, is necessarily permuted compared to the ordinary transport of Cooper pairs. The remarkable result is that the spin-ordering of the Cooper pair is reversed, that is, the Cooper pair on the right is created in the order  $|\uparrow\rangle, |\downarrow\rangle$  while the pair on the left is annihilated in the order  $|\downarrow\rangle, |\uparrow\rangle$ . This spin-reversal results in a

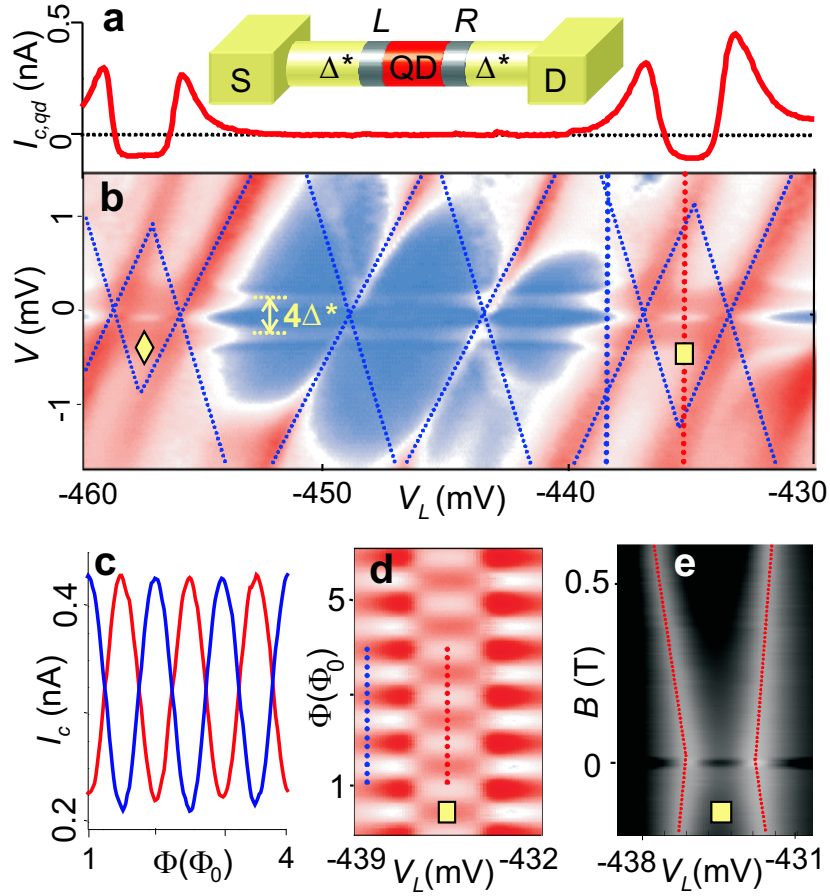


**Figure 8.2:** Supercurrent reversal in an interacting quantum dot. **a**, Plot of the critical current of the quantum dot,  $I_{c,qd}$ , as a function of gate voltage,  $V_L$ , for the same gate voltage region as in (b). A negative supercurrent is observed for two charge states. Inset: schematic of the quantum dot in the nanowire. **b**, Colour scale plot of differential conductance,  $dI/dV(V, V_L)$ , in the superconducting state ( $dI/dV$  increases from blue, white, to red).  $V_{REF} = -0.8V$ .  $\diamond$ ,  $\square$  indicate two charge states that exhibit negative supercurrent. Blue dotted lines indicate the diamond edges. **c**, Two  $I_c(\Phi)$  curves taken at gate voltages indicated by the vertical red and blue dotted lines in (b), demonstrating the shift by  $\Phi_0/2$  between the conventional (blue) and the  $\pi$ -regime (red). **d**, Critical current of the SQUID,  $I_c$ , in colour-scale as a function of magnetic flux,  $\Phi$ , and gate voltage,  $V_L$ .  $\square$ : The interference signal is shifted by half a flux quantum compared to adjacent Coulomb diamonds, indicating the  $\pi$ -shift in the Josephson relation. Red and blue dotted lines correspond to red and blue traces in (c). **e**, Gray-scale plot of linear conductance,  $G$  (increasing from black to white), as a function of magnetic field,  $B$ , and gate voltage,  $V_L$ .  $\square$ : The Coulomb peak spacing in this charge state increases with increasing field due to the Zeeman effect, indicating that the number of electrons is odd. All measurements are taken at  $T=30mK$ .

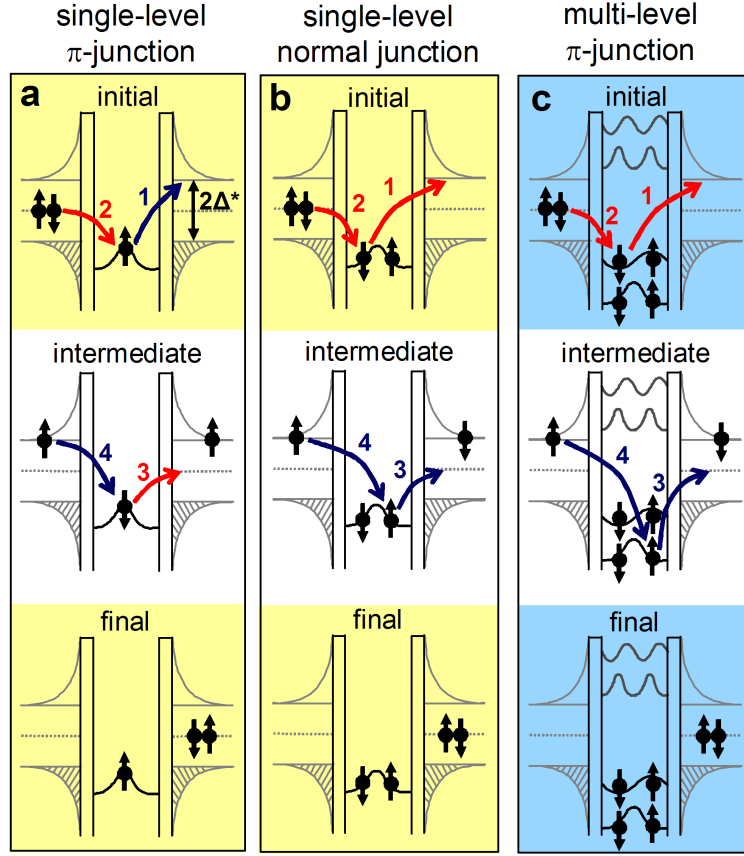


**Figure 8.3:** Energy diagrams illustrating Cooper pair transport through a quantum dot due to fourth-order co-tunnelling. Top and bottom panels represent initial and final states, respectively. The intermediate panels show one of the three virtual intermediate states. Numbers indicate the sequence of tunnel events. Red (blue) corresponds to the tunnelling of a spin-down (spin-up) electron. **a**, Transport occurs through a single spin-degenerate level filled with one electron. During this event the spin-ordering of the Cooper pair is reversed. This results in a negative contribution to the supercurrent (see also diagrams in [5]). **b**, Transport through one spin-degenerate level filled with two electrons. The spin-ordering of the Cooper pair cannot be reversed, resulting in a positive supercurrent. **c**, Co-tunnelling event involving two energy levels with wavefunctions of opposite parity. This results in a negative contribution to the supercurrent [7].

sign-change of the Cooper pair singlet state (e.g. from  $1/\sqrt{2}(|\uparrow\downarrow\rangle - |\downarrow\uparrow\rangle)$  to  $e^{i\pi}/\sqrt{2}(|\uparrow\downarrow\rangle - |\downarrow\uparrow\rangle)$ ) leading to a  $\pi$ -shift in the Josephson relation and a negative supercurrent. However, if an extra electron is added to the quantum dot the sequence of tunnel events discussed above is prohibited due to the Pauli exclusion principle. Now other sequences of tunnel events are allowed which result

in a normal, positive supercurrent [5] (see Fig. 8.3b). Therefore, in a single-level quantum dot a negative (positive) supercurrent is expected for an odd (even) number of electrons.

We can discriminate between odd and even numbers of electrons in Fig. 8.2b by measuring the linear conductance,  $G$ , as a function of gate voltage and magnetic field,  $B$  (see Fig. 8.2e). We observe that the Coulomb peak spacing for the two charge states denoted by  $\diamond$  and  $\square$  increases due to the Zeeman effect, demonstrating that for these charge states the occupation number,  $n$ , is odd [23] (only  $\square$  is shown,  $|g\text{-factor}| \sim 15$  similar to previous results for similar systems [24]). These observations are consistent with the model described above.

## 8.5 Supercurrents through multi-level quantum dots

However, for the charge state around  $V_L = -447\text{mV}$  with an odd number of electrons we observe a very small, but positive critical current ( $I_c \sim 10\text{pA}$ ). Moreover, in a different gate voltage range, shown in Fig. 8.4a, supercurrent reversal is observed also for charge states with an even number of electrons. We argue that these observations originate from co-tunnelling via multiple energy levels of the quantum dot. The multi-level nature of the quantum dot for the gate range studied in Fig. 8.4a, emerges from the measurement of differential conductance in the normal-state (Fig. 8.1e). Here several peaks parallel to the diamond edges are observed, which correspond to transport through excited states of the quantum dot. In this gate voltage range the level spacing,  $\delta$ , is of the order of  $E_c$ . Therefore, these excited states can take part in co-tunnelling events and the simple model of a single-level quantum dot is no longer appropriate. As a result, all 24 sequences of tunnel events are allowed for both odd and even numbers of electrons. Therefore, a negative supercurrent due to permutation of tunnel events is possible for both odd and even numbers of electrons [7, 25] (see Appendix). Additionally, in the multi-level regime properties of the wavefunctions of the quantum dot become important. To illustrate this we consider the co-tunnelling event in Fig. 8.3c in which two different energy levels are involved in a dot with an even number of electrons. Because the two electrons now take a different path they can acquire a different phase. The opposite parity of the wavefunctions results in a phase difference of  $\pi$  and, therefore, this event contributes to a negative supercurrent [7] (see Appendix). So, for a multi-level dot two effects can result in supercurrent reversal: permutation of tunnel events and an opposite parity of wavefunctions. When co-tunnelling events with a negative contribution dominate, the junction



will exhibit a negative supercurrent.

To further investigate the importance of multi-level effects we numerically evaluate the critical current using fourth-order perturbation theory (see Appendix for details) [6, 7]. We assume that tunnel couplings are random in amplitude and sign (reflecting the parity of wavefunctions) and set  $\Delta^*/E_c = 0.1$ , as in our experiment. The probability for a negative supercurrent in the centre of a Coulomb diamond,  $P_\pi$ , is plotted in Fig. 8.4b for odd and even numbers of electrons. A very large average level spacing ( $\delta/E_c \gg 1$ ) effectively gives a single-level quantum dot so that  $P_\pi = 1$  (0) for odd (even) numbers as explained in Figs. 3a,b. The dependence of the critical current,  $I_{c,qd}$ , on  $V_{gate}$  (Fig. 8.4c) indeed unambiguously demonstrates the correlation between the number of electrons on the dot and the supercurrent sign. This correlation is absent in the opposite limit ( $\delta/E_c \ll 1$ ), where  $P_\pi \sim 0.3$  for both odd and even numbers of electrons, in agreement with previous calculations [7]. From the experimental data in Fig. 8.1e, we estimate  $\delta/E_c \sim 0.4$  which clearly indicates an intermediate regime. Fig. 8.4d shows a typical result for  $I_{c,qd}$  versus  $V_{gate}$  for  $\delta/E_c = 0.4$ . As observed in the experiment we obtain a negative supercurrent for both even (blue dot) and odd (red dot) numbers of electrons. Also, the typical line-shapes are in close resemblance with the experimental data. Thus, in this multi-level regime co-tunnelling events occur through a single level as well as through different levels. Consequently, the sign of the supercurrent is not only determined by the number of electrons on the quantum dot but also by the orbital wavefunctions of the involved energy levels.

## 8.6 Appendix

### 8.6.1 Additional data

Here we show additional data for a different device (see Fig. 8.6c for an SEM image). The general behaviour of this sample is similar to that of the device discussed in the main text. The supercurrent reversal is demonstrated in Fig. 8.5a, which shows the critical current of the nanowire quantum dot junction,  $I_{c,qd}$ , as a function of gate voltage,  $V_L$  (the critical current of the reference junction,  $I_{c,REF}$ , is set to 280pA). The corresponding measurement of differential conductance of the quantum dot,  $dI/dV$ , as a function of  $V$  and  $V_L$  is shown in Fig. 8.5b. A negative supercurrent is observed for two adjacent diamonds. Therefore, supercurrent reversal occurs for both odd and even numbers of electrons on the quantum dot. From Fig. 8.5b we can estimate the ratio of the mean level spacing and the charging energy:  $\delta/E_c \sim 0.3$ . If we compare this value with the theoretical results in Fig. 8.4b, we indeed expect supercurrent reversal for odd and even  $n$ .

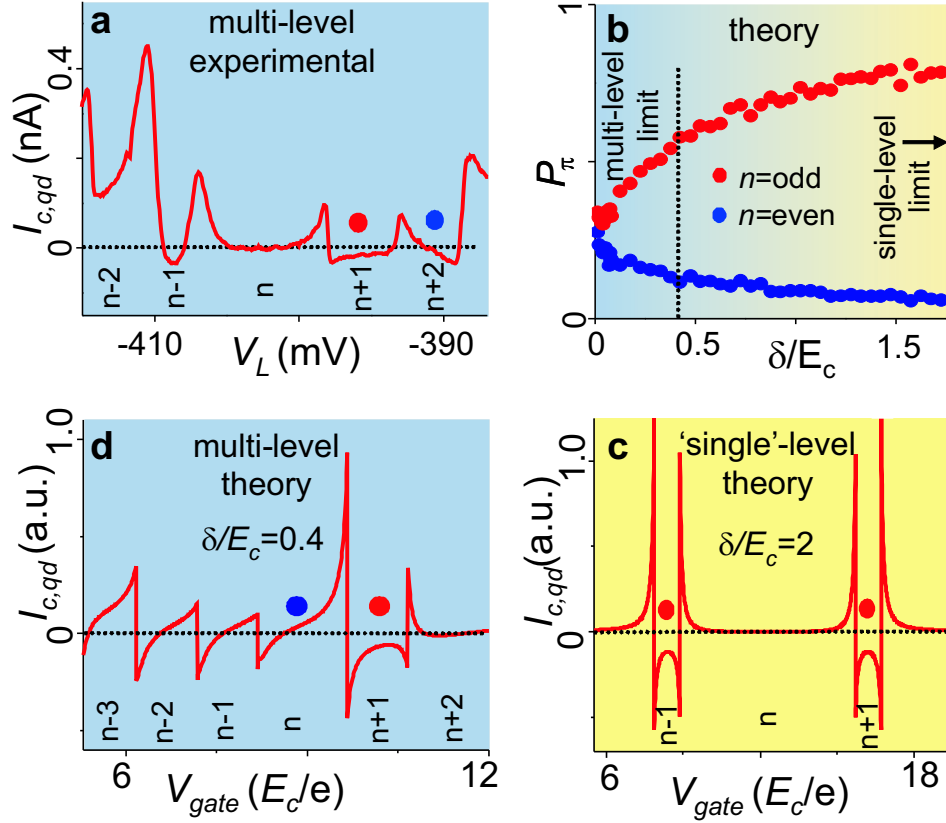


**Figure 8.4:** Experimental results and numerical simulations for a multi-level quantum dot. Panels are ordered clockwise. **a**, Measured critical current of the quantum dot,  $I_{c,qd}$ , as a function of  $V_L$  showing supercurrent reversal for even and odd numbers of electrons (indicated by a blue and red dot, respectively,  $V_R = -0.4V$ ). **b**, Calculated probability of  $\pi$ -behaviour,  $P_\pi$ , for odd (red) and even (blue) numbers of electrons as a function of  $\delta/E_c$ . Strength and sign of tunnel couplings are randomly varied. For  $\delta/E_c \gg 1$ , the limiting case of a single-level quantum dot is reached, resulting in  $\pi$ -behaviour for odd numbers and conventional behaviour for even numbers of electrons. In the multi-level limit ( $\delta/E_c \ll 1$ ) we obtain  $P_\pi \sim 0.3$  for both even and odd numbers of electrons. **c**, Calculated critical current,  $I_{c,qd}$ , as a function of gate voltage,  $V_{gate}$ , for  $\delta/E_c = 2$ . For odd numbers of electrons (red dots) the critical current is typically negative, similar to the measurement shown in Fig. 8.2a. **d**,  $I_{c,qd}(V_{gate})$  for  $\delta/E_c = 0.4$ . Negative supercurrents are found for both odd (red dot) and even numbers of electrons (blue dot) and line-shapes qualitatively reproduce the experimental data shown in (a).

### 8.6.2 Nanowire growth and device fabrication

Substrates for the wire growth were prepared by dispersing 20 nm Au colloids on an epi-ready InP(100) substrate. The nanowires were grown epitaxially in the two [111]B directions in the VLS growth mode by the use of a low-pressure

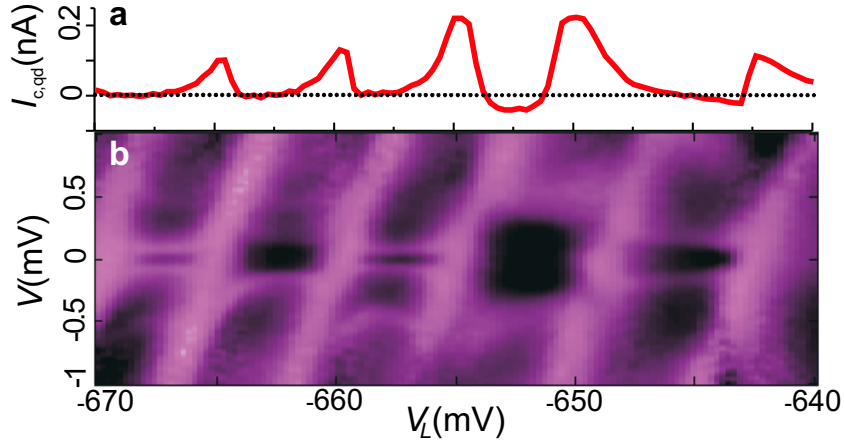


**Figure 8.5:** Supercurrent reversal in a second device. **a**, Plot of the critical current of the quantum dot,  $I_{c,qd}$ , as a function of gate voltage,  $V_L$ , for the same gate voltage region as in (b). **b**, Colour scale plot of differential conductance,  $dI/dV$ , as a function of bias voltage,  $V$ , and gate voltage,  $V_L$  ( $dI/dV$  increases from black to purple). Two adjacent charge states exhibit  $\pi$ -behaviour.

(50 mbar) Metal-Organic Vapour-Phase Epitaxy (MOVPE) system (Aixtron 200) (Fig. 8.6a). Trimethylindium (TMI), phosphine ( $\text{PH}_3$ ), and arsine ( $\text{AsH}_3$ ) were used as precursors in a total flow of 6.0 l/min where hydrogen ( $\text{H}_2$ ) was used as carrier gas. The TMI molar fraction was  $2.8 \cdot 10^{-5}$ , and the  $\text{PH}_3$  and  $\text{AsH}_3$  molar fractions were  $1.5 \cdot 10^{-2}$ . A  $\text{PH}_3$  pressure was applied during the pre-anneal (at  $550^\circ\text{C}$  for 10 min) and the heating of the substrate to the desired growth temperature ( $420^\circ\text{C}$ ), at which growth was initiated by opening the TMI source. In order to reduce the tapering of the nanowires first an InP segment was grown for 1 minute, followed by the InAs segment, grown for 10 minutes. Although this approach reduces the tapering, the tapering of the InAs nanowires (due to non-catalytic side-deposition) is still considerable as is shown in Fig. 8.6b. The diameter of the InAs nanowires ranges from  $\sim 20$  nm at the top of the nanowire to  $\sim 70$  nm at the base. After growth, the wires were randomly deposited on a degenerately doped silicon wafer covered with a 250 nm dry thermal oxide. The position of the nanowires was determined by using a set of pre-deposited markers. With conventional e-beam lithography the electrodes were defined in a double-layer of PMMA. The superconducting contacts (10nm Ti / 100nm Al) were deposited by e-beam evaporation in a UHV system with a background pressure of  $3 \cdot 10^{-8}$  mbar. Before evaporation a 5s BHF-dip was performed in order to reduce the contact resistance. The thin titanium layer ensures a high transparency of the contacts while the aluminium is used for its superconducting properties. From transport measurements we observed that the superconducting gap ( $2\Delta$ ) of the

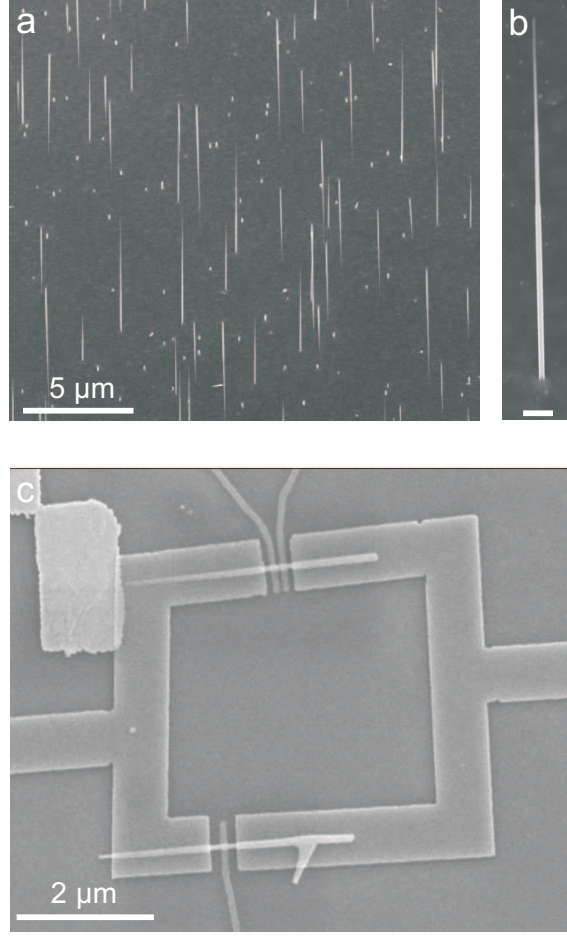


**Figure 8.6:** Scanning Electron Microscopy (SEM) images. **a**, SEM-image of InAs nanowires epitaxially grown on an InP(100) substrate. **b**, SEM-image of an InAs nanowire (scalebar is 300 nm). **c**, SEM-image of the second nanowire device. An alignment marker is visible in the upper left part of the image.

bi-layer is  $200\text{--}250\mu\text{eV}$ . In a second lithography step the local gates were defined and again e-beam deposition was used to deposit 100nm thick aluminium gates. The typical breakdown voltage of the local gates is  $-2\text{V}$ , which is well above the voltages that we need to locally deplete the InAs nanowires (up to  $-1\text{V}$ ).

### 8.6.3 Additional discussion

As explained in the main text two effects determine the sign of supercurrent: (i) permutation of tunnel events, and (ii) parity of wave functions of the levels in the dot. First we discuss both effects separately and then the combination of the two.

(i) Many co-tunnelling events contribute to the supercurrent. Each co-tunnelling event involves 4 elementary tunnel events. The sign of a contribution of a particular co-tunnelling event depends on the sequence of the elementary tunnel events. Each tunnel event is represented by electron creation/annihilation operators so the sequence of the tunnel events corresponds to a sequence of electron operators. We define operators that create electrons in the right superconducting lead,  $c_{\sigma}^{\dagger}$ , and annihilate electrons in the left superconducting lead,  $c_{\sigma}$ , with spin  $\sigma$ . In order to determine the sign of each contribution we take the sequence of operators and permute operators to achieve the conventional sequence for Cooper pair transport from the left to the right lead:  $c_{\uparrow}^{\dagger}c_{\downarrow}^{\dagger}c_{\downarrow}c_{\uparrow}$ . Owing to the anti-commutation of electron operators, odd (even) numbers of permutations result in a negative (positive) sign of the contribution. In general, there are  $4!=24$  different possible sequences of 4 operators. However, in each concrete situation the number of allowed sequences can be reduced because the levels involved in the co-tunneling event are either empty or filled. In the case of a single level filled with one electron, there are 6 sequences allowed. All 6 give a negative contribution to the supercurrent. We demonstrate this for the sequence illustrated in Fig. 8.3a. The corresponding sequence of operators is given by:  $c_{\uparrow}c_{\downarrow}^{\dagger}c_{\downarrow}c_{\uparrow}^{\dagger}$ . In order to achieve the conventional sequence for Cooper pair transport we have to perform five permutations. This gives a negative sign:  $c_{\uparrow}c_{\downarrow}^{\dagger}c_{\downarrow}c_{\uparrow}^{\dagger} = (-1) c_{\downarrow}^{\dagger}c_{\uparrow}c_{\downarrow}c_{\uparrow}^{\dagger} = (-1)^2 c_{\downarrow}^{\dagger}c_{\downarrow}c_{\uparrow}c_{\uparrow}^{\dagger} = (-1)^3 c_{\downarrow}^{\dagger}c_{\downarrow}c_{\uparrow}^{\dagger}c_{\uparrow} = (-1)^4 c_{\downarrow}^{\dagger}c_{\uparrow}^{\dagger}c_{\downarrow}c_{\uparrow} = (-1)^5 c_{\uparrow}^{\dagger}c_{\downarrow}^{\dagger}c_{\downarrow}c_{\uparrow}$ .

If the single level is filled with two electrons, the six sequences mentioned before are forbidden by Pauli exclusion principle. In this situation other sequences are allowed that give a positive contribution. For example, the sequence of operators corresponding to the co-tunnelling event illustrated in Fig. 8.3b is given by:  $c_{\uparrow}c_{\uparrow}^{\dagger}c_{\downarrow}c_{\downarrow}^{\dagger}$ . The occurrence of four permutations compared to the conventional sequence of operators for Cooper pair transport results in a positive sign. Therefore the sign of the supercurrent for a single-level dot is determined by the number of electrons on the quantum dot.

In the case of a multi-level quantum dot the above mentioned restrictions on the sequences of operators are relaxed and, in principle, all 24 sequences are possible. As a result, also events can occur that give a negative (positive) contribution to the supercurrent for even (odd) numbers of electrons. To illustrate this we consider the situation when two electrons are transported through different levels for an even number of electrons on the quantum dot (Fig. 8.7a). In this case the sequence of operators is given by:  $c_{\uparrow}c_{\downarrow}^{\dagger}c_{\downarrow}c_{\uparrow}^{\dagger}$ . This sequence is identical to the sequence for Fig. 8.3a, thus resulting in a negative contribution to the supercurrent. By investigating all 24 possible sequences the following general conclusion can be obtained [7]: The contribution to the supercurrent for a co-tunnelling

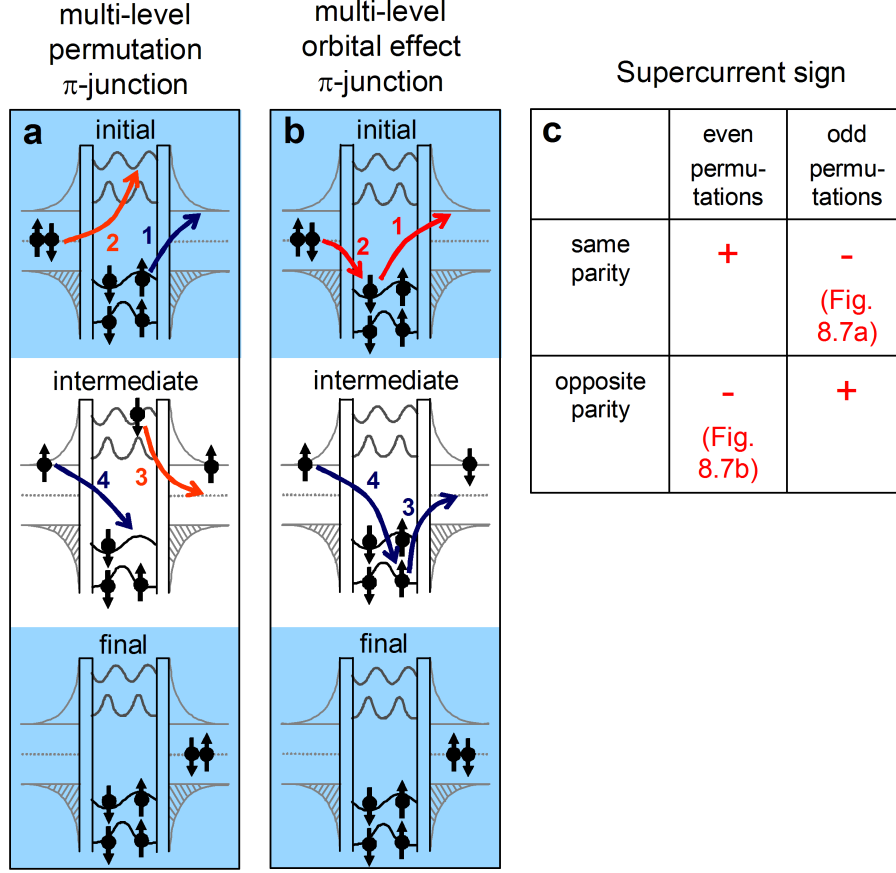


**Figure 8.7:** Energy diagrams illustrating transport through a multi-level quantum dot. **a**, Transport occurs through a filled and an empty energy level. The corresponding sequence of operators involves five permutations resulting in a negative supercurrent. **b**, Transport occurs through two filled energy levels with opposite parity of the corresponding wavefunctions. This results in a negative contribution to the supercurrent. **c**, Sign of supercurrent contribution for the four different types of co-tunnelling events. Only if one of the above effects occurs, the contribution to the supercurrent is negative.

event is negative when one electron is transported through a filled level and the other electron through an empty level. The contribution is positive when both electrons are transported through filled or through empty levels. Note that it is necessary to include dot-operators in order to determine the correct supercurrent sign for all sequences.

(ii) Orbital effects can result in negative supercurrents when two electrons are transported through different levels (or orbitals) of the quantum dot [7]. We illustrate this using equation 8.1 from the next subsection. In this equation, the contribution to the supercurrent of a co-tunnelling event is proportional to the

product of the four tunnel amplitudes. The tunnel amplitudes can be positive or negative, depending on the overlap integral with the corresponding wavefunction. In the case of a quantum dot with a single spin-degenerate level, this always yields a positive result because the tunnel amplitudes are squared. However, when two electrons are transported through different energy levels, an odd number of negative tunnel amplitudes results in a negative supercurrent. This situation corresponds to Cooper pair transport through two levels with wavefunctions of opposite parity. An example of such a co-tunnelling event is illustrated in Fig. 8.7b.

The combined result of effects (i) and (ii) are summarized in Fig. 8.7c, showing the sign of the supercurrent for the four possible situations. Note that when both effects are present in a co-tunnelling effect, the supercurrent sign will be positive.

The sign of the supercurrent of the quantum dot is determined by the dominating type of co-tunnelling events (i.e. + or -). As mentioned before, for a single-level quantum dot the supercurrent sign is negative (positive) for odd (even) numbers of electrons on the dot. In the case of a multi-level quantum dot the supercurrent sign is determined by the dominant co-tunnelling events. Co-tunnelling events will have a large contribution to the supercurrent when: 1. the amplitude of the four tunnel couplings is large, and 2. the energy of the intermediate virtual states is small. By numerical evaluation (discussed below) the sign and magnitude of the critical current for a quantum dot with a specific energy spectrum can be calculated.

#### 8.6.4 Numerical evaluation

To model the quantum dot, we proceed in a conventional way: We introduce a system of discrete spin-degenerate levels with energies  $E_i$ . In a given charge configuration, these energies are counted from the last level filled. Coulomb interaction is taken into account in addition/extraction energies of the dot. For instance, the energy cost to put an extra electron to the level  $i$  reads  $E_i + E^+$ , to put two electrons to the levels  $i$  and  $j$  reads  $E_j + E_i + E^{++}$ ,  $E^+$ ,  $E^{++}$  being the charging energy differences. The charging energy of the state with  $N$  electrons reads as usual:  $E_{ch} = E_c(N - C_g V_g)^2$ .

In a common quantum dot, the actual value of  $N$  is determined from the minimum of the charging energy and changes in step-like fashion with increasing gate voltage. The tunnelling between a discrete level  $i$  of the dot and a continuous-spectrum state  $\mathbf{k}$  in a lead is generally described by an amplitude  $t_{i,k}$ . Due to time-reversibility, all amplitudes can be chosen real.

As mentioned, the amplitude of the Cooper pair transfer is contributed by

co-tunneling ‘events’, each involving up to two levels  $(i, j)$  and four elementary tunneling ‘events’. Each co-tunneling event comes with a certain combination of amplitudes:  $t_i^L t_i^R t_j^L t_j^R$ . It is convenient to introduce products of amplitudes that characterize tunnelling via a certain level:  $T_i = t_i^L t_i^R \sqrt{\nu_L \nu_R}$ ;  $\nu_L, \nu_R$  being the densities of states on both sides of the contact. We note that  $T_i$  can be both positive and negative. Its sign is determined by the *parity* of the corresponding wave-function: positive if the wave-function is of the same sign at both tunnel point contacts and negative otherwise. A compact expression for the Josephson amplitude reads:

$$-E_J = \sum_{i,j,\alpha} T_i T_j (A_{ee} \tilde{f}_{i,\alpha} \tilde{f}_{j,-\alpha} + A_{hh} f_{i,\alpha} f_{j,-\alpha} - A_{he} f_{i,\alpha} \tilde{f}_{j,-\alpha}); \quad (8.1)$$

Here,  $\alpha$  denotes the spin index and  $f_{i,\alpha}$  represents the electron filling factor of a given level ( $\tilde{f}_{i,\alpha} \equiv 1 - f_{i,\alpha}$  is the hole filling factor). Since we disregard temperature  $f_{i,\alpha}$  can only take two values: 0 and 1. We keep the spin index to treat completely filled and half-filled levels on equal footing: For filled levels  $f_{i,\alpha} = f_{i,-\alpha}$ , while for half-filled ones  $f_{i,\alpha} + f_{i,-\alpha} = 1$ .  $A_{ee}$ ,  $A_{hh}$ ,  $A_{he}$  are positive functions of the two level energies,  $\Delta$ , and the charging energy. From this expression one can inherit all sign rules previously discussed. For a single half-filled level,  $i = j$  and only the third term survives resulting in a negative sign. Terms with  $i = j$  that correspond to either filled or empty levels always provide a positive contribution. For a contribution of a pair of different levels,  $i \neq j$ , and the sign depends on the sign of  $T_i T_j$ , that is, on relative parity of the corresponding wave-functions. If both wave-functions are odd or even, the contribution is positive if both levels are filled or empty, and negative otherwise. If one wave-function is odd and another one is even, the situation is opposite: the sign is negative if both levels are filled or empty, and positive otherwise. The concrete expression for  $A_{ee}$  reads:

$$A_{ee}(E_i, E_j) = \int d\varepsilon_1 d\varepsilon_2 \nu(\varepsilon_1) \nu(\varepsilon_2) \left( \frac{\frac{1}{(\varepsilon_1 + E_i + E^+)(E_i + E_j + E^{++})(\varepsilon_2 + E_j + E^+)} + \frac{1}{(\varepsilon_1 + E_i + E^+)(E_i + E_j + E^{++})(\varepsilon_2 + E_i + E^+)} + \frac{1}{(\varepsilon_1 + E_i + E^+)(\varepsilon_1 + \varepsilon_2)(\varepsilon_2 + E_j + E^+)}}{(\varepsilon_1 + E_i + E^+)(\varepsilon_1 + \varepsilon_2)(\varepsilon_2 + E_j + E^+)} \right). \quad (8.2)$$

Similar expressions can be obtained for  $A_{hh}$  and  $A_{he}$ . In all cases, they are obtained by integration of three energy denominators corresponding to the possible virtual states over energies of virtual quasiparticles.  $\nu(\varepsilon_1)$  in the above expressions presents the BCS factor of superconducting density of states,  $\nu(\varepsilon) \equiv$



$\Theta(\Delta^2 - \varepsilon^2)|\varepsilon|/\sqrt{\varepsilon^2 - \Delta^2}$ . Two-dimensional integration required for the numerical evaluation of  $A$  slowed down the simulations considerably.

The concrete numerical calculations have been performed in two ways. Firstly, we take a randomly chosen realisation of  $T_i$ ,  $E_i$  and calculate the current as function of gate voltage in a wide interval of gate voltage. Typically, we took about a hundred levels and the interval of gate voltages where the number of electrons varied from 50 to 70. The ratio of charging energy and  $\Delta$  was fixed to the experimental value while the ratio of level spacing and charging energy has been varied in a wide range. The goal of this simulation was to compare typical patterns in current-gate voltage dependence with those observed experimentally. The current typically showed pronounced peaks at the gate voltages where the number of particles changes (edges of diamonds). Peaks of either sign have been obtained. Randomly distributed  $T_i$  result in strong (by order of magnitude) variations of the current from diamond to diamond. The supercurrent changes sign within a diamond as well as at the edges. If the average spacing is smaller than the charging energy, the patterns and the magnitudes of the current exhibit relatively strong correlation in neighbouring diamonds. This indicates that the current in this case is contributed by many levels, those are essentially the same in neighbouring diamonds. The situation is opposite for large level spacing where the level closest to the Fermi energy clearly dominates the supercurrent. This, as discussed, gives positive (negative) supercurrent for even (odd) numbers of electrons.

Secondly, we use the same simulation scheme to quantify the probability of a negative/positive sign of the supercurrent. In this case, we fix the gate voltage to the middle of an even (odd) diamond and evaluate the current for a big set of random realizations of  $T_i$  (typically, 10.000 realizations). So we can get the probability with 1% accuracy.

*Note 1:* It is important to recognize an important detail specific for a dot connected to superconducting leads: its charging state is bistable at zero temperature near the values of gate voltage corresponding to the charge of  $N$ . This is a consequence of the fact that one has to create a quasiparticle in order to put a charge into a superconductor, this costs extra energy  $\Delta$ . In our simulations, we disregarded the bistability assuming that the dot is always in the ground state. This should correspond to the experimental situation where the supercurrent has been measured at small but finite voltage. This voltage, although small, may generate the quasiparticles required for a fast relaxation to the ground state.

*Note 2:* We disregard the dependence of the amplitude on  $\mathbf{k}$ . This corresponds to the important physical assumption of a point-like tunnelling contact where most tunnelling processes take place within the same transport channel

that has the highest transparency. While this assumption frequently fails for natural oxide tunnel barriers in metallic systems, it is well-justified and proven for electrostatically formed tunnel barriers in semiconductor quantum dots where the potential profile is smooth at the scale of the electron wave-length. Since the junctions in our experiment are formed electrostatically, we assume that the tunnel contacts are point-like.

We thank Y-J. Doh and L. Glazman for discussions, G. Immink for nanowire growth and A. van der Enden and R. Schouten for technical support.

## References

- [1] Josephson, B. D. Possible New Effects in Superconductive Tunnelling. *Phys. Lett.* **1**, 251-253 (1962).
- [2] Tinkham, M., Introduction to Superconductivity (McGraw-Hill, Singapore, ed. 2, 1996).
- [3] Bulaevskii, L. N., Kuzii, V. V., & Sobyenin, A. A. Superconducting system with weak coupling to the current in the ground state. *JETP Lett.* **25**, 290 (1977).
- [4] Glazman, L. I., & Matveev, K. A. Resonant Josephson current through Kondo impurities in a tunnel barrier. *JETP Lett.* **49**, 659 (1989).
- [5] Spivak, B. I., & Kivelson, S. A. Negative local superfluid densities: The difference between dirty superconductors and dirty bose liquids. *Phys. Rev. B* **43**, 3740 (1991).
- [6] Bauernschmitt, R., Siewert, J., Nazarov, Yu. V., & Odintsov, A. A. Josephson effect in low-capacitance superconductor-normal-metal-superconductor systems. *Phys. Rev. B* **49**, 4076 (1994).
- [7] Rozhkov, A. V., Arovas, D. P., & Guinea, F. Josephson coupling through a quantum dot. *Phys. Rev. B* **64**, 233301 (2001).
- [8] van Harlingen, D. J. Phase-sensitive tests of the symmetry of the pairing state in the high-temperature superconductors - Evidence for dx<sup>2</sup>-y<sup>2</sup> symmetry. *Rev. Mod. Phys.* **67**, 515 (1995).
- [9] Ryazanov, V. V. et al. Coupling of two superconductors through a ferromagnet: Evidence for a p-Junction. *Phys. Rev. Lett.* **86**, 2427 (2001).
- [10] Baselmans, J. J. A., Morpurgo, A. F., van Wees, B. J., & Klapwijk, T. M. Reversing the direction of the supercurrent in a controllable Josephson junction. *Nature* **397**, 43 (1999).

- [11] Ralph, D. C., Black, C. T., & Tinkham, M. Spectroscopic measurements of discrete electronic states in single metal particles. *Phys. Rev. Lett.* **74**, 3241 (1995).
- [12] Black, C. T., Ralph, D. C., & Tinkham, M. Spectroscopy of the superconducting gap in individual nanometer-scale aluminum particles. *Phys. Rev. Lett.* **76**, 688 (1996).
- [13] Buitelaar, M. R., Nussbaumer, T., & Schönenberger, C. Quantum dot in the Kondo regime coupled to superconductors. *Phys. Rev. Lett.* **89**, 256801 (2002).
- [14] Buitelaar, M. R. et al. Multiple Andreev reflections in a carbon nanotube quantum dot. *Phys. Rev. Lett.* **91**, 057005 (2003).
- [15] Jarillo-Herrero, P., van Dam, J. A., & Kouwenhoven, L.P. Quantum supercurrent transistors in carbon nanotubes. *Nature* **439**, 953 (2006).
- [16] Doh, Y. J. et al. Tunable Supercurrent through Semiconductor Nanowires. *Science* **309**, 272-275 (2005).
- [17] Wagner, R. S., & Ellis, W. C. Vapor-Liquid-Solid mechanism of single crystal growth. *Appl. Phys. Lett.* **4**, 89 (1964).
- [18] Morales, A. M., & Lieber, C. M. A laser ablation method for the synthesis of crystalline semiconductor nanowires. *Science* **279**, 208 (1998).
- [19] Björk M. T. et al. One-dimensional heterostructures in semiconductor nanowhiskers. *Appl. Phys. Lett.* **80**, 1058 (2002).
- [20] Verheijen, M. A., Immink, G., de Smet, T., Borgström, M. T., & Bakkers, E. P. A. M. Growth kinetics of heterostructured GaP-GaAs nanowires. *J. Am. Chem. Soc.* **128**, 1353 (2006).
- [21] Baselmans, J. J. A., Heikkilä, T. T., van Wees, B. J., & Klapwijk, T. M. Direct Observation of the transition from the conventional superconducting state to the p state in a controllable Josephson junction. *Phys. Rev. Lett.* **89**, 207002 (2002).
- [22] Averin, D. V., & Nazarov, Y. V. in Single Charge Tunneling (eds Grabert, H., Devoret, M. H.) 217-247 (Proc. NATO ASI Ser. B 294, Plenum, New York, 1991).
- [23] Sohn, L. L., Kouwenhoven, L. P., & Schön, G. (eds). Mesoscopic Electron Transport (Kluwer, Dordrecht, 1997).
- [24] Björk, M. T. et al. Tunable effective g factor in InAs nanowire quantum dots. *Phys. Rev. B* **72**, 201307 (2005).

- [25] Shimizu, Y., Horii, H., Takane, Y., & Isawa, Y. Multilevel effect on the Josephson current through a quantum dot. *J. Phys. Soc. Jap.* **67**, 1525 (1998).

# Summary

## Quantum transport in semiconductor nanowires

This thesis describes a series of experiments aimed at understanding the low-temperature electrical transport properties of semiconductor nanowires. The semiconductor nanowires (1-100 nm in diameter) are grown from nanoscale gold particles via a chemical process called vapor-liquid-solid (VLS) growth. The huge versatility of this material system (e.g. in size and materials) results in a wide range of potential applications in (opto-)electronics. During the last few years many important proofs of concept have already been provided like lasers, field-effect transistors, light emitting diodes, and biochemical sensors. Simultaneously, the versatility of semiconductor nanowires creates new opportunities for the study of quantum transport phenomena.

In chapter 4 of this thesis the principle of epitaxial growth of III-V nanowires on a group IV substrate is demonstrated. This is an important step towards the integration of the superior (opto-)electronic properties of III-V semiconductors with silicon technology. Up till now the epitaxial integration between III-V and type IV semiconductors has been prevented due to issues such as lattice and thermal expansion mismatch. The epitaxial growth is demonstrated by X-ray diffraction and transmission electron microscopy. Conductive atomic force microscopy is used in order to show that a low-resistance electrical contact can be obtained between the nanowires and the substrate.

The measurements described in the other chapters of this thesis are motivated by the new opportunities that arise for the field of quantum transport. The quantum mechanical properties of semiconductor nanowires become visible at low temperatures (below a few Kelvin) and can be very different from room-temperature transport properties. For instance, the confinement of electrons in a small nanowire segment results in a discrete electronic energy spectrum forming a quantum dot, or artificial atom.

The electrical properties of quantum dots can be studied by attaching a source and drain electrode via tunnel barriers. In order to be able to adjust the number

of electrons on the quantum dot, it is capacitively coupled to a gate electrode. By measuring the current through the quantum dot as a function of the applied bias voltage and gate voltage, the discrete energy spectrum can be investigated. This technique is used in chapter 5 in order to study quantum dots in indium phosphide nanowires. Here, the quantum dots are defined by unintentional barriers formed inside the nanowires. Transport spectroscopy measurements demonstrate the discreteness of the energy spectrum. This is confirmed by the shape of current peaks as a function of gate voltage. At low temperatures, the width of these Coulomb peaks follows the theoretical prediction for a quantum dot with a discrete energy spectrum. When the temperature is raised and the thermal energy exceeds the level spacing, the width of the resonances follows the model for a dot with a continuous energy spectrum.

In chapter 6 it is shown that superconductivity can be induced over small length scales ( $\sim 1 \mu\text{m}$ ) in indium arsenide (InAs) nanowires by aluminum electrodes. This effect is known as the proximity effect and relies on a very transparent electrical contact between the superconducting electrode and the nanowire. Typical contact resistances are below  $1\text{k}\Omega$ . When two superconducting electrodes are closely spaced, a supercurrent can flow through an InAs nanowire due to the Josephson effect. Because of the semiconductor nature of the nanowires, the supercurrent can be switched on/off by a voltage applied to a nearby gate electrode.

The combination of quantum dots and superconductivity is studied in chapters 7 and 8. In chapter 7 the properties of carbon nanotubes are exploited to obtain a quantum dot between two superconducting electrodes. When a discrete energy level is in resonance with the Fermi energy in the leads, a supercurrent can flow through the carbon nanotube quantum dot. By changing the voltage applied to a gate electrode, successive energy levels can be tuned on/off resonance resulting in an oscillating supercurrent. Existing theoretical predictions are confirmed about the magnitude of the supercurrent flowing through a system with a discrete density of states. In this experiment the effect of charging is negligible which allows the simultaneous transport of two correlated electrons of a Cooper pair through the carbon nanotube.

The supercurrent through a quantum dot is drastically affected when charging effects in the quantum dot dominate. Due to Coulomb blockade electrons prefer to tunnel one-by-one through the quantum dot. When subsequent tunnel events are coherent the sequential transport of correlated electrons through the quantum dot can yield a supercurrent. In chapter 8 it is shown that by using semiconductor nanowires it is now possible to reach the regime where charging effects dominate but, at the same time, the supercurrent is large enough to be measurable. InAs nanowires and local gating are used in order to obtain a quantum dot with tunable

coupling to superconducting leads. A negative supercurrent is observed for several charge states of the quantum dot. Numerical simulations of the supercurrent through a multi-level quantum dot confirm the experimental results. It is shown that the supercurrent sign depends on the number of electrons on the dot and the parity of the orbital wavefunctions.

Jorden van Dam  
June 2006





# Samenvatting

## Quantum transport in halfgeleider nanodraden

Dit proefschrift beschrijft experimenten gericht op het begrijpen van de elektrische transporteigenschappen van halfgeleider nanodraden bij lage temperaturen. De halfgeleider nanodraden (met een diameter van 1-100 nm) worden gegroeid uit nanodeeltjes van goud via een chemisch proces genaamd gas-vloeistof-vast (VLS) groei. De enorme veelzijdigheid van dit materiaalsysteem (bijv. in afmetingen en materialen) resulteert in een breed scala aan mogelijke toepassingen in de (opto-)elektronica. In de afgelopen jaren zijn al veel toepassingen aangetoond, zoals lasers, transistoren, LEDs en biochemische sensoren. Tegelijkertijd biedt de veelzijdigheid van halfgeleider nanodraden nieuwe mogelijkheden voor het fundamenteel onderzoek naar quantummechanische transportverschijnselen.

In hoofdstuk 4 van dit proefschrift wordt het principe aangetoond van epitaxiale groei van III-V halfgeleiders op een type IV substraat. Dit is een belangrijke stap naar de integratie van de superieure (opto-)elektronische eigenschappen van III-V halfgeleiders met silicium technologie. Tot nu toe is deze integratie niet gelukt vanwege problemen zoals afwijkende roosterconstanten en uitzettingscoëfficiënten. De epitaxiale groei wordt aangetoond door middel van röntgendiffractie en elektronen microscopie. Met een ‘atomic force microscope’ is aangetoond dat een kleine contactweerstand kan worden verkregen tussen de nanodraden en het substraat.

De metingen die worden beschreven in de overige hoofdstukken van dit proefschrift komen voort uit de nieuwe mogelijkheden voor de studie naar quantum transporteigenschappen. De quantummechanische eigenschappen van halfgeleider nanodraden worden zichtbaar bij lage temperaturen (beneden een paar Kelvin) en kunnen enorm verschillen van de transporteigenschappen bij kamertemperatuur. Bijvoorbeeld, de opsluiting van elektronen in een klein stukje nanodraad resulteert in een discreet energiespektrum en zo kan een ‘quantum dot’, of artificieel atoom, worden gevormd.

De elektrische eigenschappen van quantum dots kunnen worden bestudeerd

door er twee elektroden via tunnelbarrières aan te koppelen. Om het aantal elektronen in de quantum dot te kunnen variëren, is deze capacitief gekoppeld aan een ‘gate’ elektrode. Het discrete energiespektrum kan worden onderzocht door de stroom door de quantum dot te meten als functie van de aangelegde bias-spanning en gate-spanning. Deze techniek is gebruikt in hoofdstuk 5 om quantum dots in indiumfosfide nanodraden te bestuderen. In dit geval zijn de quantum dots gedefinieerd door barrières die niet opzettelijk zijn gemaakt. Spectroscopiemetingen laten zien dat er sprake is van een discreet energiespektrum. Dit wordt bevestigd door de vorm van de stroompieken als functie van de gate spanning. Bij lage temperaturen volgt de breedte van deze Coulomb pieken de theoretische voorspelling voor een quantum dot met een discreet spektrum. Als de temperatuur wordt verhoogd zodat de thermische energie groter is dan de typische afstand tussen energieniveaus, is de piekbreedte gegeven door een model voor een dot met een continu spektrum.

In hoofdstuk 6 wordt aangetoond dat over korte afstanden ( $\sim 1\mu\text{m}$ ) supergeleiding kan worden geïnduceerd in indiumarsenide (InAs) nanodraden door middel van aluminium elektroden. Dit effect staat bekend als het ‘proximity’ effect en is het gevolg van een zeer transparant contact tussen de nanodraad en de supergeleidende elektrode. De typische contactweerstand is minder dan  $1\text{ k}\Omega$ . Wanneer twee supergeleidende elektroden dicht bij elkaar liggen kan een superstroom door de draad stromen door het Josephson effect. Vanwege de halfgeleider eigenschappen van de nanodraden kan de superstroom aan / uit worden geschakeld door middel van een spanning op een nabijgelegen gate elektrode.

De combinatie van quantum dots en supergeleiding wordt bestudeerd in de hoofdstukken 7 en 8. In hoofdstuk 7 worden de eigenschappen van koolstof nanobuisjes benut om een quantum dot te verkrijgen tussen twee supergeleidende elektroden. Wanneer een discreet energieniveau resonant is met de Fermi energie in de elektroden kan een superstroom door de quantum dot stromen. Door de gate spanning te veranderen kunnen opeenvolgende energieniveaus in / uit resonantie worden gebracht resulterend in een oscillerende superstroom. Bestaande theorieën worden bevestigd over de grootte van de superstroom die door een object stroomt met een discreet spektrum. In dit experiment zijn ladingseffecten verwaarloosbaar zodat twee gecorreleerde elektronen van een Cooper paar gelijktijdig kunnen worden getransporteerd door het koolstof nanobuisje.

De superstroom door een quantum dot verandert drastisch wanneer ladingseffecten in de quantum dot domineren. Vanwege Coulomb blokkade tunnelen elektronen één voor één door de quantum dot. Wanneer opeenvolgende ‘tunnel events’ coherent zijn kan opeenvolgend transport van gecorreleerde elektronen door de quantum dot resulteren in een superstroom. In hoofdstuk 8 wordt laten zien

dat het met halfgeleider nanodraden nu mogelijk is om de situatie te bereiken waar ladingseffecten overheersen maar waar tegelijkertijd de superstroom groot genoeg is om te kunnen meten. InAs nanodraden en lokale gating worden gebruikt om een quantum dot te verkrijgen met een controleerbare koppeling naar de supergeleidende elektroden. Een negative superstroom is waargenomen voor verschillende ladingstoestanden van de quantum dot. Numerieke simulaties van de superstroom door een quantum dot met meerdere energie niveaus bevestigt de experimentele resultaten. Als laatste is aangetoond dat de richting van de superstroom zowel wordt bepaald door het aantal elektronen in de quantum dot als door de pariteit van de golffuncties.

Jorden van Dam  
Juni 2006



# Curriculum Vitae

Jorden van Dam

- 13-03-1978    Born in Emmen, The Netherlands.
- 1990-1996    Grammar school, Almere College, Kampen.
- 1996-2002    M.Sc. Applied Physics, University of Groningen.  
Graduate research in the group of prof. dr. ir. B. J. van Wees.
- 2001            Internship at IBM Research Laboratories, Zurich.
- 2002-2006    Ph.D. research at Delft University of Technology  
under supervision of prof. dr. ir. L. P. Kouwenhoven.  
Subject: Quantum transport in semiconductor nanowires.



# List of publications

1. *Supercurrent reversal in quantum dots*  
Jorden A. van Dam, Yuli V. Nazarov, Erik P. A. M. Bakkers, Silvano De Franceschi,  
& Leo P. Kouwenhoven.  
Submitted to Nature.
2. *Quantum supercurrent transistors in carbon nanotubes*  
Pablo Jarillo-Herrero, Jorden A. van Dam, & Leo P. Kouwenhoven.  
Nature **439**, 953 (2006).
3. *Tunable supercurrent through semiconductor nanowires*  
Yong-Joo Doh, Jorden A. van Dam, Aarnoud L. Roest, Erik P. A. M. Bakkers,  
Leo P. Kouwenhoven, & Silvano De Franceschi.  
Science **309**, 272 (2005).
4. *Epitaxial growth of InP nanowires on germanium*  
Erik P. A. M. Bakkers, Jorden A. van Dam, Silvano De Franceschi, Leo P.  
Kouwenhoven, Monja Kaiser, Marcel Verheijen, Harry Wondergem, & Paul van  
der Sluis.  
Nature Materials **3**, 769 (2004).
5. *Electronica met nanodraden*  
Jorden van Dam, Silvano De Franceschi, Erik Bakkers, & Leo Kouwenhoven.  
Nederlands Tijdschrift voor Natuurkunde **69**, 240 (2003).
6. *Single-electron tunneling in InP nanowires*  
S. De Franceschi, J. A. van Dam, E. P. A. M. Bakkers, L. F. Feiner, L. Gurevich,  
& L. P. Kouwenhoven.  
Appl. Phys. Lett. **83**, 344 (2003).

